UTS UNIVERSITY OF TECHNOLOGY SYDNEY

# Advanced Transmitarrays and Their Beam Scanning For Future Wireless Communications

**by Xuan Wang**

Thesis submitted in fulfilment of the requirements for the degree of

**Doctor of Philosophy**

under the supervision of
Dr Pei-Yuan Qin and Prof. Y. Jay Guo

University of Technology Sydney
Faculty of Engineering and Information Technology

December 2021

# CERTIFICATION OF ORIGINAL AUTHORSHIP

I, Xuan Wang declare that this thesis, is submitted in fulfilment of the requirements for the award of the degree of DOCTOR OF PHILOSOPHY, in the Faculty of Engineering and Information Technology at the University of Technology Sydney.

This thesis is wholly my own work unless otherwise reference or acknowledged. In addition, I certify that all information sources and literature used are indicated in the thesis.

This document has not been submitted for qualifications at any other academic institution.

This research is supported by the Australian Government Research Training Program.

This thesis is the result of a research candidature conducted with Shanghai Jiao Tong University as part of a collaborative Doctoral degree.

Signed: Production Note:
Signature removed prior to publication.

15/12/2021

# ABSTRACT

In recent years, transmitarrays have attracted growing attention for many wireless communication systems. Transmitarrays combine both optical and antenna array theories, leading to high gain, high efficiency, low cost and flexible radiation performance. In this thesis, on the basis of the state-of-the-art of transmitarrays, three main contributions are made to meet the challenges that arise from future wireless communications.

The first contribution is the new approach to reduce radar cross section (RCS) of transmitarrays without sacrificing their radiation performance. Phase controllable absorptive frequency-selective transmission (AFST) elements are developed for low RCS transmitarrays, providing absorption-transmission-absorption responses. Moreover, the transmission phase within the transmission band can be controlled by rotating the AFST element. Based on these elements, a low RCS transmitarray has been designed. Compared with a reference transmitarray, the radiation performance of the low-RCS one is almost unchanged. Furthermore, significant RCS reductions have been realized in two absorption bands for wide-angle impinging electromagnetic (EM) waves.

The second contribution is the development of a dual-layer wideband conformal transmitarray at E-band. The dual-layer transmitarray element is designed based on multiple Huygens resonances at different frequencies to achieve both wideband and high efficiency properties. Continuous phase compensation of 360° is achieved, reducing phase errors of the array architecture. Employing the dual-layer Huygens elements, a cylindrically conformal transmitarray at 78 GHz has been designed. The measured results show a peak

realized gain of 26.6 dBi with an aperture efficiency of 35.9 % and 3-dB bandwidth of 20.4 % from 71 to 87 GHz, which can fully cover the E-band spectrum from 71 to 86 GHz.

The third contribution is the development of reconfigurable transmitarrays to achieve 2-dimensional (2-D) beam scanning. A new reconfigurable dual-layer Huygens element is developed. A 1-bit phase compensation with low transmission loss is achieved by controlling two PIN diodes integrated on the element. Compared with many other reconfigurable transmitarray elements using multi-layer structures with metallic vias, the developed reconfigurable Huygens element has a simpler configuration and a simpler biasing network, leading to a very robust design. This particularly facilitates large aperture array at higher frequencies. To validate the design concept, a transmitarray prototype at 13 GHz has been designed. 2-D scanning beams within $\pm 50^{\circ}$ in E-plane and $\pm 40^{\circ}$ in H-plane are achieved.

All in all, the developed advanced transmitarrays and their beam scanning represent significant knowledge advance on antenna technologies. They can find wide applications in current and future wireless communication systems.

# ACKNOWLEDGEMENTS

First of all, I would like to express my deepest gratitude to my supervisor Dr. Peiyuan Qin for his continuous guidance and support for my PhD study. He has helped me applied for the doctoral candidature at University of Technology Sydney (UTS), which really helped me have the precious opportunity to study at UTS. For my research, Dr. Peiyuan Qin has given me innovative ideas and helpful suggestions. Moreover, his insight into academic frontiers and rigorous academic attitude have deeply inspired and motivated me.

I would like to express my profound gratitude to my co-supervisor Prof. Y. Jay Guo. He has provided me the precious opportunity and invaluable guidance in pursuing my doctoral degree at UTS. Without his support, I would not have the chance to study at UTS. Prof. Guo is always resourceful in providing me insightful and profound suggestions for my research. I am also greatly inspired by Prof. Guo's rigorous academic attitude and his friendly, considerate, and generous nature.

I am deeply grateful to my supervisor Prof. Ronghong Jin at Shanghai Jiao Tong University (SJTU) for providing me the opportunity to study as a joint PhD student at UTS and SJTU. He has given me continuous and solid support throughout my whole PhD study.

I would like to thank my collaborator Dr. Anh Tuyen Le and Dr. Hao Zhang for their valuable help on my work, support with experiments, and advice on papers.

I would like to thank Prof. Trevor Bird and Prof. Richard W. Ziolkowski for their

guidance and encouragement during my PhD study. I would like to thank Prof. Yanhui Liu and Prof. Zheng Li for their valuable suggestions on my work and advice on papers. My sincere thanks also go to other members at Global Big Data Technologies Centre (GBDTC), especially, Dr. Stanley Chen, Dr. Ting Zhang, Dr. He Zhu, Dr. Wei Lin, Dr. Can Ding, Miss Lizhao Song, Miss Maral Ansari, Mr Yubo Wen, Mr Ming Li, and Mr Yuenian Chen for their kind help and support.

I am also thankful to the University of Technology Sydney for giving me the opportunity to pursue my PhD studies by granting me scholarships to cover my tuition fee and living expenses. I also acknowledge the handwork put in by the School of Electrical and Data Engineering staff to provide efficient admin and academic support to the research students.

In the end, I would like to express my forever thanks to my parents for their unconditional love, unreserved support and encouragement throughout my life.

# LIST OF PUBLICATIONS

## Journal Articles

1. **X. Wang**, P. -Y. Qin, and R. Jin, "Low RCS Transmitarray Employing Phase Controllable Absorptive Frequency-Selective Transmission Elements," *IEEE Transactions on Antennas and Propagation*, vol. 69, no. 4, pp. 2398-2403, Apr. 2021.
2. **X. Wang**, P.-Y. Qin, A. T. Le, H. Zhang, R. Jin, and Y. J. Guo, "Beam Scanning Transmitarray Employing Reconfigurable Dual-Layer Huygens Element," *IEEE Transactions on Antennas and Propagation*. (Under review)

## Conference Articles

1. **X. Wang**, P.-Y. Qin, and Y. J. Guo, "1-Bit Reconfigurable Huygens Element for Beam-Steering Transmitarrays," *26th International Symposium on Antennas and Propagation (ISAP)*, 2021, pp. 1-2, doi: 10.23919/ISAP47258.2021.9614579.
2. **X. Wang**, P.-Y. Qin, C. Ding and R. Jin, "Low RCS Transmitarray Using Phase Controllabe Rasorber," *2021 IEEE International Symposium on Antennas and Propagation and USNC-URSI Radio Science Meeting (APS/URSI)*, 2021, pp. 161-162, doi: 10.1109/APS/URSI47566.2021.9704697.

# CONTENTS


**1 Introduction** **1**

1.1 Background . . . . . 1

1.1.1 Transmitarray Antenna Concept . . . . . 1

1.1.2 Transmitarray Design Approaches . . . . . 3

1.2 Motivation . . . . . 8

1.3 Contributions . . . . . 9

1.4 Thesis Organization . . . . . 11

**2 Literature Review** **15**

2.1 High-Gain Low-RCS Antennas . . . . . 15

2.2 Wideband Conformal Transmitarrays . . . . . 21

2.3 Reconfigurable Transmitarrays for Beam Scanning . . . . . 28

**3 Low RCS Transmitarray** **35**

3.1 Introduction . . . . . 35

3.2 Phase Controllable AFST Element . . . . . 37

3.2.1 AFST Element . . . . . 37

3.2.2 Phase Controllable AFST Element Using Asymmetric Configuration . . . 39
3.2.3 Equivalent Circuit Model of Phase Controllable AFST Element . 40
3.2.4 Implementation of the Phase Controllable AFST Element . . . . . 42
3.3 Low RCS Transmitarray Antenna . . . . . 46
3.3.1 Low RCS Transmitarray Prototype Design and Implementation . 46
3.3.2 Numerical and Experimental Results of the Low RCS Transmitarray Antenna . . . . . 49
3.4 Summary . . . . . 54

**4 Wideband Conformal Transmitarray** **55**
4.1 Introduction . . . . . 55
4.2 Wideband Dual-Layer Huygens Element . . . . . 58
4.2.1 Dual-Layer Huygens Element . . . . . 58
4.2.2 Dual-Layer Tightly Coupled Huygens Element . . . . . 64
4.3 Wideband Conformal Transmitarray Antenna . . . . . 73
4.3.1 Wideband Conformal Transmitarray Prototype Design and Implementation . . . . . 73
4.3.2 Numerical and Experimental Results of the Wideband Conformal Transmitarray Antenna . . . . . 77
4.4 Summary . . . . . 78

**5 Reconfigurable transmitarray** **81**
5.1 Introduction . . . . . 81
5.2 1-Bit Reconfigurable Dual-Layer Huygens Element . . . . . 83
5.2.1 Dual-Layer Huygens Element Design . . . . . 83

5.2.2 Parametric Study . . . . . 87
5.2.3 PIN Diodes: Experimental Characterization and Modeling . . . . 89
5.2.4 Reconfigurable Dual-Layer Huygens Element with PIN Diodes . 92
5.3 Reconfigurable Transmitarray Antenna . . . . . 95
5.3.1 Reconfigurable Transmitarray Prototype Design . . . . . 95
5.3.2 Fabricated Prototype and Experimental Implementation . . . . . 98
5.3.3 Numerical and Experimental Results of the Reconfigurable Transmitarray Antenna . . . . . 100
5.4 Summary . . . . . 105

**6 Conclusions and Future Work** **107**
6.1 Conclusions . . . . . 107
6.2 Future Work . . . . . 109

**Bibliography** **110**

# List of Figures


1.1 Configuration of a transmitarray antenna. . . . . 2

1.2 Configuration of a M-FSS based transmitarray antenna. . . . . 3

1.3 Configuration of a receiver-transmitter based transmission element. . . . . 4

1.4 A dual-layer transmitarray element with periodic boundaries and Floquet ports in ANSYS Electromagnetics software. . . . . 5

1.5 Simulated transmission coefficients of a dual-layer element with different values of scale factor $k$ at 78 GHz. (a) Transmission magnitudes. (b) Transmission phases. . . . . 6

1.6 Transmission phase distribution on the aperture of a transmitarray. . . . . 7

2.1 A low RCS and high-gain patch antenna based on a holographic metasurface [20]. (a) Element configuration of the holographic metasurface. (b) Configuration of the low RCS and high-gain patch antenna. . . . . 16

2.2 A slot antenna arrays with wideband RCS reduction [22]. (a) Frequency responses of the element. (b) Exploded view of 4×4 microstrip slot antenna array. . . . . 17

2.3 (a) Geometry of periodic AMC structure patterns [25]. (b) One period of the square checkerboard surface. . . . . 18

2.4 Periodic element of reflectarray element [27]. . . . . 18

2.5 (a) Configuration of absorptive frequency-selective reflection structure element. (b) The prototype of the low-RCS reflectarray [29]. . . . . 19

2.6 (a) Configuration of the band-notched absorber element. (b) Configuration of the low-RCS transmitarray unit cell. (c) Photograph of the low-RCS reflectarray antenna [30]. . . . . 20

2.7 (a) Top view and (b) side view of the square perforated element. (c) The geometry of cylindrical perforated concave transmitarray. (d) The geometry of cylindrical perforated convex transmitarray [35]. . . . . 22

2.8 (a) OFF state, (b) ON state, (c) layer stackup of the unit cell. (d) Transmitarray structure [36]. . . . . 22

2.9 (a) Curved 4-layer transmission element and its transmission phases. (b) Cylindrically conformal transmitarray with a feed horn antenna [40]. . . . 23

2.10 (a) Top view and (b) side view of the ultra-thin triple-layer slot element. (c) 3-D view of the cylindrically conformal transmitarray antenna [37]. . . 24

2.11 (a) Top and bottom layers; (b) 3-D structure of the dual-layer Huygens element. (c) High-efficiency dual-layer conformal transmitarray structure [39]. . . . . 25

2.12 (a) Curve wideband element. (b) Cylindrically conformal transmitarray with a log-periodic dipole feed antenna [38]. . . . . 26

2.13 The configurations of (a) the dual-layer malta-cross element with metallic vias [41] and (b) the dual-layer CP element without metallic vias [43]. . . 26

2.14 The configuration of a dual-layer Huygens element [44]. . . . . 27

2.15 The configurations of (a) a triple-layer transmitarray element [48] and (b) a six-layer transmitarray element [49]. . . . . 28

2.16 1-bit electronically reconfigurable element [14]. (a) Side view. Top view of an element with (b) 1 biasing line, or (c) 10 biasing lines. . . . . 29

2.17 (a) CP transmitarray element architecture [57]. (b) Receiver unit. (c) Transmitter unit. . . . . 30

2.18 Reconfigurable element design [13]. . . . . 31

2.19 (a) A 4-layer reconfigurable element integrated with two PIN diodes [60]. (b) A 5-layer FSS element integrated with 3 varactor diodes on each layer [61]. (c) A five stacked layers of square-slot FSS element integrated with 2 varactor diodes on each layer [62]. . . . . 32

3.1 Conceptual depiction of a low RCS transmitarray. . . . . 36

3.2 Configuration of the AFST element. Top view of (a) top layer and (b) bottom layer. (c) 3D view and (d) side view of the AFST element. . . . . 38

3.3 Transmission and reflection magnitudes of the AFST unit cell. . . . . 38

3.4 Configuration of the phase controllable AFST element. (a) Top side of the first substrate. (b) Top or bottom side of the second substrate. (c) HFSS model of the phase controllable AFST element. . . . . 39

3.5 Equivalent circuit of the phase controllable AFST element. . . . . 41

3.6 Simulated results of the phase controllable AFST element. (a) Simulated transmission magnitudes. (b) Simulated transmission phases. (c) Simulated reflection magnitudes. . . . . 43

3.7 Simulated transmission coefficients of the phase controllable AFST element with Layer 3 removed. (a) Magnitudes. (b) Phases. . . . . 44

3.8 The schematic of the Low RCS transmitarray antenna. . . . . 45

3.9 Simulated reflection magnitudes of the phase controllable AFST element without resistors. . . . . 45

3.10 The prototype of the proposed low-RCS transmitarray. (a) Schematic of low-RCS transmitarray with a feed horn antenna. (b) Exploded view of the proposed low-RCS transmitarray. . . . . 47

3.11 Calculated transmission phase distribution of low-RCS transmitarray and reference transmitarray. . . . . 48

3.12 Photographs of the fabricated low-RCS transmitarray. (a) Front side. (b) Back side. . . . . 48

3.13 Simulated and measured reflection coefficients of low-RCS transmitarray and reference transmitarray. . . . . 49

3.14 Radiation patterns and realized gains versus frequency of low-RCS transmitarray and reference transmitarray. (a) E-plane radiation patterns at 12.5 GHz. (b) H-plane radiation patterns at 12.5 GHz. (c) Realized gains versus frequency. (d) Aperture efficiencies versus frequency. . . . . 50

3.14 Radiation patterns and realized gains versus frequency of low-RCS transmitarray and reference transmitarray. (a) E-plane radiation patterns at 12.5 GHz. (b) H-plane radiation patterns at 12.5 GHz. (c) Realized gains versus frequency. (d) Aperture efficiencies versus frequency. . . . . 51

3.15 Monostatic RCS of low-RCS transmitarray and reference transmitarray under normal impinging wave. (a) Vertical polarization. (b) Horizontal polarization. . . . . 52

3.16 Measured monostatic RCS of two transmitarrays under wide-angle oblique impinging waves. (a) Reference transmitarray. (b) Low-RCS transmitarray. . . . . 53

4.1 Configuration of the simple dual-layer Huygens element. (a) Top view. (b) Bottom view. (c) 3D view. . . . . 56

4.2 Transmission coefficients of the simple dual-layer Huygens element. . . . 57

4.3 (a) Equivalent circuit model of the simple dual-layer Huygens element. (b) Even mode decomposed circuit. (c) Odd mode decomposed circuit. The values of the parameters are as follows: $L_e$ = 3.26 nH, $L_o$ = 2.73 nH, $C_1$ = 1.89 fF. $C_2$ = 0.55 fF, $Z_0$ = 377 , $Z$ = 254 , $\theta$ = 60.58° and $R$ = 1.77 Ω. 59

4.4 Induced surface currents on top and bottom layers of the simple dual-layer Huygens element in a time period T. . . . . 60

4.5 (a) Electric field of the simple dual-layer Huygens element on xoz plane at t = 0 and t = T/2. (b) Surface and displacement currents of the simple dual-layer Huygens element on xoz-plane at t = -T/4(3T/4) and t = T/4. . 61

4.6 Transmission coefficients of the simple dual-layer Huygens element with different values of scale factor $k$. (a) Magnitudes. (b) Phases. . . . . 62

4.7 Configuration of the dual-layer tightly coupled Huygens element. (a) Top view. (b) Bottom view. (c) 3D view. . . . . 63

4.8 Transmission coefficients of the dual-layer tightly coupled Huygens element. . . . . 64

4.9 Induced surface current distributions on top and bottom layers of the dual-layer tighly coupled Huygens element at 71 GHz. . . . . 65

4.10 Induced surface current distributions on top and bottom layers of the dual-layer tighly coupled Huygens element at 78.5 GHz. . . . . 66

4.11 Induced surface current distributions on top and bottom layers of the dual-layer tighly coupled Huygens element at 86 GHz. . . . . 67

4.12 Transmission coefficients of the dual-layer tightly coupled Huygens element with different values of scale factor $k$. (a) Magnitudes. (b) Phases. . 68

4.13 Cylindrically conformal transmitarray antenna: (a) 3D view; (b) schematic of front view. (c) The No. of the scale factor $k$ distributions on a quarter of the transmitarray. . . . . 70

4.14 Photographs of the fabricated wideband conformal transmitarray antenna. 71

4.15 Measured and simulated reflection magnitudes of the wideband conformal transmitarray antenna. . . . . 73

4.16 Measured and simulated realized gain patterns of the wideband conformal transmitarray antenna in E and H planes at different frequencies. (a) 72 GHz. (b) 74 GHz. (c) 76 GHz. (d) 78 GHz. (e) 80 GHz. (f) 82 GHz. (g) 84 GHz. (h) 86 GHz. . . . . 74

4.16 Measured and simulated realized gain patterns of the wideband conformal transmitarray antenna in E and H planes at different frequencies. (a) 72 GHz. (b) 74 GHz. (c) 76 GHz. (d) 78 GHz. (e) 80 GHz. (f) 82 GHz. (g) 84 GHz. (h) 86 GHz. . . . . 75

4.16 Measured and simulated realized gain patterns of the wideband conformal transmitarray antenna in E and H planes at different frequencies. (a) 72 GHz. (b) 74 GHz. (c) 76 GHz. (d) 78 GHz. (e) 80 GHz. (f) 82 GHz. (g) 84 GHz. (h) 86 GHz. . . . . 76

4.17 Measured and simulated realized gains and aperture efficiencies of the wideband conformal transmitarray antenna versus frequencies. . . . . 78

5.1 Configuration of the dual-layer Huygens element. (a) Top view. (b) Bottom view. (c) 3D view. . . . . 83

5.2 Transmission coefficients of the dual-layer Huygens element under the incidence waves with different angles. . . . . 84

5.3 Simulated current distributions on top and bottom layers of the dual-layer Huygens element. . . . . 86

5.4 Transmission coefficients of the dual-layer Huygens element with different values of parameter $a$. (a) Magnitudes. (b) Phases. . . . . 87

5.5 Transmission coefficients of the dual-layer Huygens element with different values of parameter $l$. (a) Magnitudes. (b) Phases. . . . . 88

5.6 Transmission magnitudes of the dual-layer Huygens element with different thickness $h$ of the dielectric substrate. . . . . 89

5.7 (a) Fabricated fixture for the experimental characterization of the PIN diode. Equivalent models of the PIN diode under (b) forward bias; (c) reverse bias. . . . . 90

5.8 De-embedded and fitted results of the PIN diode under (a) forward bias; (b) reverse bias. . . . . 91

5.9 *S*-parameters of the equivalent circuits of the PIN diode. . . . . 91

5.10 Configurations of the 1-bit reconfigurable dual-layer Huygens element. (a) Top view; (b) bottom view; (c) 3D view of the element with 4 biasing lines. (d) Top view; (e) bottom view of the element with 20 biasing lines. (f) Top view of a part of the whole transmitarray. . . . . 93

5.11 Transmission coefficients of the reconfigurable dual-layer Huygens element with 4 or 20 biasing lines under ON and OFF states. (a) Magnitudes. (b) Phases. . . . . 94

5.12 (a) Schematic diagram of the phase compensation for a radiated beam in a desired direction. (b) The 10×10 reconfigurable transmitarray with its scanning-control board. . . . . 96

5.13 Simulated radiation patterns for different scan angles at 13 GHz in (a) E-plane and in (b) H-plane. . . . . 98

5.14 Photographs of (a) the fabricated reconfigurable transmitarray antenna (RTA) prototype and (b) the experimental setup of the RTA mounted in the anechoic chamber. . . . . 99

5.15 Measured and simulated input reflection magnitudes of the transmitarray radiating towards boresight. . . . . 100

5.16 (a) Measured and simulated boresight radiation patterns in E and H planes at 12.8 GHz. (b) Measured and simulated realized gains in boresight direction versus frequencies. . . . . 101

5.17 Measured radiation patterns for different scanning angles at 12.8 GHz in (a) E plane and (b) H plane. . . . . 102

5.18 Measured cross-polarization radiation patterns for different scanning angles at 12.8 GHz in E and H planes. . . . . 104

# LIST OF TABLES


3.1 Comparison of Relevant Transmitarray (TA), Reflectarrays (RAs) or Patch Antenna . . . . . 53

4.1 Transmission Losses and Phase Coverages of the Dual-Layer Tightly Coupled Huygens Element at Different Frequencies . . . . . 69

4.2 Transmission Losses and Phases of the Dual-Layer Tightly Coupled Huygens Element with Different Values of Scale Factor $K$ at 78 GHz . . . . . 72

4.3 Comparison Between Reported Transmitarray Antennas . . . . . 77

5.1 Transmission Magnitudes and Phases of the 1-Bit Dual-Layer Huygens Element with Four Biasing Lines at 13 GHz . . . . . 95

5.2 Beam Scanning Performance of the Reconfigurable Transmitarray in E Plane . . . . . 103

5.3 Beam Scanning Performance of the Reconfigurable Transmitarray in H Plane . . . . . 103

5.4 Comparison Between the Reconfigurable Transmitarray Antennas . . . . 104

# List of Acronyms

| | |
|---|---|
| **2-D** | 2-Dimensional |
| **3-D** | 3-Dimensional |
| **5G** | Fifth Generation |
| **6G** | Sixth Generation |
| **AFST** | Absorptive Frequency-Selective Transmission |
| **AMC** | Artificial Magnetic Conductor |
| **BW** | Bandwidth |
| **CP** | Circular-Polarization |
| **DC** | Direct Current |
| **EM** | Electromagnetic |
| **FPGA** | Field-Programmable Gate Array |
| **FSR** | Frequency-Selective Rasorber |
| **FSS** | Frequency-Selective Surface |
| **Gbps** | Gigabits-Per-Second |
| **IDC** | Insulation-Displacement Contact |
| **LED** | Light-Emitting Diode |
| **LP** | Linear-Polarization |
| **MEMS** | Micro-Electro-Mechanical System |
| **M-FSS** | Multilayer-Frequency-Selective Surface |
| **mm-wave** | Millimeter Wave |
| **MVG** | Microwave Vision Group |

| | |
|---|---|
| **PCB** | Printed Circuit Board |
| **PEC** | Perfect Electric Conductor |
| **RCS** | Radar Cross Section |
| **RF** | Radio Frequency |
| **RTA** | Reconfigurable Transmitarray |
| **RTE** | $\text{TE}^y$ Plane Wave |
| **RTM** | $\text{TM}^y$ Plane Wave |
| **SLL** | Side Lobe Level |
| **Tbps** | Terabits-Per-Second |
| **THz** | Terahertz |
| **UAV** | Nnmanned Aerial Vehicles |
| **USB** | Universal Serial Bus |
| **VNA** | Vector Network Analyzer |

# 1 Introduction

## 1.1 Background

### 1.1.1 Transmitarray Antenna Concept

During the last decade, transmitarray antennas have attracted a lot of interest due to their merits of high-gain, spatial feeding network and low-cost for long-distance communications in many emerging applications especially at millimeter-wave frequencies.

A high-gain antenna is usually designed by two methods: the optic theory and the array method. Based on the optical theory, the radiation beam can be focused by manipulating the surface curvature of an antenna, such as a reflector antenna and a lens antenna. However, the curved surface of a reflector antenna or a lens antenna increases the fabrication complexity and the architecture volume which limit its applications. By using the array method, high-gain can be achieved with the increased aperture size, such as printed microstrip antenna arrays, but complex feeding networks are required. As an

emerging concept, transmitarray antennas can combine the advantages of the optic theory and the array method which is based on utilizing the low cost standard printed circuit board (PCB) technique and make them lightweight, high-gain, high efficiency, flexible radiation performance and feasible to integrate active devices for reconfiguration.

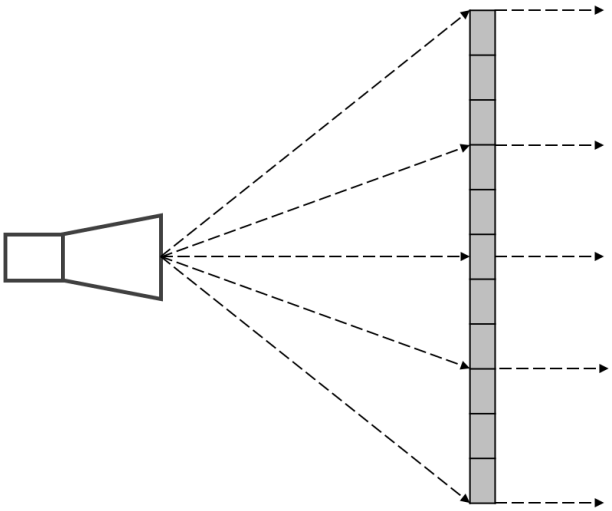

Figure 1.1: Configuration of a transmitarray antenna.

As illustrated in Fig. 1.1, Transmitarray antennas typically consist of a focal source illuminating an array of sub-wavelength transmission elements with designed phase distribution across the aperture. A horn antenna is usually selected to be located on the focal point as a feeding source. An array of sub-wavelength transmission elements is named as a transmitarray, which can convert the original spherical electromagnetic waves of the feeding source into a specified radiation pattern. For example, it can convert spherical waves of the feed horn into plane waves of a desired direction with high gain and narrow beamwidth.

Compared with a reflectarray antenna, a transmitarray antenna does not have the effects of the feed blockage but more challenge in the design procedure [1–3]. In a reflectarray, the reflection magnitude keeps close to 1 due to the presence of a metallic ground plane; thus, only the reflection phase needs to be controlled. In contrary, in a transmitarray, both transmission magnitudes and phases of the elements on the aperture need to be controlled. The transmission magnitudes should be close to 1 in order to achieve high

gain and high aperture efficiency.

### 1.1.2 Transmitarray Design Approaches

A general design procedure of a transmitarray antenna is composed of two steps: transmission element design and transmitarray prototype design.

#### 1.1.2.1 Transmission Element Design

The transmission magnitude of a transmission element needs to be close to 1, and the transmission phase coverage usually needs to be 360°. In the transmission element design, a proper element type needs to be selected and the element dimensions for certain transmission phase and magnitude requirements need to be determined.

There are three different approaches for transmitarray element designs: multilayer frequency-selective surface (M-FSS), receiver-transmitter, and metasurface approaches.

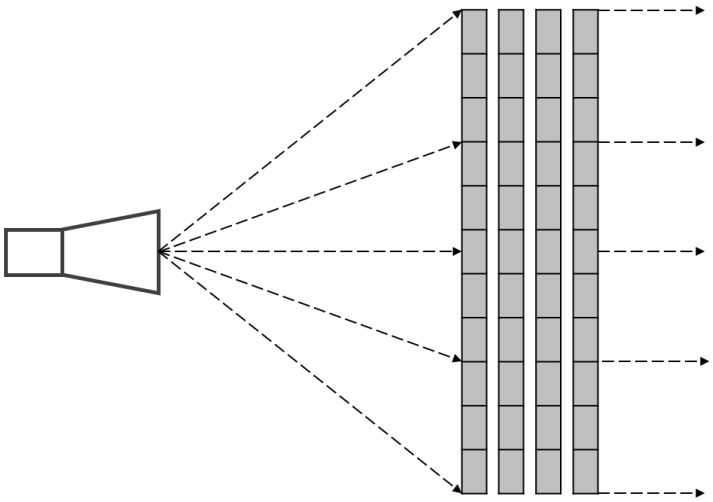

Figure 1.2: Configuration of a M-FSS based transmitarray antenna.

The multilayer frequency-selective surface (M-FSS) approach is usually used to individually control the transmission magnitude and phase of each element in the array by changing the dimensions of the element [4–8]. However, only one layer of printed transmission element array cannot achieve a full 360° phase compensation [4]. Therefore, to

increase the transmission phase coverage of the array, a multilayer design in which each layer is separated by either an air spacer or a dielectric material is required, as shown in Fig. 1.2.

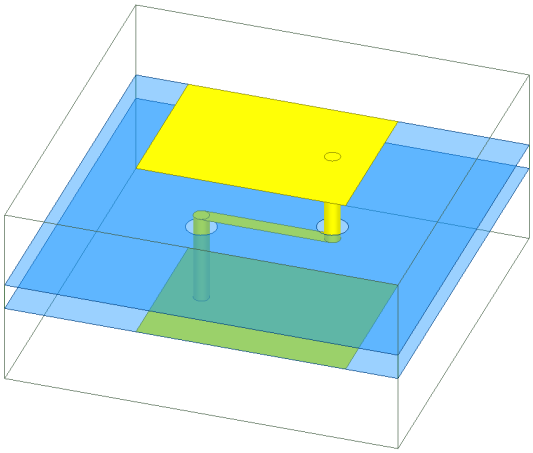

Figure 1.3: Configuration of a receiver-transmitter based transmission element.

A receiver-transmitter configuration is typically composed of three parts: a receiver, a transmitter and a phase shifter. The receiver and transmitter are usually two planar arrays of printed antennas, and their elements are coupled or interconnected by the phase shifter. The receiver array is illuminated by the antenna feed source. The phase shifter array is designed to achieve a desired magnitude and phase distribution from the receiver array to the transmitter array [9–14]. The configuration of a receiver-transmitter element is shown in Fig. 1.3. Using this method, if the outer two layers are designed as wideband working element, then it would be easier to realize a wideband transmitarray element design when choosing a true time delay line between them for phase adjustment.

The metasurface approach controls the transmission phase of each element in the array by varying the effective permittivity and permeability of its metasurface configuration [15, 16]. The difficulties of this method are the complicated theory and synthesis procedure. However, it is capable for full-range phase control without reflection and polarization loss, as well as a pretty low profile with subwavelength dimension.

Three different approaches above show how to control the transmission phases of transmitarray elements. Moreover, based on these three transmitarray design approaches,

a parametric study of the unit-cell element is usually performed to obtain the desired transmission coefficients of the elements. The transmitarray element should be simulated in periodic boundaries, as shown in Fig. 1.4, to simulate an infinite array of the element, which can be analyzed by most electromagnetic simulators. For a transmitarray, the transmission magnitudes and phases of the elements can be obtained by using an electromagnetic simulator with periodic boundary conditions.

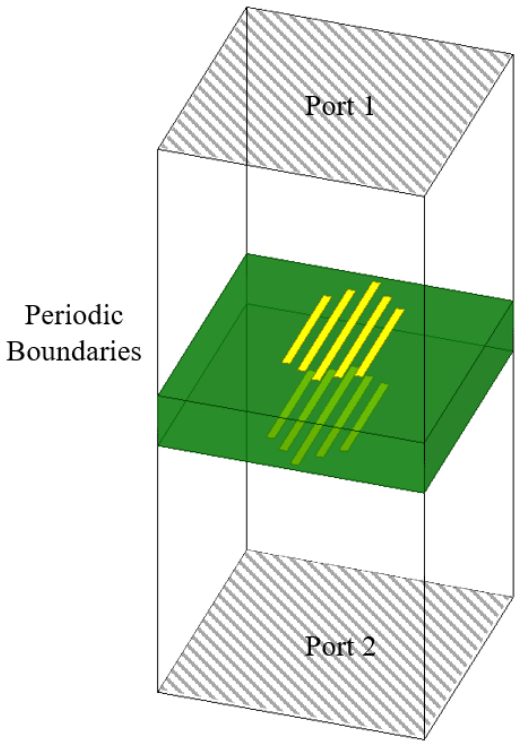


Figure 1.4: A dual-layer transmitarray element with periodic boundaries and Floquet ports in ANSYS Electromagnetics software.

For example, Fig. 1.5 depicts the simulated transmission magnitudes and phases vs. each stripline length's scale factor $k$ of the unit-cell element shown in Fig. 1.4, and the operating frequency is 78 GHz. It is observed that when the scale factor $k$ changes, a 432° phase change is achieved while the transmission loss is less than -1 dB.

#### 1.1.2.2 Transmitarray Prototype Design

As we known, a transmitarray antenna typically consist of a focal source illuminating an array of sub-wavelength transmission elements. The basis of a transmitarray antenna

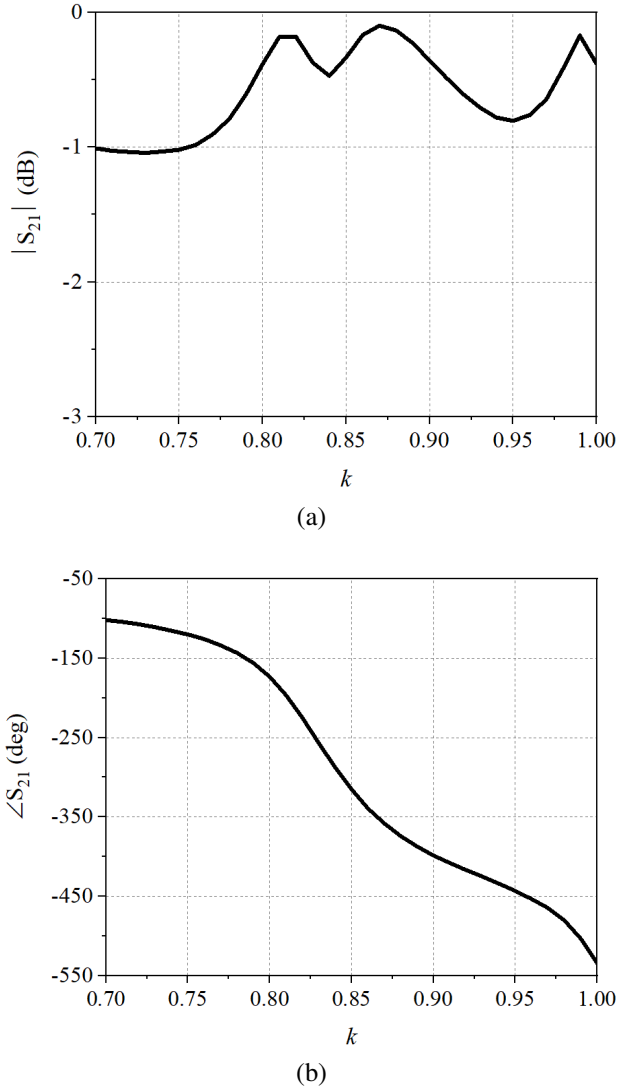


Figure 1.5: Simulated transmission coefficients of a dual-layer element with different values of scale factor $k$ at 78 GHz. (a) Transmission magnitudes. (b) Transmission phases.

analysis is the assumption that all transmitarray elements are located in the far-field area of the feed source. Therefore, the incident electromagnetic waves from the feed source to each transmitarray element at a specific angle can be seen as a spherical wave propagation which means the transmission phase is proportional to the distance between the phase center of the feed source and each element.

In the transmitarray antenna system design, the aperture size and feed location can be first determined for a certain gain requirement through the gain and efficiency analysis. When associated with the beam direction or radiation pattern specifications, the transmission phase compensation over the aperture can be calculated. Each element should be

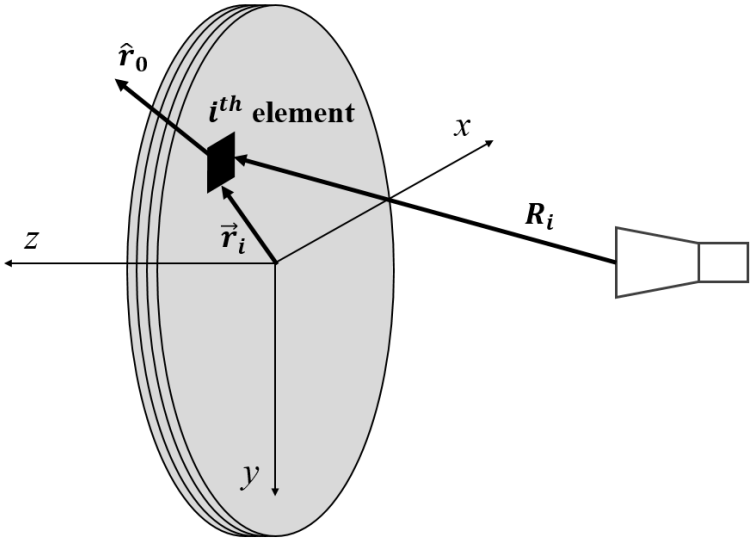


Figure 1.6: Transmission phase distribution on the aperture of a transmitarray.

designed to compensate the spatial phase delay from the phase center of the feed source to the element to achieve a specific phase distribution for a desired radiation pattern, as shown in Fig. 1.6. The transmission phase $\phi_i$ on the $i^{th}$ element can be calculated as follows [17, 18]:

$$\phi_i = k(R_i - \vec{r}_i \cdot \hat{r}_0) + \phi_0 \tag{1.1}$$

where $k$ is the propagation constant in free space, $R_i$ is the distance from the phase center of the feed antenna to the $i^{th}$ element, $\vec{r}_i$ is the position vector of the $i^{th}$ element, and $\hat{r}_0$ represents the direction of the radiation beam, and $\phi_0$ is a constant reference phase.

From the phase compensation, the transmission element geometry can be decided for prototype fabrication and measurement. Also from the phase compensation, both the aperture field and far field of a transmitarray antenna can be computed through the radiation analysis. To calculate the radiation performance of a transmitarray, different radiation analysis techniques have been developed.

A simple and straightforward method is the array theory approach. Each transmission element has an excitation magnitude and phase. The magnitude is determined by the feed pattern and the distance between the feed and the element. The phase is the sum of the incident wave phase and the element transmission phase. Once the excitation magnitude

and phase are determined for each element, the far-field radiation pattern can be determined through array summation. This method provides a fast calculation of the radiation pattern and is quite accurate around the main beam region.

To obtain a more rigorous result, more advanced approaches can be used, such as the aperture field method and the full-wave simulation of the entire antenna. Once the radiation pattern is obtained, some characteristics parameters of the transmitarray antenna can be computed, such as gain, efficiency, beamwidth, sidelobe levels, and cross-polarization levels.

## 1.2 Motivation

Transmitarray antennas have attracted increasing attention in long-distance communications for space and terrestrial wireless communication systems due to their merits of high gain, low cost and flexible radiation performance, which can be a good antenna candidate for the fifth generation (5G) and beyond wireless networks with the requirements of high gain and low cost at millimeter-wave (mm-wave) and terahertz (THz) bands [19]. Although theoretical study and practical design of transmitarrays have been greatly developed, there are still some challenges that exist for transmitarrays to fulfill the requirements in future wireless communications.

Firstly, high-gain antennas are essential to achieving long-distance communications in space and terrestrial systems. In order to obtain high gains, a large antenna aperture is required, but this increases the scattering area as well, which would normally lead to high RCS unfortunately. Since transmitarrays can achieve high gains without using complex and lossy feed networks, they have been widely hailed as competitive high gain antenna candidates. Consequently, it is very desired but challenging to design a transmitarray antenna with both high-gain and low-RCS properties.

Secondly, conformal transmitarrays are developed to achieve aerodynamic requirements of many mounting wireless communication platforms, e.g., satellites, aircrafts and

unmanned aerial vehicles (UAVs). A conformal transmitarray is designed to adapt the shape of a mounting platform, which can be a part of the platform surface and accommodate a feeding antenna placed behind the transmitarray to utilize platform space better without destroying its aerodynamic performance. Based on the current fabrication technology, it is highly desirable to develop dual-layer transmitarray without vertical metallic vias. However, the bandwidths of the currently reported dual-layer transmitarrays are limited. Thus, it is very challenging to improve the bandwidth of a dual-layer transmitarray for conformal applications.

Thirdly, electronically reconfigurable antennas have attracted much attention in many emerging applications at microwaves and millimeter waves, such as satellite communications and automotive radar systems, due to the capabilities of 2-D beam steering and beam synthesis. The traditional high-gain electronically reconfigurable antennas are the phased arrays. However, the phased arrays require a large number of phase shifters which strongly increase the system complexity and fabrication cost. Compared to the phased arrays, reconfigurable reflectarray antennas and reconfigurable transmitarray antennas have spatial feeding architecture instead of complex feeding network, which can achieve excellent 2-D beam steering and beam synthesis performance by independently controlling the reflection and transmission phases of the elements on the apertures, respectively. Contrary to reflectarray antennas, transmitarray antennas do not have the disadvantage of blockage effect, which can be a good candidate for high-gain electronically reconfigurable antennas.

## 1.3 Contributions

This work aims to tackle the challenges discussed above and provide new approaches for the advanced transmitarray and their beam scanning. Major contributions are summarized as follows:

The firstly contribution is the improvement of the AFST element. The currently reported AFST elements have the same transmission phases, focusing on periodic surface

designs. However, for transmitarray designs, the elements need to provide a digital or continuous phase change to achieve collimated or shaped beams. Actually, it is very challenging to manipulate the phase response of the AFST elements as the phase response is usually related to the element's absorption and transmission performance. The state-of-the-art of AFST elements is significantly extended by developing a phase controllable AFST element. The element can achieve a 1-bit phase change in the transmission band. Then, a low-RCS transmitarray is developed by using the phase controllable AFST element without sacrificing its radiation performance. Significant RCS reductions have been achieved at lower and upper absorption bands outside the transmission band under normal and wide-angle oblique impinging waves for dual polarization.

The second contribution is the improvement of dual-layer transmitarray. The current reported dual-layer transmitarrays without metallic vias achieve full phase range by rotating the elements for circular polarization or employing dual-layer Huygens elements, but these approach is limited by circular polarization or bandwidth, which is not suitable in many applications, e.g., E-band satellite communication. Actually, there is always a tradeoff between the layer amount of the transmitarray and its gain bandwidth. It is very challenging to improve the bandwidth of a dual-layer transmitarray for conformal applications. The element consists of five pairs of partly overlapped metallic striplines with different lengths printed on two layers of a dielectric substrate, which can provide tightly coupled Huygens resonances with nearly total transmission and full transmission phase coverage in a wide bandwidth. A cylindrically conformal transmitarray at 78 GHz is designed, fabricated and measured. Continuous phase compensation of 360° is achieved by tuning the lengths of the striplines, reducing phase errors of the array architecture. The 3-dB bandwidth can fully cover the E-band spectrum.

The third contribution is the improvement of electronic beam scanning transmitarray. Most of the currently reported reconfigurable transmitarray elements have more than three metallic layers with several metallic vias. Such configurations may lead to complex fabrication and package processes, which could affect the performance of transmitarrays. Hence, it is highly desirable to design dual-layer reconfigurable transmitarray elements

without metallic vias, which can also facilitate the design of large-size arrays at higher frequencies. The developed Huygens element is composed of two metallic crosses which enables a near non-reflection response. Moreover, the element can achieve a 1-bit phase compensation with low transmission loss by controlling two PIN diodes on the element. Compared with many other reconfigurable transmitarray elements using multi-layer structures with metallic vias, the proposed reconfigurable Huygens element has a simpler configuration and a simpler biasing network, and it is not affected by multi-layer alignment errors. By employing the dual-layer reconfigurable Huygens element, a novel electronic beam scanning transmitarray antenna is developed. Although the structure of the proposed element is simpler, the performance of the transmitarray is comparable to or even better than those of mostly reported beam scanning transmitarray antennas.

## 1.4 Thesis Organization

This thesis is organised as follows:

- *Chapter 1*: This chapter presents the background and motivation of the research problem and the main contributions of this work.

- *Chapter 2*: This chapter presents a detailed literature review on low RCS antennas, wideband conformal transmitarrays and reconfigurable transmitarrays.

- *Chapter 3*: This chapter presents a low RCS transmitarray using phase controllable AFST elements. The element consists of asymmetrical resonators with resistors to obtain an absorption-transmission-absorption response. The transmission phase within the transmission band can be controlled by rotating the AFST elements, achieving a 1-bit phase change. A low-RCS transmitarray using the developed elements is designed, fabricated and measured. Compared with a reference transmitarray, the radiation performance of the low-RCS one is almost unchanged with a realized gain of 24.4 dBi. Significant RCS reductions have been realized for dual

polarizations of the impinging EM waves. The 10 dB RCS reduction bandwidths are 18 % and 14 % for the lower and upper absorption bands, respectively.

- *Chapter 4*: This chapter presents a wideband conformal transmitarray employing dual-layer tightly coupled Huygens elements for E-band high data rate communication. The element consists of five pairs of partly overlapped metallic striplines with different lengths printed on two layers of a dielectric substrate, which can provide tightly coupled Huygens resonances with nearly total transmission and full transmission phase coverage in a wide bandwidth. To validate the design concept, a cylindrically conformal transmitarray at 78 GHz is designed, fabricated and measured. Continuous phase compensation of 360° is achieved by tuning the lengths of the striplines, reducing phase errors of the array architecture. Good agreement between the measured and simulated results is found, showing a peak measured realized gain of 26.6 dBi with an aperture efficiency of 35.9 % and measured 3-dB bandwidth of 20.4 % from 71 to 87 GHz, fully covering the E-band spectrum from 71 to 86 GHz.

- *Chapter 5*: This chapter presents a Ku-band electronic 2-D beam scanning transmitarray employing a new reconfigurable dual-layer Huygens element. The Huygens element consists of two metallic crosses printed on two layers of a dielectric substrate. A 1-bit phase compensation with low transmission loss is achieved by controlling two PIN diodes integrated on the element. Compared with many other reconfigurable transmitarray elements using multi-layer structures with metallic vias, the developed reconfigurable Huygens element has a simpler biasing network and is not affected by multi-layer alignment errors. This particularly facilitates large aperture array at higher frequencies. To validate the design concept, a transmitarray prototype at 13 GHz is designed and fabricated. The measured results agree well with the simulated ones, showing 2-D scanning beams within $\pm 50°$ in E-plane and $\pm 40°$ in H-plane. A maximum realized gain of 18.4 dBi is obtained.

- *Chapter 6*: This chapter concludes the thesis by summarizing the achievements of the work. Future work and plans to further develop this research topic are also discussed.

# 2

# Literature Review

## 2.1 High-Gain Low-RCS Antennas

High-gain antennas are essential to achieving long-distance communications in space and terrestrial systems. In order to obtain high gains, a large antenna aperture is required, but this increases the scattering area as well, which would normally lead to high RCS unfortunately.

Recently, many efforts have been devoted to high-gain and low-RCS antennas using metasurface [20,21], superstrate layers [22–24] to absorb the impinging waves or artificial magnetic conductors (AMCs) [25,26] to deviate the impinging waves. In [20], a low RCS patch antenna based on a holographic metasurface is proposed, as shown in Fig. 2.1.

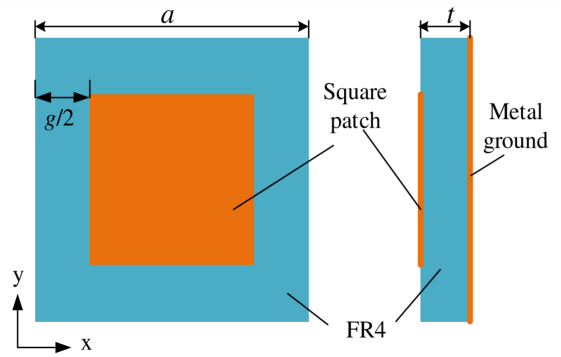


(a)

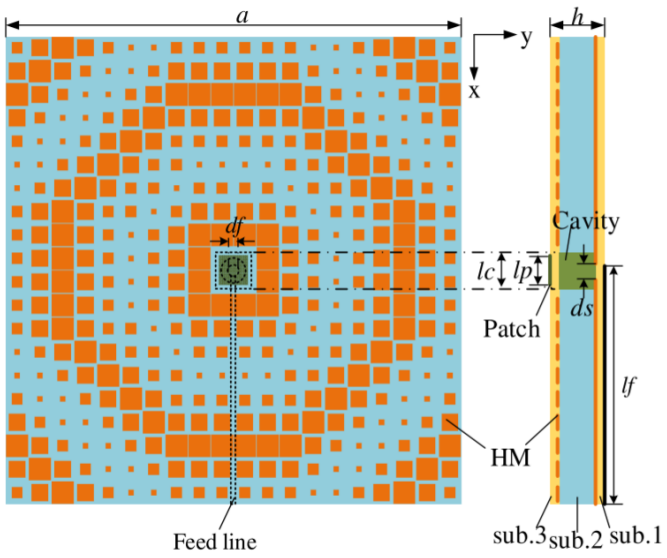


(b)

Figure 2.1: A low RCS and high-gain patch antenna based on a holographic metasurface [20]. (a) Element configuration of the holographic metasurface. (b) Configuration of the low RCS and high-gain patch antenna.

As a parasitic structure of the antenna, the holographic metasurface can effectively increase the antenna radiation aperture; thus, a relatively high gain is obtained. At the same time, the holographic metasurface has the ability to transform a propagating wave into a surface wave. Therefore, the backscattering is greatly reduced, resulting in a low monostatic RCS. In [22], a slot antenna arrays with wideband RCS reduction employing a periodic resistive surface in front of the radiating apertures is proposed, as shown in Fig. 2.2. It is shown that a remarkable reduction of the monostatic and bistatic RCS of the proposed structures for normal and oblique incidence waves can be accomplished over a frequency band as wide as two octaves.

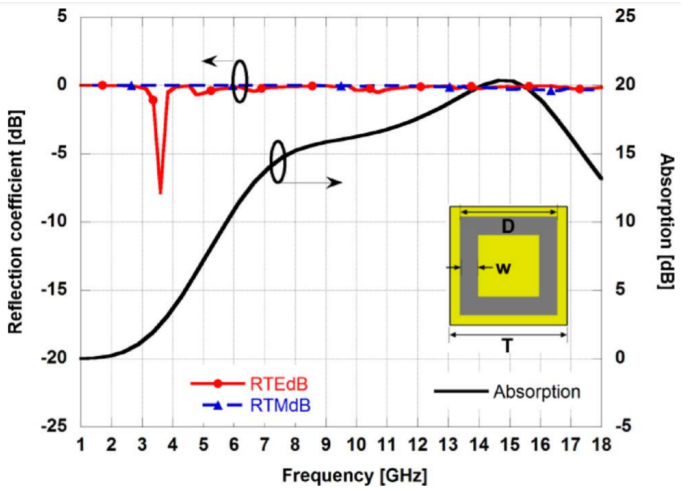


(a)

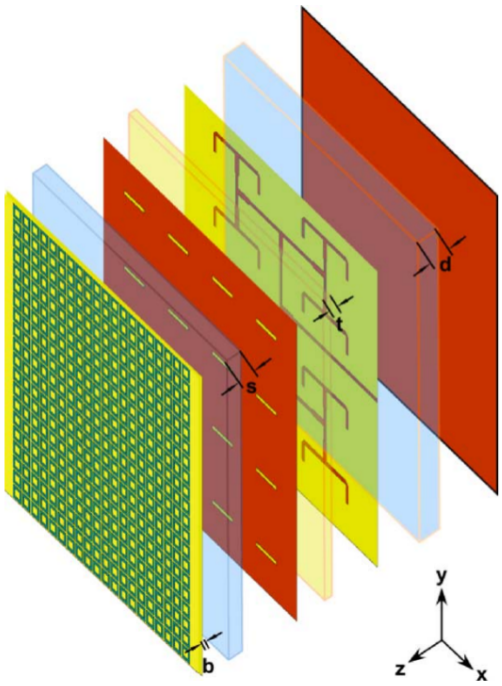


(b)

Figure 2.2: A slot antenna arrays with wideband RCS reduction [22]. (a) Frequency responses of the element. (b) Exploded view of 4×4 microstrip slot antenna array.

In [25],a method for wideband RCS reduction by designing checkerboard surfaces using strategically placed AMCs is proposed. The cross frame and folded cross dipoles are chosen as the patterns of two AMCs, the prototype of the checkerboard surface (comprised of the two AMCs) is shown in Fig. 2.3.

Since reflectarrays and transmitarrays can achieve high gains without using complex

and lossy feed networks, they have been widely hailed as competitive high gain antenna candidates. Some effective methods have been utilized to reduce the RCS of reflectarrays.

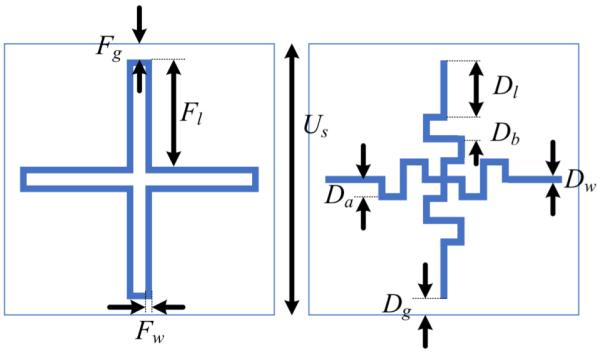


(a)

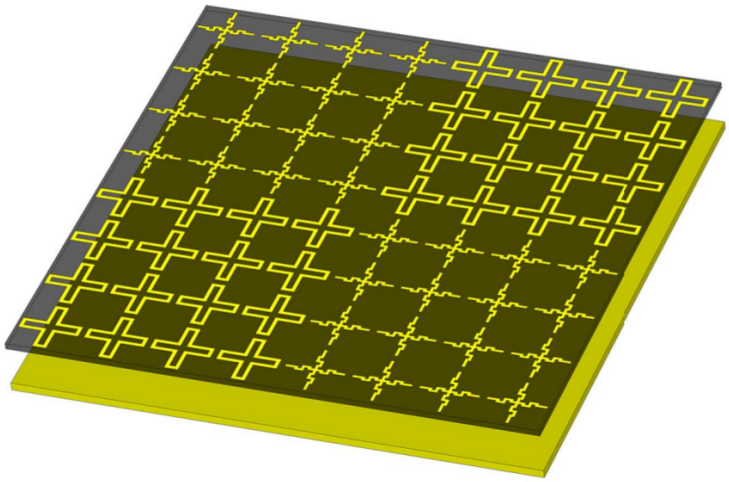

(b)

Figure 2.3: (a) Geometry of periodic AMC structure patterns [25]. (b) One period of the square checkerboard surface.

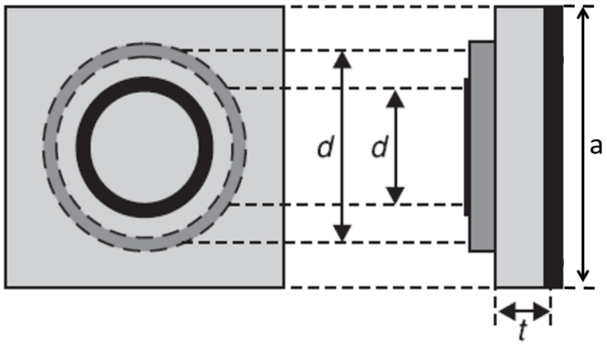


Figure 2.4: Periodic element of reflectarray element [27].

These methods can be classified into three types. The first one is to replace the ground plane of the reflectarray with a bandstop FSS [27]. The bandstop FSS behaves as a normal ground plane within the operating band while being transparent for the impinging waves at the out-of-band frequencies, as shown in Fig. 2.4. However, in practice, the FSS-backed reflectarray antenna is not suitable to be mounted on a application platform, because the transmitted out-of-band waves may cause interference for the back-side systems, such as the transceiver system or other circuits, or even damaging [28].

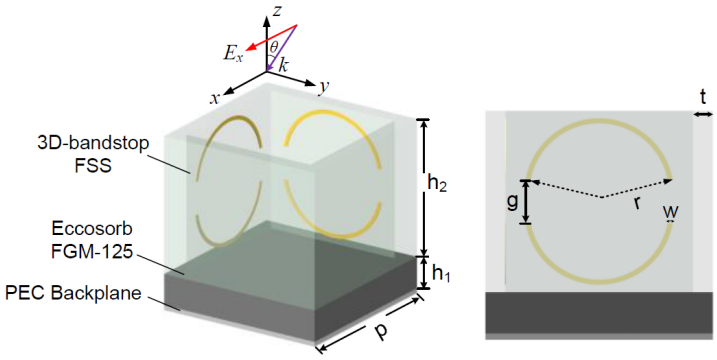


(a)

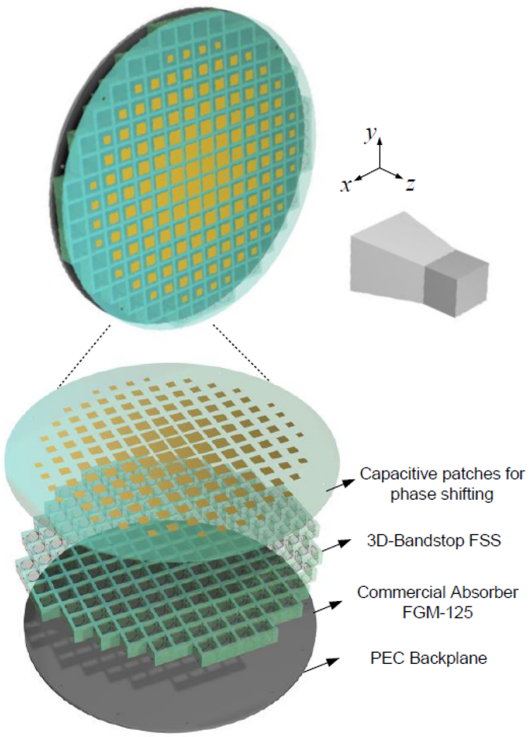


(b)

Figure 2.5: (a) Configuration of absorptive frequency-selective reflection structure element. (b) The prototype of the low-RCS reflectarray [29].

Furthermore, by placing an absorptive material behind the bandstop-FSS-backed reflectarray, the impinging EM waves at the out-of-band frequencies can be absorbed [29], as shown in Fig. 2.5. The FSS-backed reflectarray with absorptive material structure can be seen as a PEC within the operating band, while behaving as an absorber at the out-of-band frequencies.

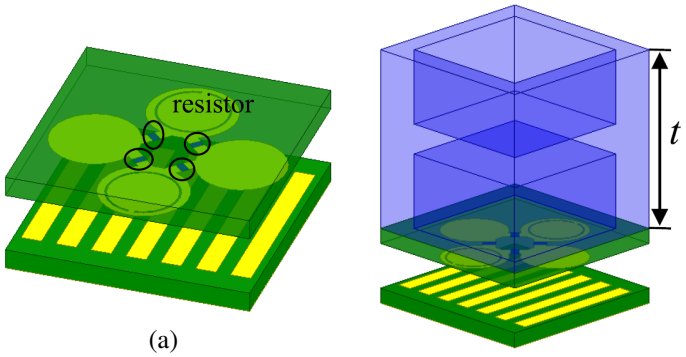


(a) (b)

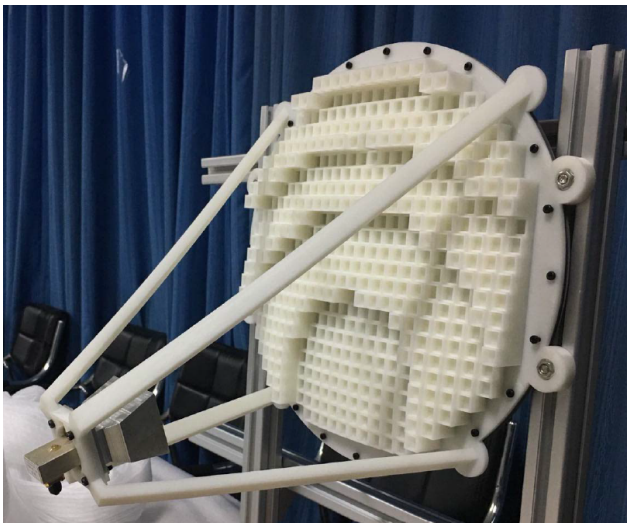

(c)

Figure 2.6: (a) Configuration of the band-notched absorber element. (b) Configuration of the low-RCS transmitarray unit cell. (c) Photograph of the low-RCS reflectarray antenna [30].

The second method is to combine a reflectarray with a frequency selective rasorber (FSR) to achieve RCS reduction [31]. In [31], by placing the FSR structure between the reflectarray and feed horn, the incident waves fed by horn antenna can be transmitted with low loss in the operating band while RCS is significantly reduced at out-of-band

frequencies. The FSR is able to absorb the impinging waves at out-of-band frequencies while maintain the transmission performance, which can be seen as a combination of an antenna radome and an absorber [32–34].

The third method is to employ a band-notched absorber and a dielectric lens [30], as shown in Fig. 2.6. The band-notched absorber can provide an absorption-reflection-absorption frequency response. It can create a reflection band with low losses within a wide absorption band which is achieved by employing resistors instead of absorptive materials to consume the impinging EM waves besides the reflection band. In addition, a dielectric lens is placed on top of the band-notched absorber to achieve the required phase compensation.

## 2.2 Wideband Conformal Transmitarrays

Conformal transmitarrays are developed for various mounting applications, e.g., satellites, aircrafts and UAVs. They can provide high gains with adapting the aerodynamic requirements of the mounting platforms. The conformal transmitarray antennas are also composed of transmission element array and an illuminating feed source similar with the planar transmitarray antennas. A highly-focused beam can be converted from a low-gain spherical beam radiated from the feed source by individually designed the transmission phase of each element on the aperture of the transmitarray.

A conformal transmitarray is designed to adapt the shape of a mounting platform, which can be a part of the platform surface and accommodate a feeding antenna placed behind the transmitarray to utilize platform space better without destroying its aerodynamic performance. Based on the current fabrication technologies, metallic ink can be printed directly on a curved structure. However, it is very expensive and technically difficult for multi-layer metal printing on curved surfaces. Thus, one of the most practical and cost-efficient methods to realize a conformal transmitarray is to employ very thin transmitarray elements with a thickness of less than 0.5 mm and then bend the thin planar transmitarray based on a desired shape.

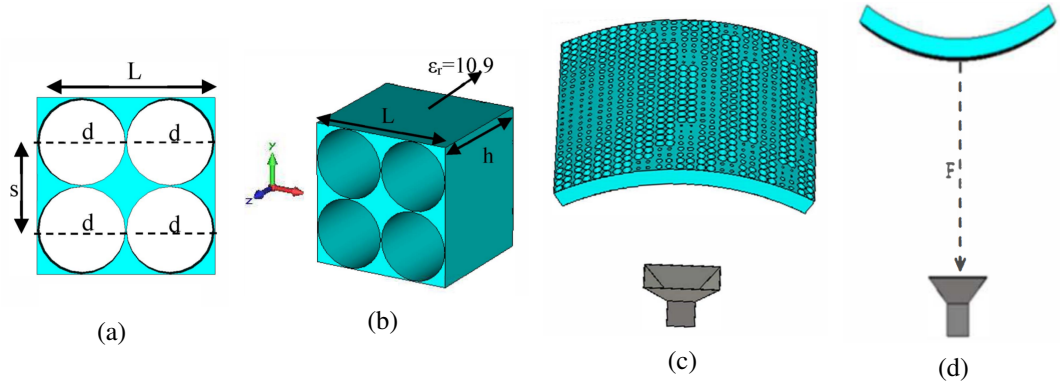


Figure 2.7: (a) Top view and (b) side view of the square perforated element. (c) The geometry of cylindrical perforated concave transmitarray. (d) The geometry of cylindrical perforated convex transmitarray [35].

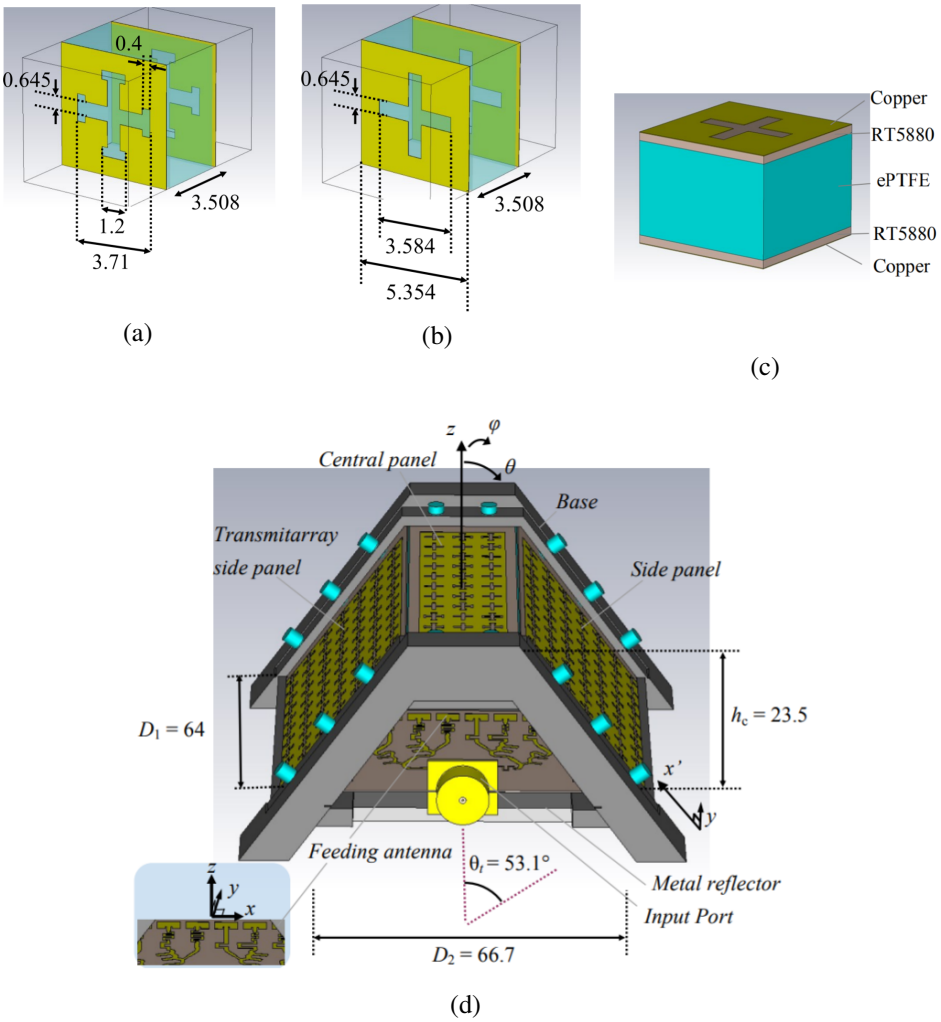


Figure 2.8: (a) OFF state, (b) ON state, (c) layer stackup of the unit cell. (d) Transmitarray structure [36].

Recently, Some reported research efforts have been demonstrated to conformal transmitarrays [35–40]. Concave and convex cylindrically conformal transmitarrays were designed based on cylindrical perforated dielectric sheet [35], as shown in Fig. 2.7. A conformal transmitarray was designed consisting of three planar sub-transmitarrays [36], as shown in Fig. 2.8. A cylindrically conformal transmitarray employing four-layer cascaded elements was designed [40], as shown in Fig. 2.9.

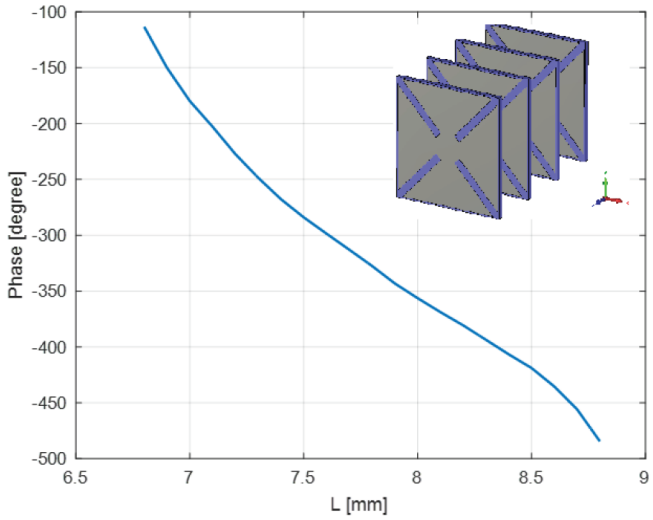


(a)

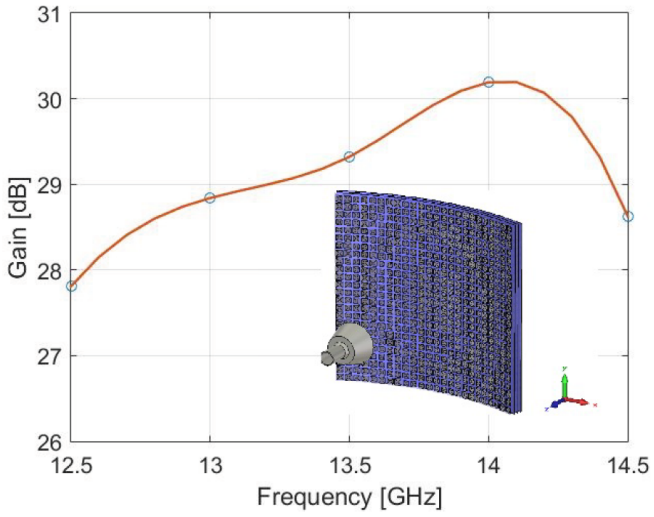


(b)

Figure 2.9: (a) Curved 4-layer transmission element and its transmission phases. (b) Cylindrically conformal transmitarray with a feed horn antenna [40].

However, these conformal transmitarrays above are not implemented. By bending an

ultrathin planar transmitarray based on a desired shape, a cylindrically conformal transmitarray employing ultra-thin triple-layer slot elements was developed with a peak gain of 19.6 dBi, an aperture efficiency of 25.1 % and 3 dB gain bandwidth of 6.7 % [37], as shown in Fig. 2.10.

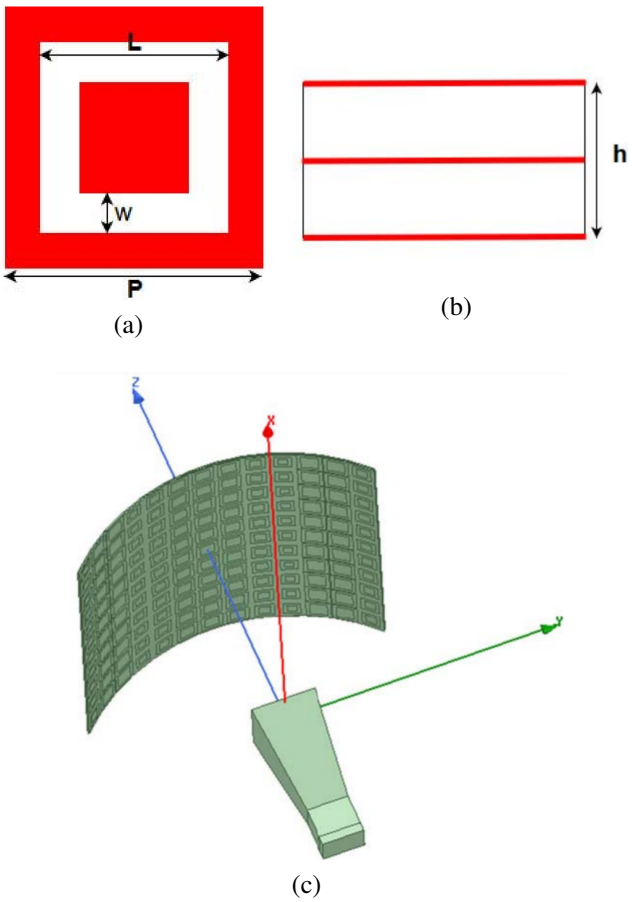


Figure 2.10: (a) Top view and (b) side view of the ultra-thin triple-layer slot element. (c) 3-D view of the cylindrically conformal transmitarray antenna [37].

As shown in Fig. 2.11, a high-efficiency cylindrically conformal transmitarray was developed employing dual-layer ultrathin Huygens elements with a gain of 20.6 dBi, a 47 % aperture efficiency and 3 dB gain bandwidth of 3.7 % (9.83-10.2 GHz) [39]. In [37,39], the bandwidth of the conformal transmitarrays are limited, which are not suitable for many platforms and wireless communication systems. For example, to support hundred gigabits-per-second (Gbps) to terabits-per-second (Tbps) data rates required by the 6G networks, their antennas must provide enough bandwidth.

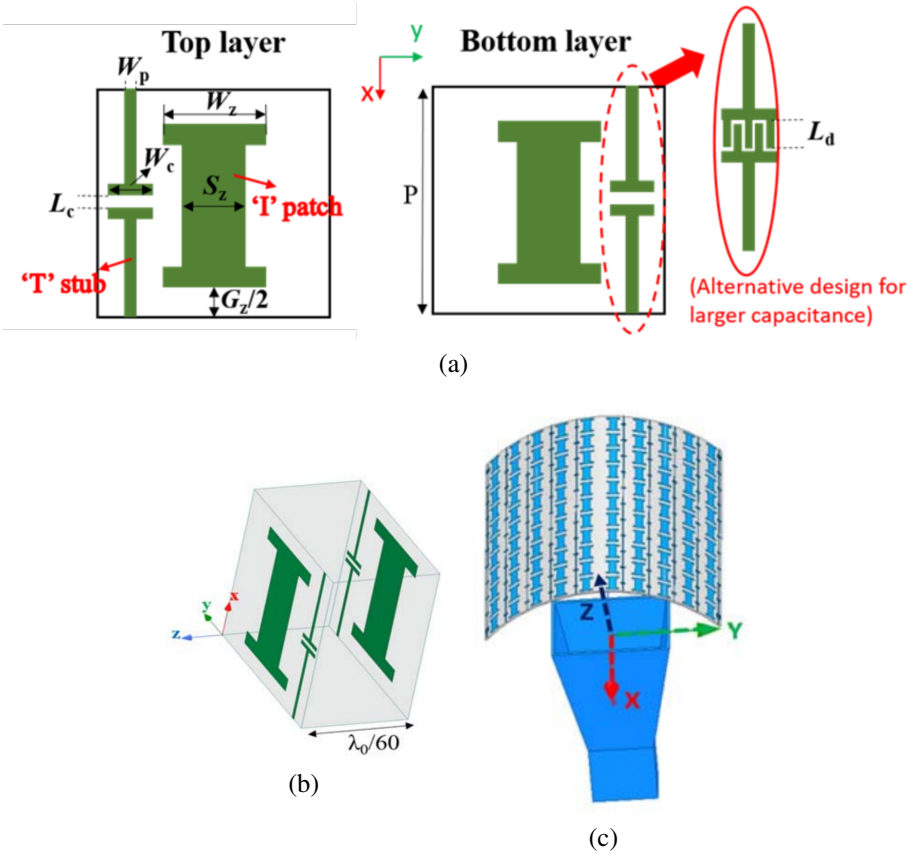


Figure 2.11: (a) Top and bottom layers; (b) 3-D structure of the dual-layer Huygens element. (c) High-efficiency dual-layer conformal transmitarray structure [39].

In [38], an ultrawideband cylindrically conformal transmitarray was proposed employing connected slot-bowtie elements with true-time delay lines achieving a realized gain of from 12.0 dBi to 20.2 dBi and an aperture efficiency of from 39 % to 76 % in the operating band from 8.5 GHz to 17 GHz, as shown in Fig. 2.12. However, the slot-bowtie and true-time delay line of an element of the ultrawideband transmitarray are vertically connected by soldering, which may result in manufacture difficulties, alignment errors especially at higher frequencies and degraded aerodynamic performance.

According to the above literature review, it can be found that it is highly desired to develop wideband conformal dual-layer transmitarray to support high data rate and aerodynamic requirements with reduced alignment errors. It should be noted that there are some reported planar dual-layer transmitarrays using malta-cross elements with metallic vias [41] shown in Fig. 2.13 (a) or patch elements with metallic vias [42].

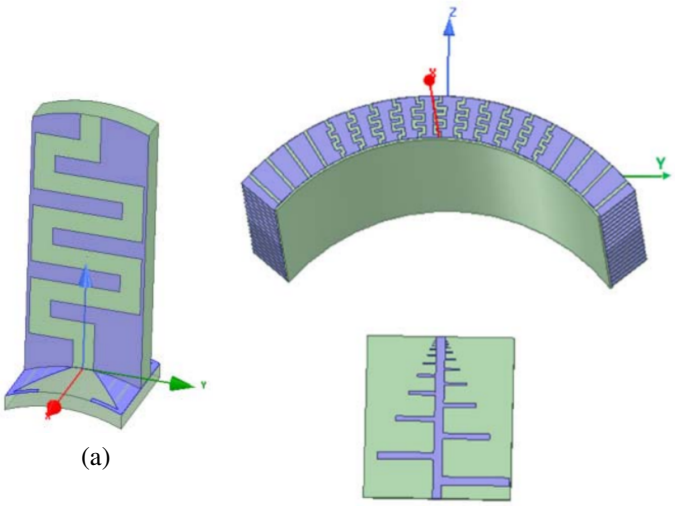

(a)

(b)

Figure 2.12: (a) Curve wideband element. (b) Cylindrically conformal transmitarray with a log-periodic dipole feed antenna [38].

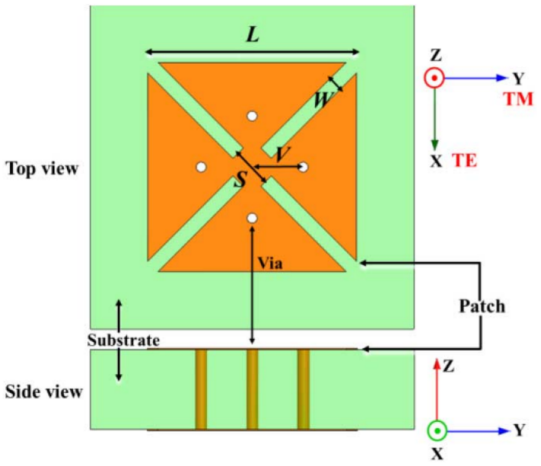


(a)

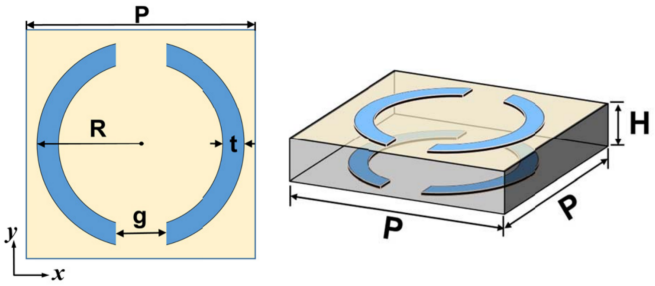


(b)

Figure 2.13: The configurations of (a) the dual-layer malta-cross element with metallic vias [41] and (b) the dual-layer CP element without metallic vias [43].

However, the metallic vias increase the transmitarray complexity and make the aperture surface fragile and difficult to bend. Without inserting metallic vias, planar dual-layer transmitarray elements can achieve full phase range by rotating the elements for circular polarization, but this approach is not suitable for linear polarization because of the polarization mismatch with the elements rotated [43], as shown in Fig. 2.13 (b).

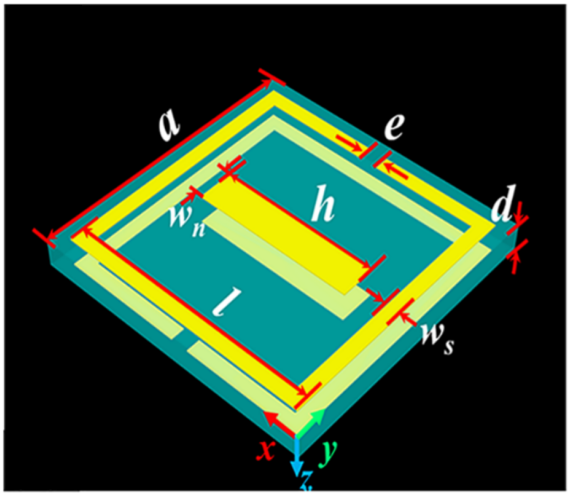


Figure 2.14: The configuration of a dual-layer Huygens element [44].

Furthermore, some planar dual-layer transmitarrays without metallic vias are to employ dual-layer Huygens elements [44–47]. An antisymmetric dual-layer Huygens element [44] is shown in Fig. 2.14. The Huygens elements can provide a nearly total transmission and full phase coverage when the electric and magnetic responses are balanced, which is beneficial to design high-efficiency transmitarrays. However, most of their bandwidths are very limited. Only the transmitarray in [47] can provide the 3-dB bandwidth of 15.7 % but are not suitable for conformal applications.

There have been many reported efforts to enhance the bandwidth of planar transmitarrays. In [48], a triple-layer FSS element printed on three dielectric substrates separated by two air spacers is proposed for a wideband transmitarray with 1-dB gain bandwidth of 16.8 % as shown in Fig. 2.15 (a). In [49], a wideband transmitarray with 1-dB gain bandwidth of 16 % is developed employing two identical triple-layer FSSs separated by an air spacer as shown in Fig. 2.15 (b). Actually, there is always a tradeoff between the thickness of the transmitarray and its gain bandwidth. Thus, it is very challenging to

improve the bandwidth of a dual-layer transmitarray for conformal applications.

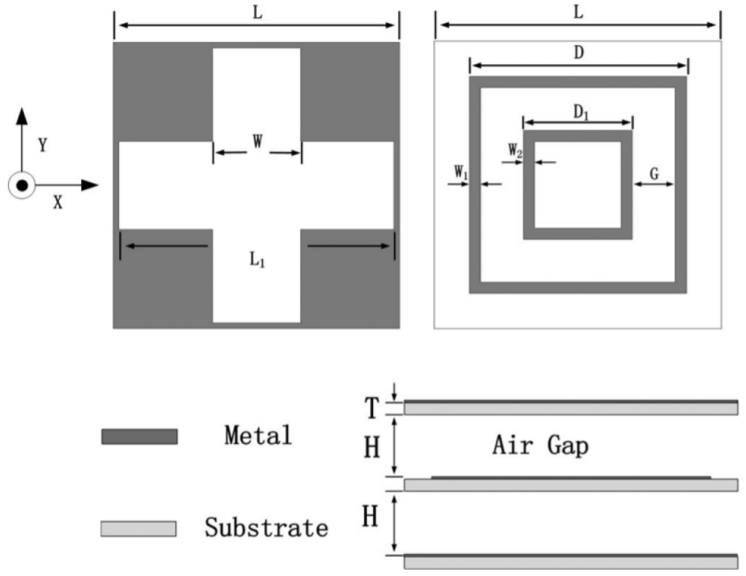


(a)

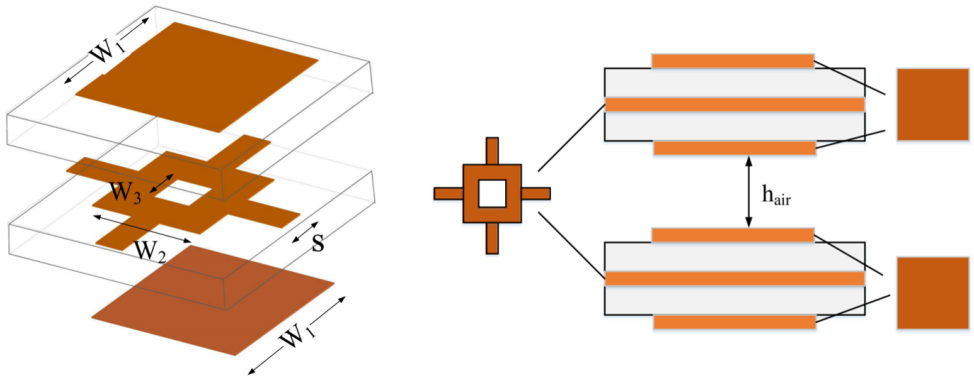


(b)

Figure 2.15: The configurations of (a) a triple-layer transmitarray element [48] and (b) a six-layer transmitarray element [49].

## 2.3 Reconfigurable Transmitarrays for Beam Scanning

Electronic beam scanning transmitarrays have attracted substantial attention due to their wide applications in satellite communications, imaging systems and automotive radars. Compared to phased arrays using transmission line based feeding networks, re-

configurable transmitarrays [10, 13, 50–62] have spatial feeding architecture, which can achieve excellent 2-D beam steering and/or shaped beam with less cost and loss, especially at millimeter-wave or higher bands. The beam scanning is realized by independently controlling the reflection or transmission phases of the elements on the apertures using PIN diodes, MEMS switches or varactor diodes.

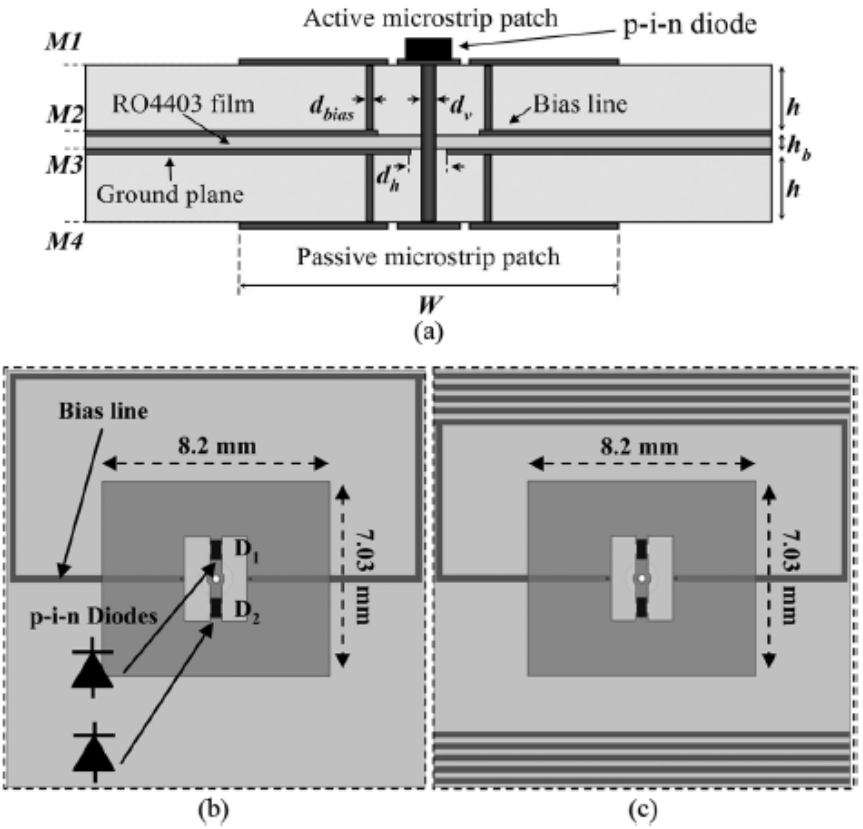


Figure 2.16: 1-bit electronically reconfigurable element [14]. (a) Side view. Top view of an element with (b) 1 biasing line, or (c) 10 biasing lines.

In the last two decades, many electronically beam scanning transmitarrays have been reported. A typical method is to use reconfigurable receiver-transmitter (Rx-Tx) elements [**?**, **?**, 50–59]. These elements usually consist of three parts: a receive (Rx) unit, an electronically controlled phase shifter, and a transmit (Tx) unit. In a Rx-Tx element, metallic vias are usually placed to transmit EM waves between the Rx and Tx units. Moreover, additional substrate layers are needed for direct current (DC) biasing networks to control the phase shifters. As a result, the configuration of a reconfigurable Rx-Tx

element usually contains more than three metallic layers with multiple metallic vias. For example, in [52], [55], and [57], the reconfigurable elements have 4 layers with 18 vias, 6 layers with 7 vias, and 5 layers with 6 vias, respectively.

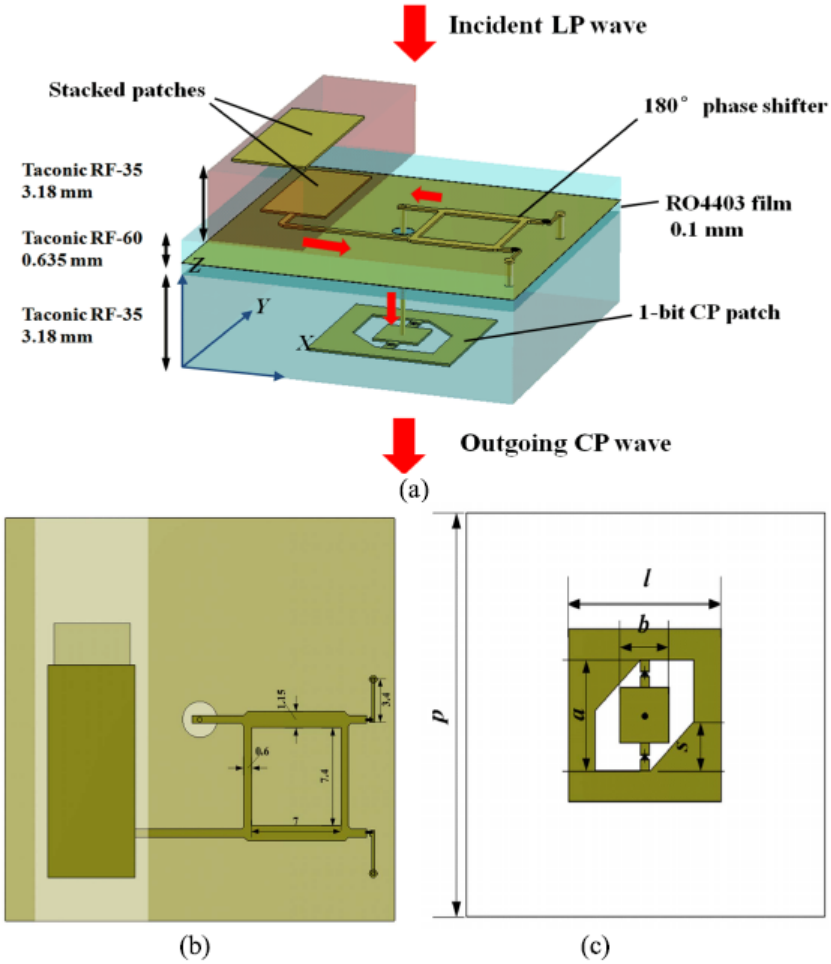


Figure 2.17: (a) CP transmitarray element architecture [57]. (b) Receiver unit. (c) Transmitter unit.

As shown in Fig. 2.16, the element stack-up consists of four metal layers: receiver unit, biasing lines, ground plane and transmitter unit [14]. Two PIN diodes are integrated on the receiver unit of each element to control its transmission phase. Finally, a 15.8 % fractional bandwidth and a maximum gain of 22.7 dBi at broadside were achieved. Also as depicted in Fig. 2.17, using receiver-transmitter approach with integrating two PIN diodes on transmitter patch, a linearly polarized (LP) incidence wave was transformed into a circularly polarized (CP) outgoing wave, and beam steering at angle of $\pm 45^{\circ}$ was

achieved [57]. As shown in Fig. 2.18, receiver-transmitter approach is still used for reconfigurable realization, and varactor diodes are integrated in the middle phase shifters [13].

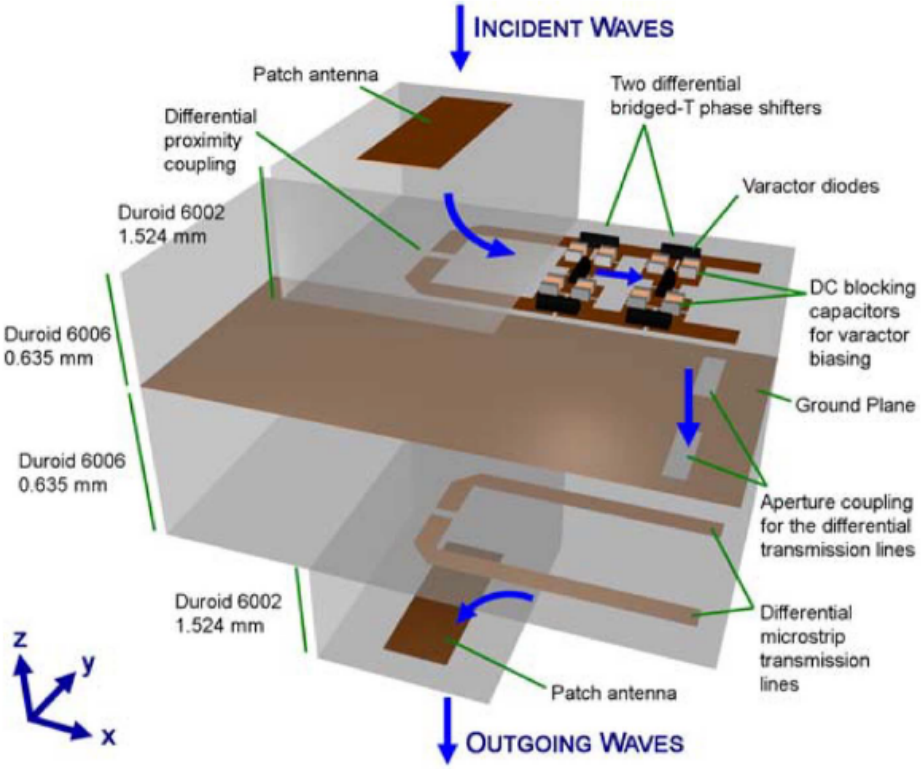


Figure 2.18: Reconfigurable element design [13].

Another method to achieve beam scanning transmitarrays is to employ FSS based reconfigurable elements. These elements utilize mutual coupling between multiple layers to transmit electromagnetic waves through the aperture surfaces without metallic vias. In [60], a reconfigurable transmitarray element consisting of four layers printed on two substrates can achieve 1-bit phase shift by controlling two PIN diodes integrated in the element as shown in Fig. 2.19 (a). In [61], a five-layer cascaded FSS element can achieve 360° continuous phase coverage with three varactor diodes on each layer as shown in Fig. 2.19 (b). In [62], a five stacked layers of square-slot FSS element loaded with two varactor diodes on each layer is proposed to achieve 440° phase range at fixed frequency as shown in Fig. 2.19 (c). The phase compensation provided by these elements is achieved by varying their resonant frequencies.

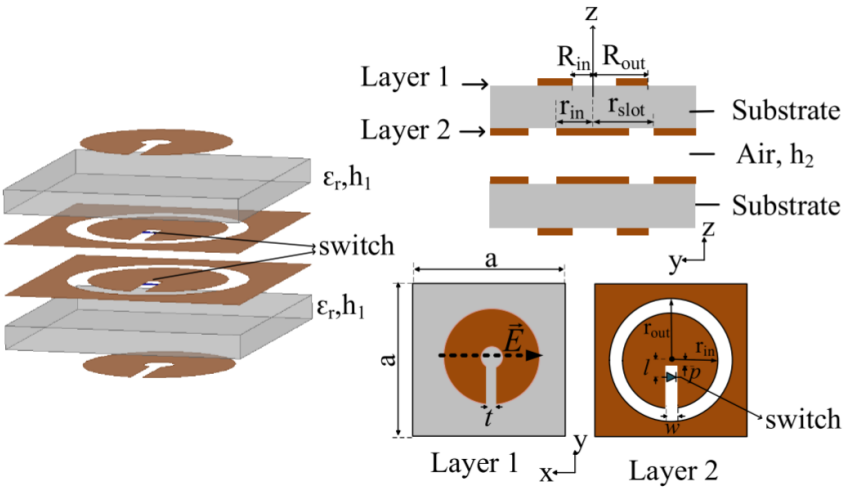


(a)

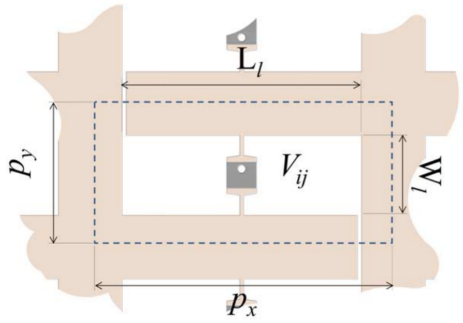


(b)

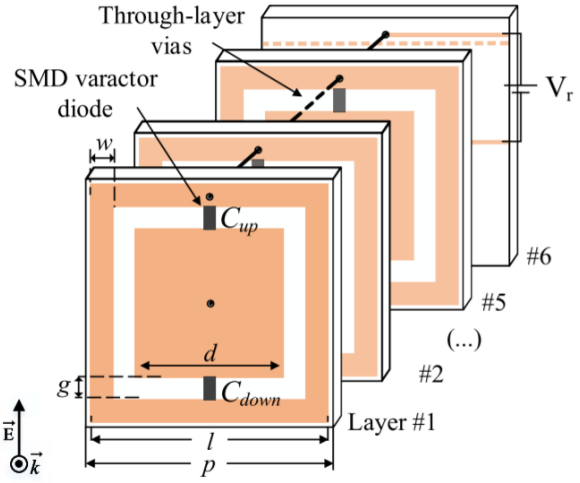


(c)

Figure 2.19: (a) A 4-layer reconfigurable element integrated with two PIN diodes [60]. (b) A 5-layer FSS element integrated with 3 varactor diodes on each layer [61]. (c) A five stacked layers of square-slot FSS element integrated with 2 varactor diodes on each layer [62].

According to the above literature review, it can be found that most of the currently reported reconfigurable transmitarray elements have more than three metallic layers with several metallic vias. Such configurations may lead to complex fabrication and package processes, which could affect the performance of transmitarrays. For example, for a 2-bit reconfigurable transmitarray using 6-layer elements with 7 vias at 29 GHz reported in [55], 51 elements were found faulty, which could be due to the fabrication inaccuracies. Hence, it is highly desirable to design dual-layer reconfigurable transmitarray elements without metallic vias, which can also facilitate the design of large-size arrays at higher frequencies. Actually, electronic beam-scanning transmitarrays based on dual-layer reconfigurable elements have been rarely reported.

# 3

# Low RCS Transmitarray

## 3.1 Introduction

High-gain antennas are essential to achieving long-distance communications in space and terrestrial systems. In order to obtain high gains, a large antenna aperture is required, but this increases the scattering area as well, which would normally lead to high RCS unfortunately. Consequently, it is a major challenge to design an antenna with both high-gain and low-RCS properties. Since reflectarrays and transmitarrays can achieve high gains without using complex and lossy feed networks, they have been widely hailed as competitive high gain antenna candidates. Compared to reflectarrays, transmitarrays do not have the issue of feed blockage [1–3].

To this end, there have been substantial advances in various types of transmitarrays, e.g., wideband transmitarrays [49, 63, 64] and beam steering transmitarrays [50, 65, 66]. To author's best knowledge, there has been no reported method for reducing the RCS of transmitarrays without affecting their radiation performance. In order to fill this technology gap, a phase controllable AFST element is developed and applied to a low-RCS transmitarray in this work. The AFST structure [67], also known as frequency-selective rasorber [32], absorptive/transmissive FSS [68] or bandpass frequency-selective absorber [69], has the property of absorption-transmission-absorption for the scattering parameters. It should be noted that the currently reported AFST elements have the same transmission phases, focusing on periodic surface designs. However, for transmitarray designs, the elements need to provide a digital or continuous phase change to achieve collimated or shaped beams. Actually, it is very challenging to manipulate the phase response of the AFST elements as the phase response is usually related to the element's absorption and transmission performance.

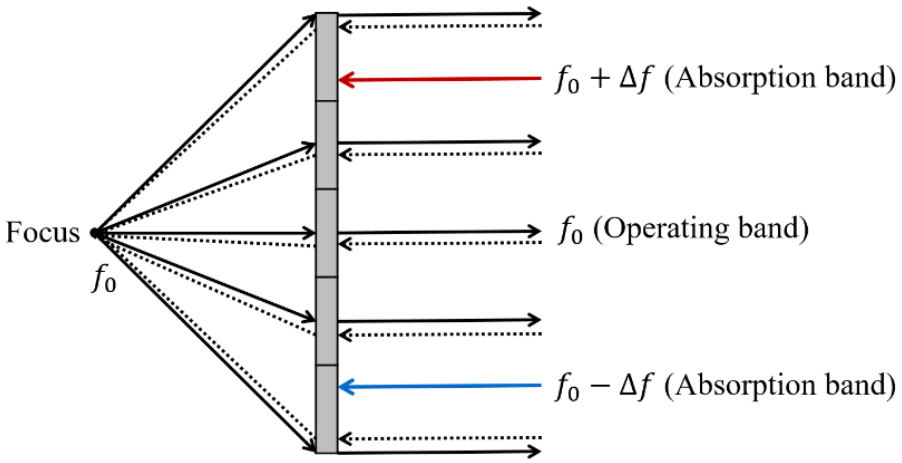


Figure 3.1: Conceptual depiction of a low RCS transmitarray.

In this chapter, a low RCS transmitarray is presented using phase controllable AFST elements. The element consists of asymmetrical resonators with resistors to obtain an absorption-transmission-absorption response. The transmission phase within the transmission band can be controlled by rotating the AFST elements, achieving a 1-bit phase change. A low-RCS transmitarray using the developed elements is designed, fabricated

and measured. Compared with a reference transmitarray, the radiation performance of the low-RCS one is almost unchanged with a realized gain of 24.4 dBi. Significant RCS reductions have been realized for dual polarizations of the impinging EM waves. The 10 dB RCS reduction bandwidths are 18 % and 14 % for the lower and upper absorption bands, respectively.

The design concept schematic of the proposed low RCS transmitarray is shown in Fig. 3.1. For an incident EM wave of frequency $f_0$, it behaves transparent with total transmission. Moreover, the transmitted waves can be transformed from a spherical EM waves to a plane EM waves by using a specific transmission phase distribution. For the lower frequency band $f_0$-$\Delta f$ and the upper frequency band $f_0$+$\Delta f$, it acts as an absorber with good absorption performance.

## 3.2 Phase Controllable AFST Element

### 3.2.1 AFST Element

To create a transmission band within a wide absorption band, the key idea is to make the absorptive layer become transparent to EM waves in transmission band by utilizing a dual circular ring on the top layer and a circular slot on the bottom layer, which are both equivalent to parallel LC resonators for the incident wave vertical to the substrate [31].

The configuration of the proposed AFST element is illustrated in Fig. 3.2. It consists of two dielectric substrates separated by an air spacer. Top and bottom metallic layers are printed on top and bottom substrate layers, respectively. It is seen from Fig. 3.2 (a) that the top layer is a dual circular ring connected by four metallic strips. Resistors are embedded on the metallic striplines to achieve the absorption performance at certain frequencies. As shown in Fig. 3.2 (b), the bottom layer is a bandpass FSS consisting of a circular slot. The structure of the resultant AFST structure after integration is shown in Fig. 3.2 (c). The parameter values are as follows: $R_{in}$ = 2.19 mm, $R_{out}$ = 2.69 mm, $r$ =

3.24 mm, $w_1$ = 0.31 mm, $w_2$ = 0.3 mm, $l$ = 3 mm, $D$ = 12 mm, $H$ = 5.5 mm, $h$ = 0.5 mm, the lumped resistors are 200 Ω.

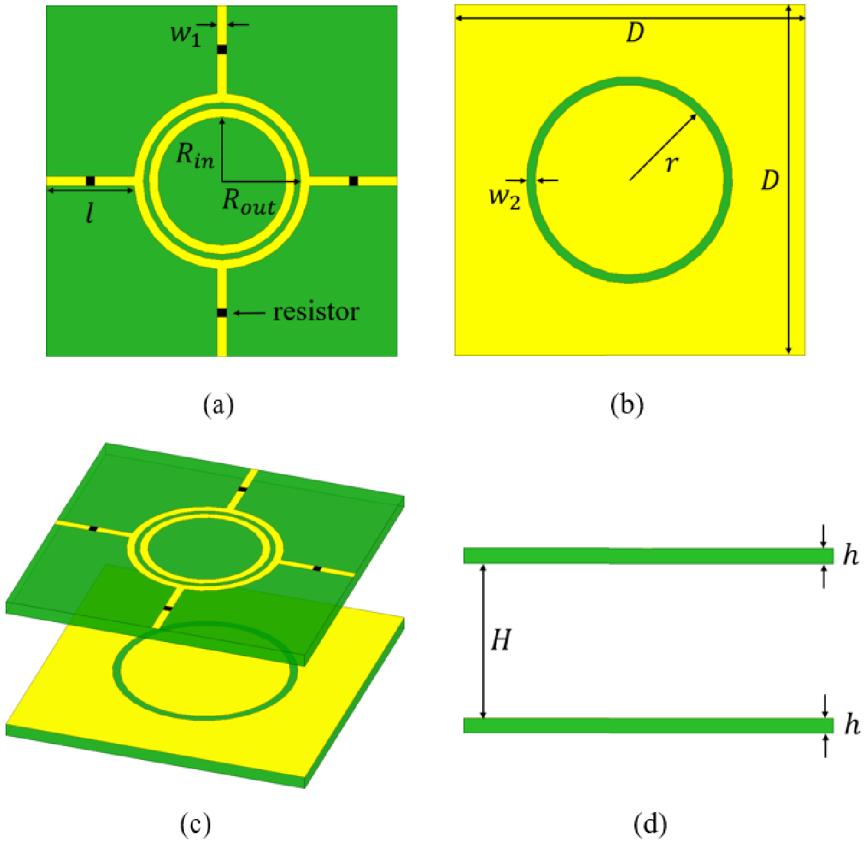


Figure 3.2: Configuration of the AFST element. Top view of (a) top layer and (b) bottom layer. (c) 3D view and (d) side view of the AFST element.

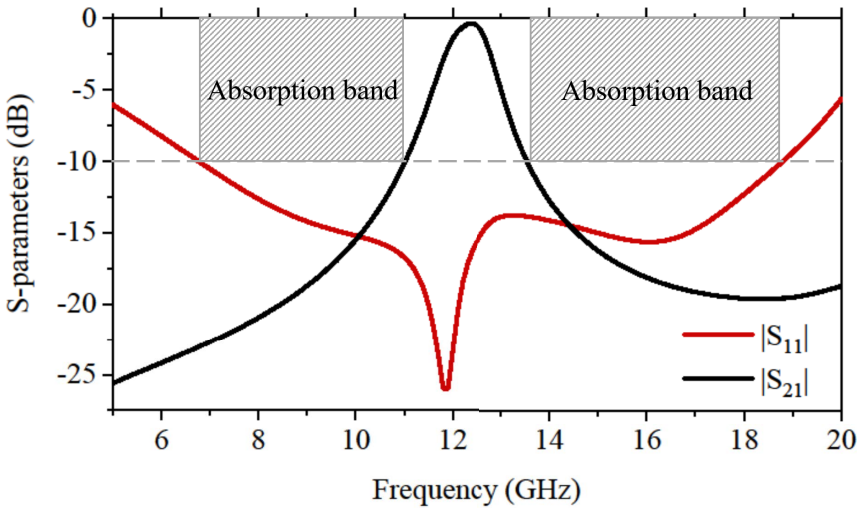


Figure 3.3: Transmission and reflection magnitudes of the AFST unit cell.

The AFST element is analyzed in a periodic boundary condition by EM simulation software HFSS. As shown in Fig. 3.3, the AFST element can provide a transmission band with less than 1 dB transmission loss from 12.1 GHz to 12.6 GHz and two wide absorption bands besides the transmission band. The lower absorption band has the reflection and transmission losses of larger than 10 dB from 6.8 GHz to 11.0 GHz, corresponding to a fractional absorption bandwidth of 47 %. The upper absorption band has the reflection and transmission losses of larger than 10 dB from 13.5 GHz to 18.8 GHz, corresponding to a fractional absorption bandwidth of 33 %.

### 3.2.2 Phase Controllable AFST Element Using Asymmetric Configuration

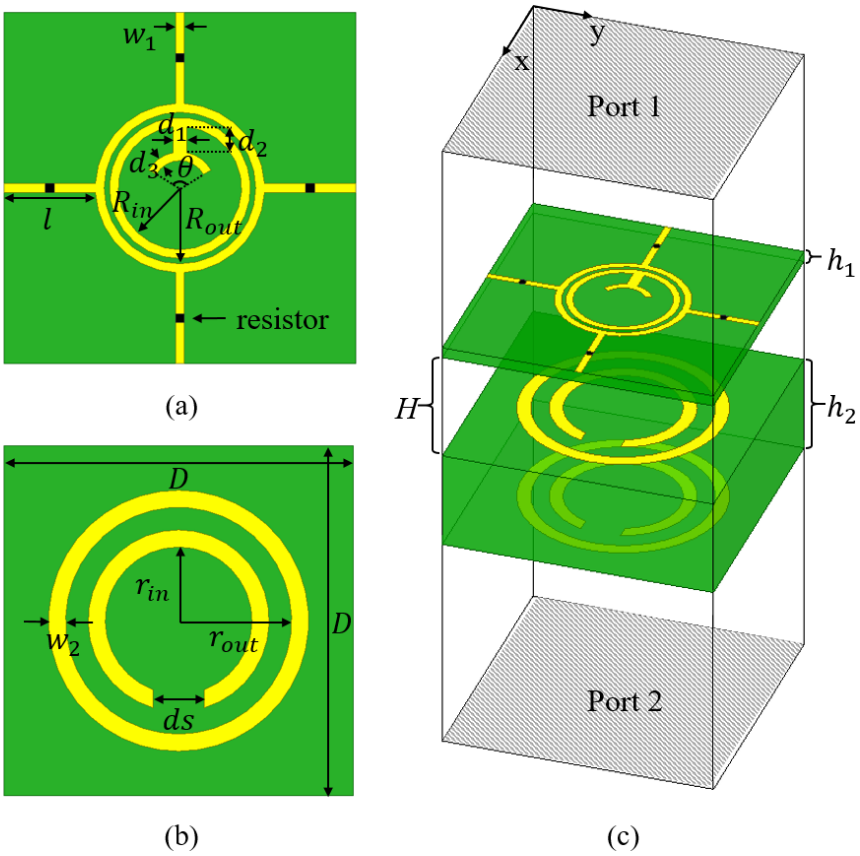


Figure 3.4: Configuration of the phase controllable AFST element. (a) Top side of the first substrate. (b) Top or bottom side of the second substrate. (c) HFSS model of the phase controllable AFST element.

In order to control the transmission phase within the transmission band, phase controllable AFST unit cell is proposed based on the AFST structure in 3.2.1. The configuration of the proposed phase controllable AFST element is shown in Fig. 3.4. It consists of two substrates, which are separated by air. It is seen from Fig. 3.4 (a) that the top side of the first substrate has a dual circular ring connected by four metallic strips. Resistors are soldered between these metallic strips. An arched strip is printed on the inner circular ring. This metallic layer is named as Layer 1. The metal on the bottom side of this substrate has been removed. The top and bottom sides of the second substrate are the same.

Each side is composed of an outer metallic circular ring and an inner metallic split circular ring as shown in Fig. 3.4 (b). These two metallic layers are named as Layers 2 and 3, respectively. These two identical layers are used to achieve a sufficient phase change range and a high transmission coefficient which will be shown in 3.2.4. The first and the second substrates are Rogers RO4350 substrate (relative permittivity of 3.66 and loss tangent of 0.004) and Arlon AD270 substrate (relative permittivity of 2.7 and loss tangent of 0.0023), respectively.

### 3.2.3 Equivalent Circuit Model of Phase Controllable AFST Element

To illustrate the mechanism of the phase controllable AFST element, its equivalent circuit model is shown in Fig. 3.5. It should be mentioned that $Z_1$, $Z_2$ and $Z_0$ are the characteristic impedances of the first substrate, the second substrate and the free space, respectively. $\theta_1$, $\theta_2$, and $\theta_0$ are the electrical lengths corresponding to the thicknesses of the first substrate, the second substrate and the free space, respectively.

The outer circular ring and the inner ring with an arched metallic strip on Layer 1 are modeled as a parallel $LC$ circuit consisting of $L_4$ and a series $L_1C_1$. The four metallic strips embedded with four lumped resistors are equivalent to $L_5R$ series circuits. On Layer 2 or 3, the outer circular ring and the inner ring with a split are modeled as series connections of $L_2C_2$ and $L_3C_3$, respectively. The two series circuits are paralleled with each other. They perform as a bandpass FSS. In order to achieve a minimum insertion

loss, the parallel $LC$ circuits on Layers 1, 2 and 3 should be designed to have an overlapped passband. In the two bands at two sides of the passband, Layer 1 has two series $LC$ frequencies, and Layer 2 or 3 (bandpass FSS) performs as a ground plane for Layer 1 to absorb the incidence waves. Thus, two absorption bands are achieved with very low transmission and reflection coefficients. For the developed structure, the resistors will not affect the transmission efficiency in the transmission band while only providing absorption at the bands beside the transmission band.

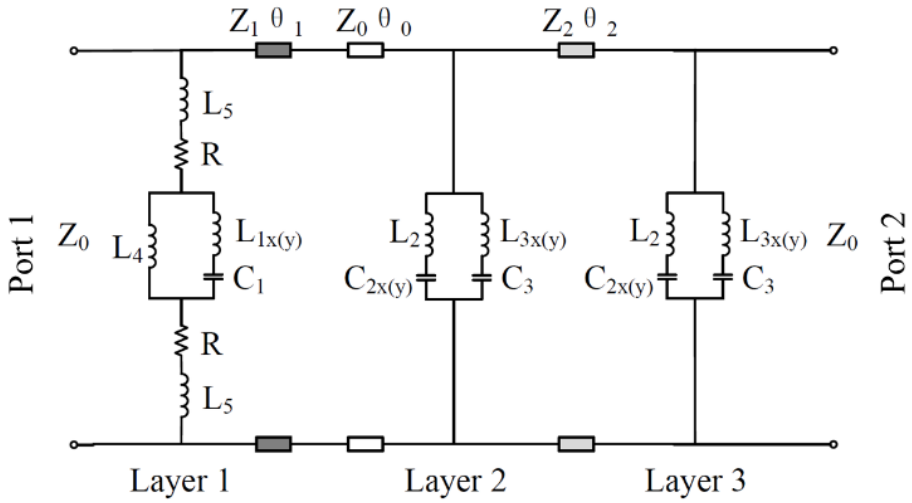


Figure 3.5: Equivalent circuit of the phase controllable AFST element.

Simulated transmission and reflection coefficients of the equivalent circuit can be obtained from the circuit simulation software ADS. In this work, we aim to achieve a passband at 12.5 GHz and two absorption bands at the two sides of the passband. Please be noted that although the equivalent circuits for x- and y-polarized waves have the same topology, some of the elements have different values to account for the structure asymmetry.

To this end, the values of equivalent inductances, capacitances and resistances are optimized as follows: $Z_0$ = 377 Ω, $Z_1$ = 197 Ω, $Z_2$ = 229 Ω, $\theta_0$ = 75° at 12.5 GHz, $\theta_1$ = 7.5° at 12.5 GHz, $\theta_2$ = 67.5° at 12.5 GHz, $R$ = 200 Ω, $L_{1x}$ = 1.18 nH for x-polarization, $L_{1y}$ = 1.07 nH for y-polarization, $L_2$ = 3.36 nH, $L_{3x}$ = 3.56 nH for x-polarization, $L_{3y}$ = 2.57 nH for y-polarization, $L_4$ = 0.82 nH, $L_5$ = 1.13 nH, $C_1$ = 0.065 pF, $C_{2x}$ = 0.114 pF for x-polarization, $C_{2y}$ = 0.078 pF for y-polarization, $C_3$ = 0.036 pF. The simulated

scattering parameters are shown in Fig. 3.6. These results will be compared with the EM simulations and discussed in 3.2.4.

### 3.2.4 Implementation of the Phase Controllable AFST Element

Based on the circuit analysis of the phase controllable AFST element, its 3D model is analyzed in a periodic boundary condition by EM simulation software HFSS with either an x- or y-polarized incidence wave. The reason to simulate the element under two polarizations is to calculate the performance of the element and its 90° rotated counterpart.

As shown in Fig. 3.4, it can be observed that the resonant length for the incidence wave of x and y polarizations are different for this element due to the arched metallic strip on Layer 1 and splits on the inner circular rings on Layers 2 and 3. The additional arched metallic strip on Layer 1 has an effect on the x-polarized incidence wave, increasing its electrical length. The splits on the inner rings of Layers 2 and 3 reduce the electrical length for the y-polarized incidence wave. The combined effects make the electrical length for y-polarized incidence wave shorter than that for the x-polarized one. Therefore, the y-polarized incidence wave has a higher resonant frequency. According to the design specifications, the dimensions of the element are optimized as follows: $R_{in}$ = 2.15 mm, $R_{out}$ = 2.65 mm, $r_{in}$ = 2.58 mm, $r_{out}$ = 3.97 mm, $w_1$ = 0.31 mm, $w_2$ = 0.6 mm, $l$ = 3.18 mm, $\theta$ = 120°, $d_1$ = 0.5 mm, $d_2$ = 0.95 mm, $d_3$ = 0.2mm, $d_s$ = 1.79 mm, $D$ = 12.26 mm, $H$ = 5 mm, $h_1$ = 0.5 mm, $h_2$ = 4.5 mm, the lumped resistors are 200 Ω.

The EM simulated results are compared with the circuit results. Port 2 corresponds to the position of the feed source of the transmitarray discussed later and Port 1 corresponds to the position of the radar. As this 2-port network is reciprocal, $S_{12}$ is equal to $S_{21}$, so only $S_{21}$ is given in Figs. 3.6 (a) and 3.6 (b). As found in Fig. 3.6 (a), the element resonates at two adjacent frequency points for the illumination waves of two polarizations, respectively. There is an overlapped passband from 12.35 GHz to 12.60 GHz with an insertion loss less than 3 dB. During this passband, the transmission phase difference between the two polarizations is about 180° as shown in Fig. 3.6 (b). Therefore, for

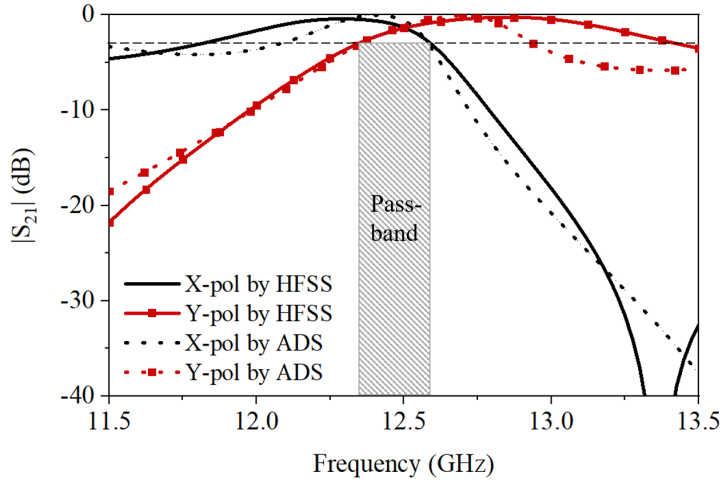


(a)

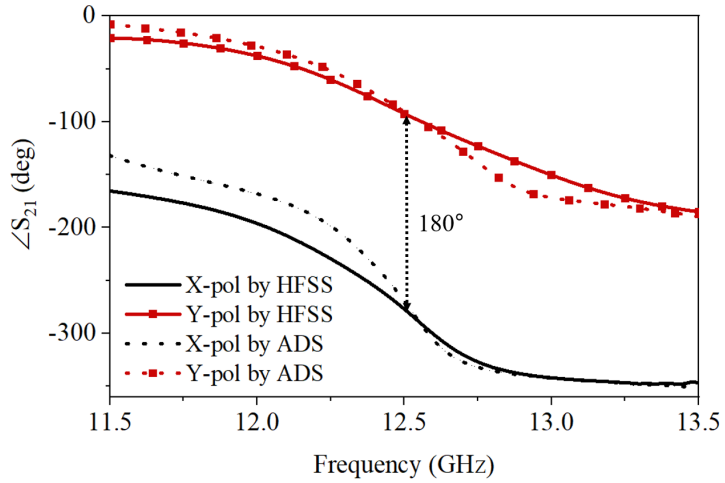


(b)

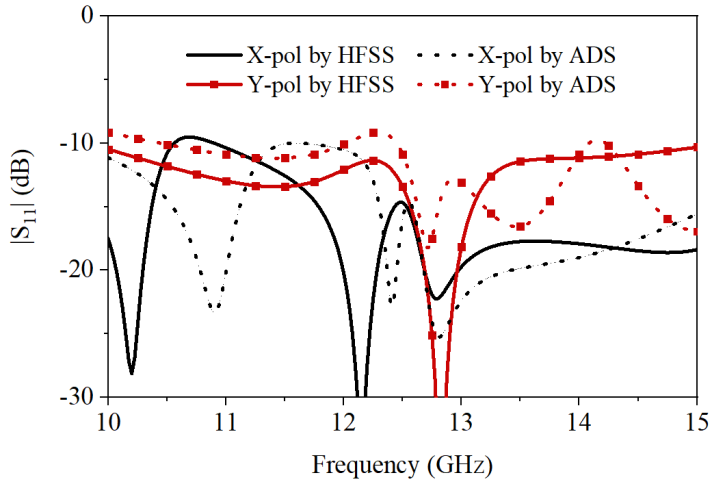


(c)

Figure 3.6: Simulated results of the phase controllable AFST element. (a) Simulated transmission magnitudes. (b) Simulated transmission phases. (c) Simulated reflection magnitudes.

an incidence wave with a given polarization (either x or y), a 1-bit phase change can be achieved by rotating the element by 90°.

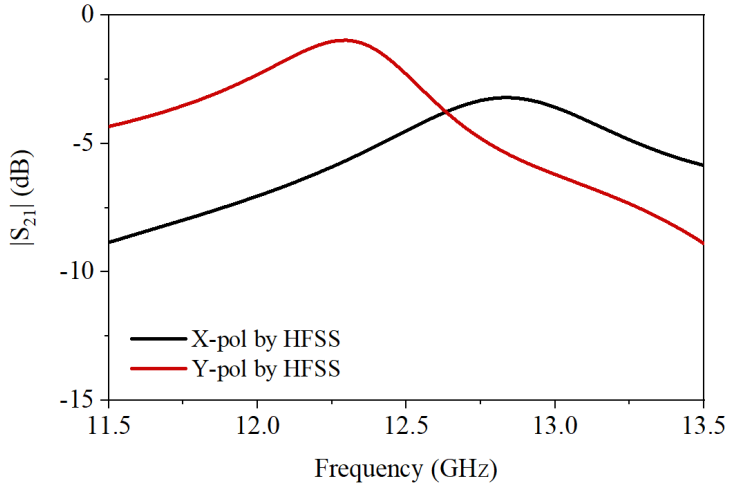


(a)

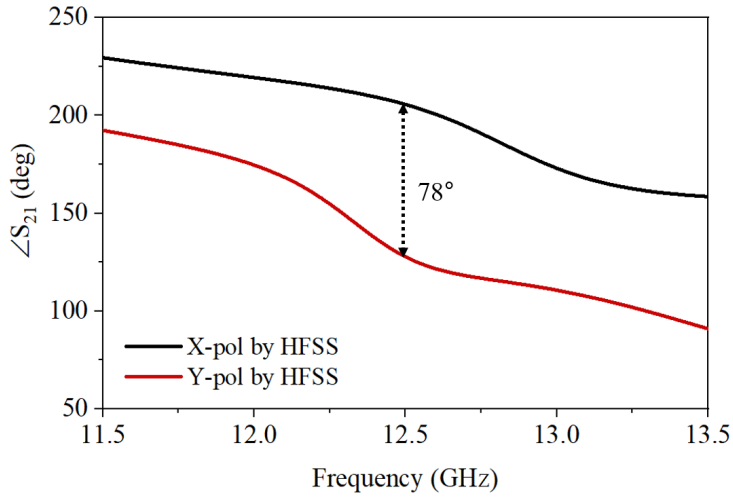


(b)

Figure 3.7: Simulated transmission coefficients of the phase controllable AFST element with Layer 3 removed. (a) Magnitudes. (b) Phases.

These two identical layers Layer 2 and Layer 3 are utilized to achieve enough phase shift between x and y polarizations while maintaining high transmission in the operating band. If Layer 3 is removed from the phase controllable AFST element, its simulated results are shown below in Fig. 3.7. The transmission magnitudes are reduced from -1.6 dB to -4.5 dB at 12.5 GHz for both polarizations. Furthermore, the transmission phase difference between x and y polarizations is reduced from 180° to 78°.

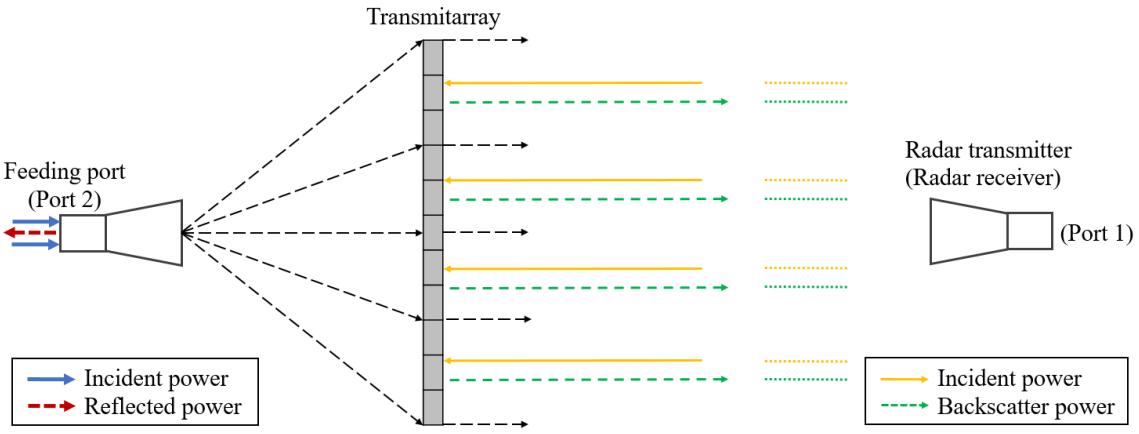


Figure 3.8: The schematic of the Low RCS transmitarray antenna.

To realize RCS reduction of the transmitarray, the input reflection coefficients of the elements under both x and y polarized waves need to be lower than -10 dB within the absorption bands. As shown in Fig. 3.8, the RCS is the ratio of backscatter power density reflected by the transmitarray in the direction of the radar to the power density intercepted by the transmitarray. The RCS is related to the reflection coefficients of the transmitarray unit cell looking from Port 1 side, which are given in Fig. 3.6 (c) and Fig. 3.9.

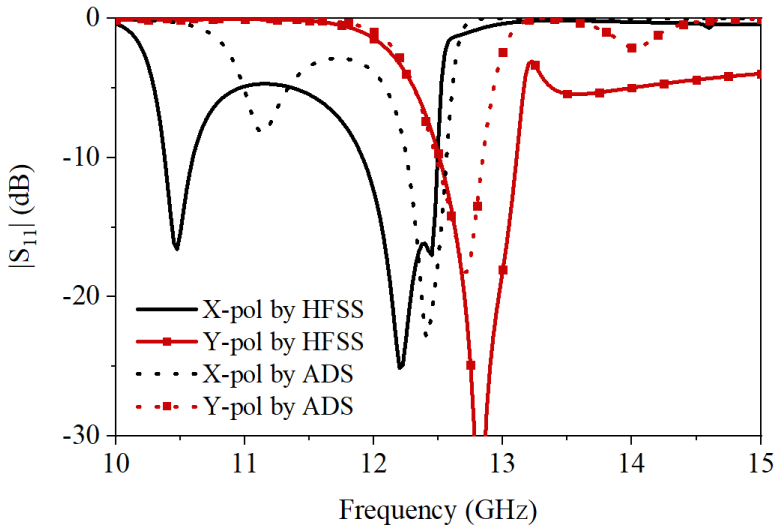


Figure 3.9: Simulated reflection magnitudes of the phase controllable AFST element without resistors.

As seen from Fig. 3.6 (c), the input reflection coefficients for the waves radiated

from Port 1 (radar's position) are lower than -10 dB from 10 GHz to 15 GHz for x and y polarizations. Therefore, a very small amount of the EM waves impinging on the aperture is reflected. As a comparison, the element with resistors replaced by short striplines is also simulated using HFSS, which has similar transmission performance as the AFST elements in the transmission band. However, only at a single frequency point of 12.5 GHz as shown in Fig. 3.9, the overlapped input reflection coefficient for the impinging waves of two polarizations from Port 1 is lower than -10 dB. At other frequency points, high reflections for either or both polarizations are observed, which can result in high RCS.

## 3.3 Low RCS Transmitarray Antenna

### 3.3.1 Low RCS Transmitarray Prototype Design and Implementation

A low-RCS transmitarray prototype is designed at 12.5 GHz using the developed phase controllable AFST elements as shown in Fig. 3.10. Another prototype using the elements with resistors replaced by short striplines is also developed as a reference transmitarray for comparisons. It should be noted that the elements without resistors will no longer possess the absorptive properties outside of the transmission band. However, it can still achieve the 1-bit phase change in the transmission band. Therefore, it can be used as a reference for the RCS comparison. Similar comparison method is used in [30], where a reference reflectarray is set up by using a metallic plane to replace a band-notched absorber.

The low-RCS transmitarray and reference transmitarray have the same aperture size of 245 mm $\times$ 245 mm ($10\lambda \times 10\lambda$), which consists of 400 square-patch elements. A linearly polarized standard gain horn with a gain of 13.5 dB at 12.5 GHz is chosen as the feed antenna for both transmitarrays. The distance between the feeding horn and

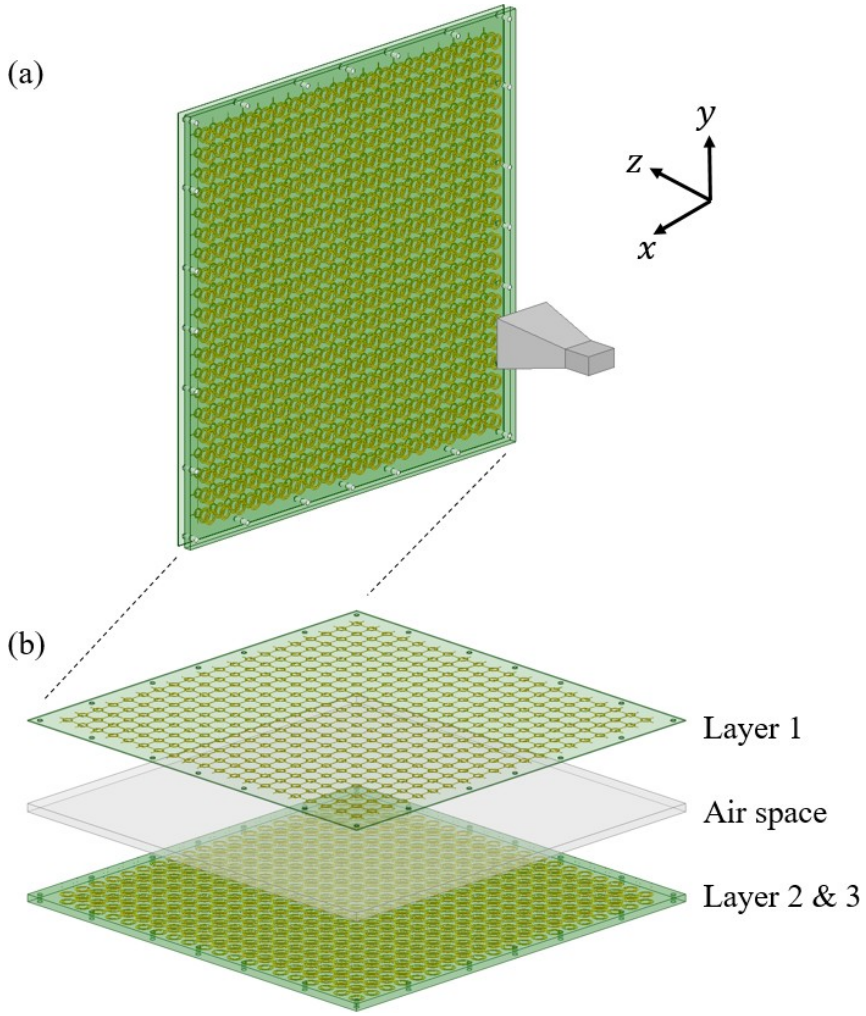


Figure 3.10: The prototype of the proposed low-RCS transmitarray. (a) Schematic of low-RCS transmitarray with a feed horn antenna. (b) Exploded view of the proposed low-RCS transmitarray.

the transmitting surface is 138mm to ensure a 10 dB illumination amplitude taper from the center to the edge of transmitarray aperture. The required transmission phase for each element of both transmitarrays for a broadside beam is calculated as shown in Fig. 3.11. Based on the transmission phase distribution, the low-RCS transmitarray and the reference one are designed by utilizing the phase controllable AFST elements and the elements without resistors, respectively.

The photos of the fabricated low-RCS transmitarray prototype are given in Fig. 3.12. As shown in the insets of Fig. 3.12, some of the elements are rotated by 90° to achieve the transmission phase change of 180°.

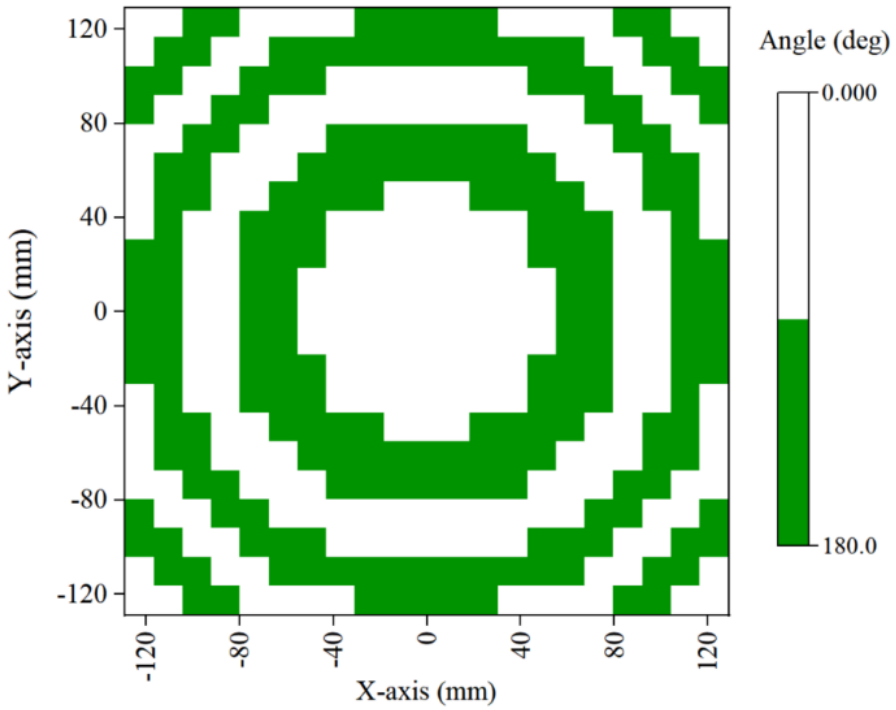


Figure 3.11: Calculated transmission phase distribution of low-RCS transmitarray and reference transmitarray.

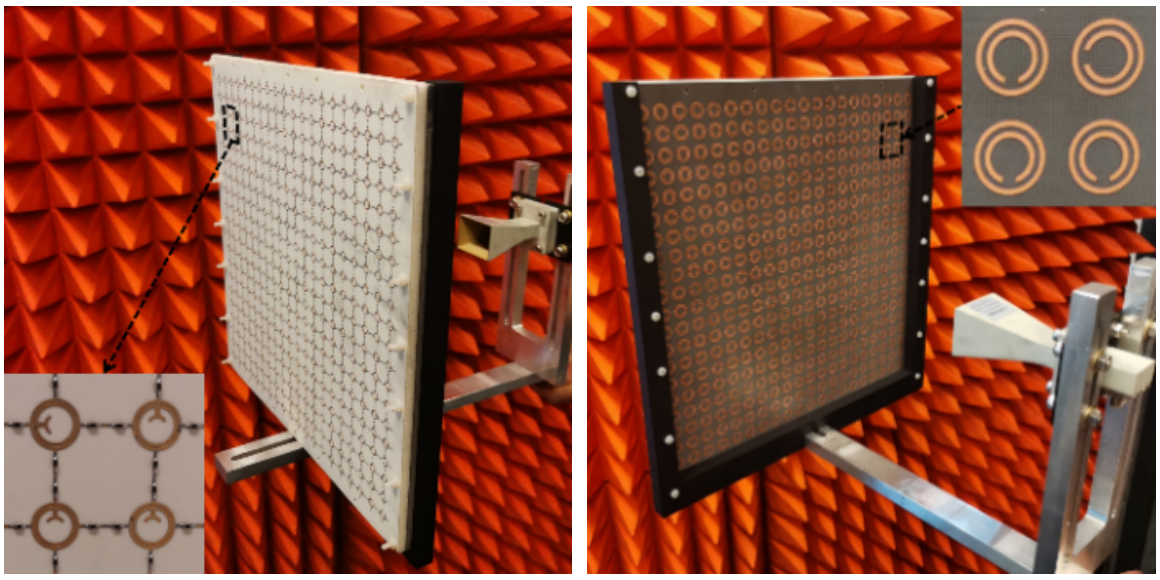

(a) (b)

Figure 3.12: Photographs of the fabricated low-RCS transmitarray. (a) Front side. (b) Back side.

### 3.3.2 Numerical and Experimental Results of the Low RCS Transmitarray Antenna

The simulated and measured input reflection coefficients of the proposed low-RCS transmitarray and the reference one are all below -10 dB from 11.9 GHz to 12.9 GHz, as shown in Fig. 3.13. The input reflection coefficients are with respect to the feeding gain horn port and describe the ratio of reflected power to input power for the antenna. As shown in Fig. 3.8, it is defined as how much of the incident power at the input feeding port is reflected. It is related to the input impedance looking from the feeding port of the gain horn.

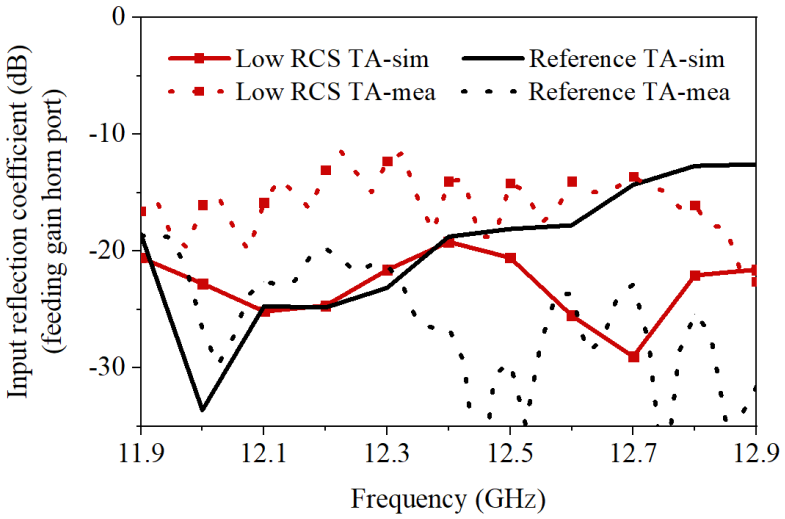


Figure 3.13: Simulated and measured reflection coefficients of low-RCS transmitarray and reference transmitarray.

The simulated and measured radiation patterns of the low-RCS transmitarray and the reference one at 12.5 GHz are compared. Their E-plane and H-plane are shown in Figs. 3.14 (a) and 3.14 (b), respectively. The simulated and measured realized gains and aperture efficiencies versus frequency for the two transmitarrays are given in Fig. 3.14 (c) and 3.14 (d), respectively. As seen from these figures, the simulated and measured radiation patterns agree reasonably well for each array. There is a 0.1 GHz frequency shift for the simulated and measured realized gains for both arrays. This can be due to the limitation of our workstation to simulate this electrically large size array or fabrication errors. The

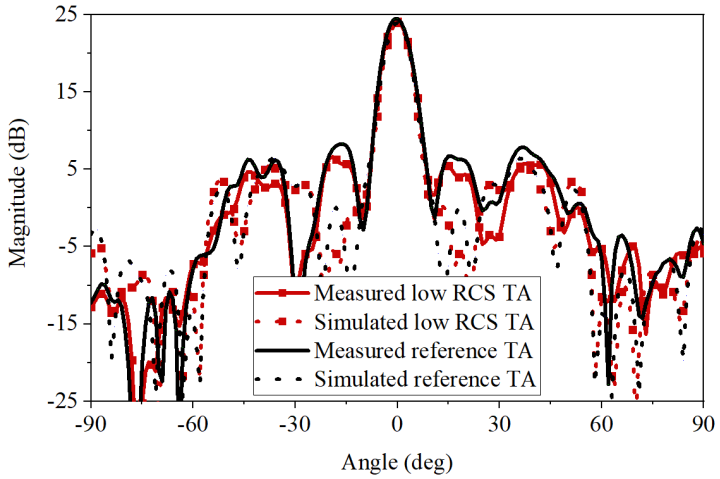


(a)

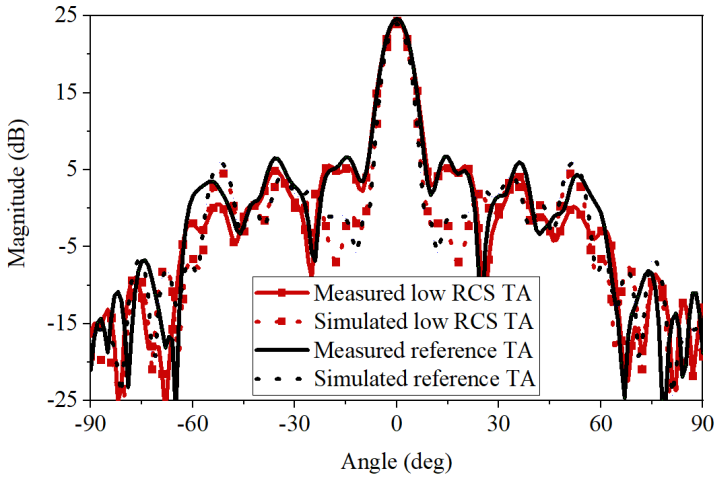


(b)

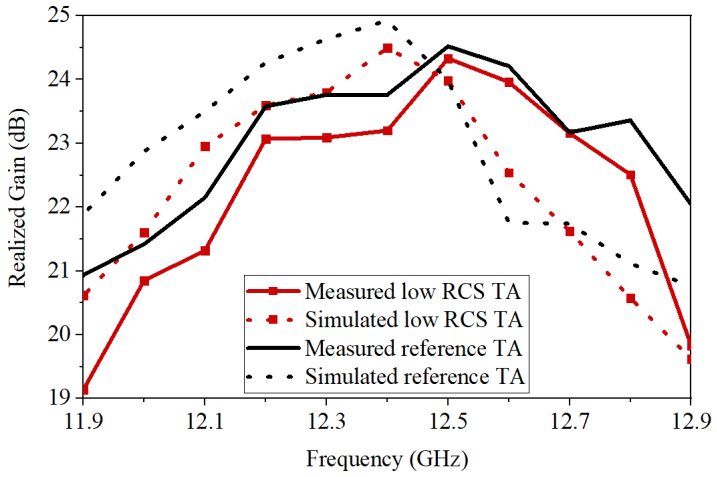


(c)

Figure 3.14: Radiation patterns and realized gains versus frequency of low-RCS transmitarray and reference transmitarray. (a) E-plane radiation patterns at 12.5 GHz. (b) H-plane radiation patterns at 12.5 GHz. (c) Realized gains versus frequency. (d) Aperture efficiencies versus frequency.

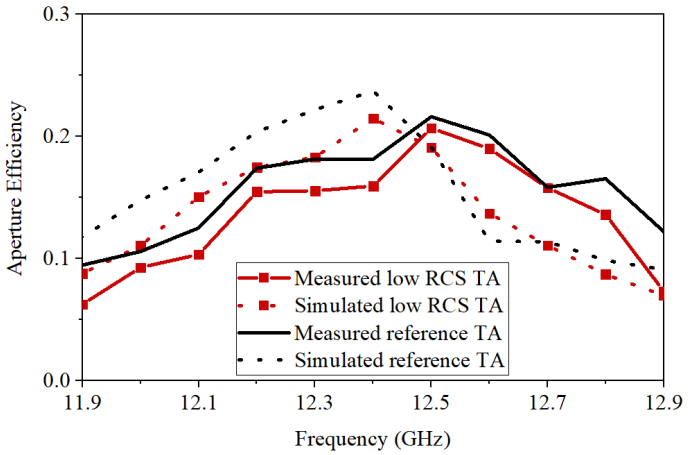


(d)

Figure 3.14: Radiation patterns and realized gains versus frequency of low-RCS transmitarray and reference transmitarray. (a) E-plane radiation patterns at 12.5 GHz. (b) H-plane radiation patterns at 12.5 GHz. (c) Realized gains versus frequency. (d) Aperture efficiencies versus frequency.

measured in-band 3-dB gain bandwidth is 6 % for the proposed low-RCS transmitarray. Furthermore, the measured patterns of the two transmitarrays agree very well with each other. The measured peak realized gains and aperture efficiencies of the low-RCS transmitarray and the reference one are 24.4 dBi (21.0 %) and 24.5 dBi (21.5 %) at 12.5 GHz, respectively. It indicates that the proposed phase controllable AFST elements with resistors have a negligible effect on the directivities and efficiencies of the antenna, which is because the induced currents passing through the lossy resistors are very small in the transmission band.

The RCS reduction performance is evaluated by comparing the RCS of the proposed low-RCS transmitarray with the reference one. The monostatic RCS of the two transmitarrays under normal and oblique incidence waves is measured. It is noted that both feed antennas of transmitarrays are terminated with matched loads during the measurement. The simulated and measured monostatic RCS are shown in Fig. 3.15 under normal impinging waves. Reasonably good agreement can be found. The discrepancies can be mostly attributed to the fabrication tolerance, multilayer alignment inaccuracies and measurement errors.

As shown in Fig. 3.15, under the normal impinging wave, the measured monostatic

RCS has more than 10 dB reduction for both polarizations from 10 to 12 GHz (18 %) and from 13 to 15 GHz (14 %). Ideally, the RCS performance for the two polarizations should be close to each other. However, due to the chamber's unequal response to the two polarizations, there are some discrepancies between the RCS reduction for two polarizations. For the operating band (transmission band) round 12.5 GHz, the RCS for both transmitarrays are very low. This is because the impinging EM waves can pass through the transmitarray aperture and focus back to the feed horn with matched loads.

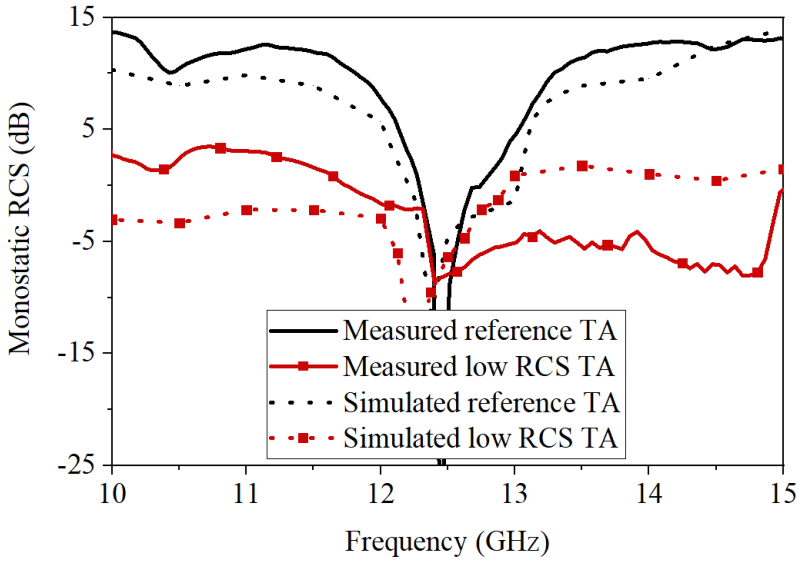


(a)

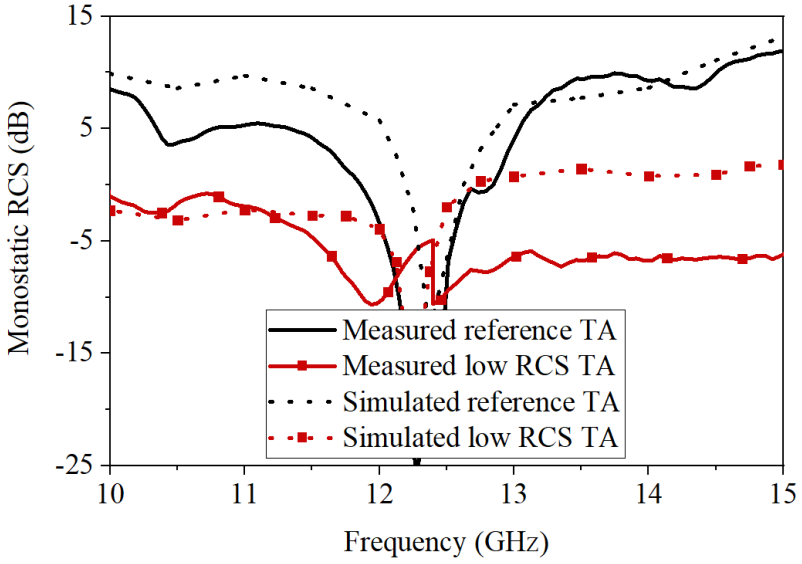


(b)

Figure 3.15: Monostatic RCS of low-RCS transmitarray and reference transmitarray under normal impinging wave. (a) Vertical polarization. (b) Horizontal polarization.

The RCS performance is also examined for oblique impinging angles which increases up to 45° for the horizontal polarization as shown in Fig. 3.16. Compared to the reference transmitarray, there is a remarkable RCS reduction at the out-of-band frequencies for the low-RCS one. It has shown that the proposed low-RCS transmitarray has achieved the RCS reduction under wide-angle impinging waves. A comparison of relevant transmitarray, reflectarray and patch antenna is shown in Table 3.1.

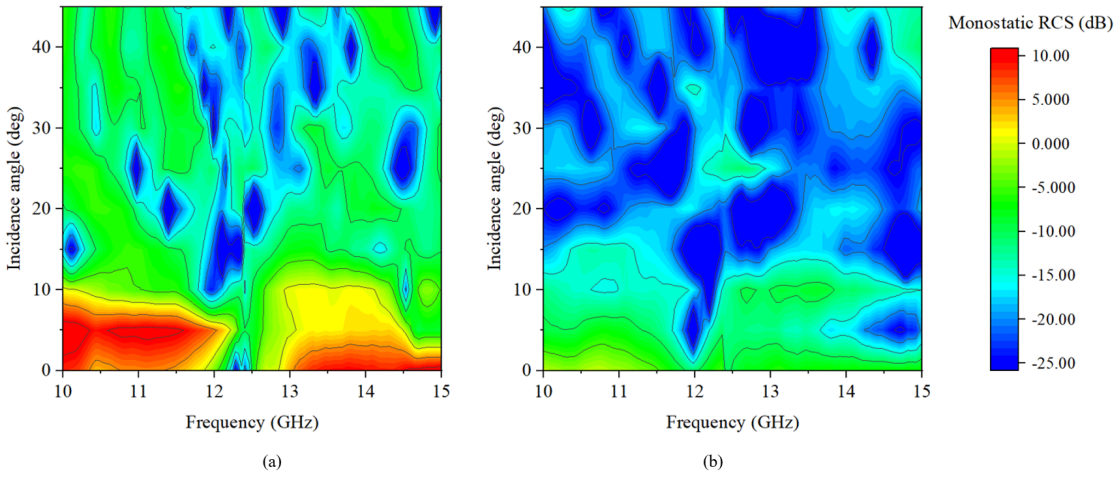


Figure 3.16: Measured monostatic RCS of two transmitarrays under wide-angle oblique impinging waves. (a) Reference transmitarray. (b) Low-RCS transmitarray.

Table 3.1: Comparison of Relevant Transmitarray (TA), Reflectarrays (RAs) or Patch Antenna

| | [30] | [29] | [20] | This Work |
|---|---|---|---|---|
| Theory | RA | RA | Patch | TA |
| Freq. (GHz) | 10.0 | 7.1 | 10.2 | 12.5 |
| Operating Band (GHz) | 9-10.5 | 6.8-7.7 | 9.7-10.7 | 11.9-12.9 |
| Thickness | 1.37$\lambda$ | 0.42$\lambda$ | 0.10$\lambda$ | 0.42$\lambda$ |
| RCSR Bandwidth (GHz) | 7-9.2 (>10 dB); 10.5-13 (>5 dB) | 2-4.5 (>10 dB); 9.1-10.8 (>8 dB) | 5.5-21.5 | 10-12 (>10 dB); 13-15 (>10 dB) |
| Gain | 22.0 dBi | 23.3 dBi | 10.0 dBi | 24.4 dBi |

## 3.4 Summary

A phase controllable AFST element is proposed to obtain an absorption-transmission-absorption scattering response, which consists of asymmetrical resonators integrated with resistors. A 1-bit phase change within the transmission band is achieved by rotating the elements. By utilizing the phase controllable AFST elements, a low-RCS transmitarray is designed, fabricated and measured. Compared with the reference transmitarray, the low-RCS one has a comparable realized gain. Meanwhile, significant RCS reductions have been achieved at lower and upper absorption bands outside the transmission band under normal and wide-angle oblique impinging waves for dual polarizations.

# 4

# Wideband Conformal Transmitarray

## 4.1 Introduction

Transmitarray antennas have attracted increasing attention in long-distance communications for space and terrestrial wireless systems due to their merits of high gain, low cost and flexible radiation performance, which can be a good antenna candidate for the 5G and beyond wireless networks with the requirements of high gain and low cost at mm-wave and THz bands [19]. Compared with the ground-based 5G wireless networks, the 6G networks are based on the integration of both terrestrial networks and space networks to provide a 3-D coverage for people and vehicles [70]. Due to the high path loss at mm-wave and THz bands, an airborne layer above the stratosphere needs to be deployed

to bridge wireless communication links between terrestrial and satellite platforms. For delivering the airborne layer, UAVs can be considered as one of the best candidates due to their high mobility and low cost.

Conventional transmitarray antennas are not suitable for UAVs as they would protrude from UAVs fuselage, which results in degraded motor performance and energy efficiency. To overcome this issue, conformal transmitarray antennas are developed to adapt the mounting platform shapes in order to achieve their aerodynamic requirements, which can be a part of the platform surface and accommodate a feeding antenna placed behind the transmitarray to utilize platform space better without destroying its aerodynamic performance. Some reported research efforts have been demonstrated to conformal transmitarrays [35–40].

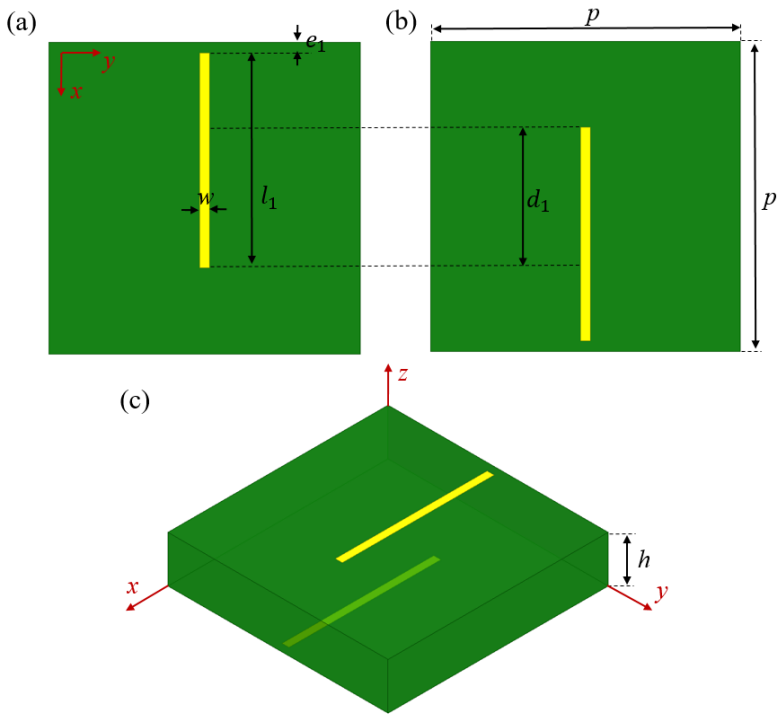


Figure 4.1: Configuration of the simple dual-layer Huygens element. (a) Top view. (b) Bottom view. (c) 3D view.

Based on the current fabrication technology, metallic ink can be printed on a curved structure. However, the implementation of metal printing on curved surface is very expensive and technically difficult. Thus, one of the feasible methods to realize a confor-

mal transmitarray is to bend an ultrathin planar transmitarray based on a desired shape. By using this realization method, two cylindrically conformal transmitarray were developed [37, 39] with limited bandwidth which are not suitable for many platforms and wireless communication systems. An ultrawideband cylindrically conformal transmitarray was proposed employing connected slot-bowtie elements with true-time delay lines achieving an operating band from 8.5 to 17 GHz [38]. However, its elements are vertically connected by soldering, which may result in manufacture difficulties, alignment errors especially at higher frequencies and degraded aerodynamic performance. Thus, it can be found that it is highly desired to develop wideband conformal dual-layer transmitarray to support high data rate and aerodynamic requirements with reduced alignment errors.

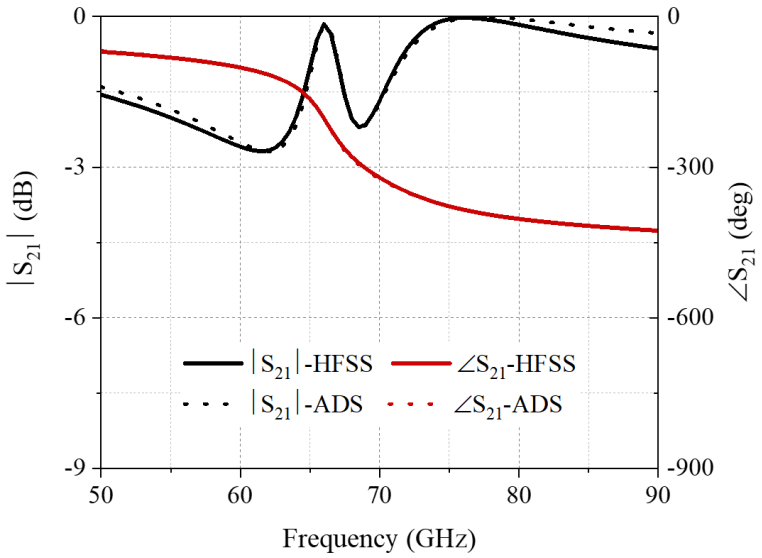


Figure 4.2: Transmission coefficients of the simple dual-layer Huygens element.

Over the E-band of 71-76 and 81-86 GHz (gigabyte wireless spectrum), the atmospheric absorption rate is relatively low, providing the capability of long-distance gigabyte point-to-point wireless services. The wide bandwidth and the low atmospheric absorption at E-band have spurred many applications and innovations for 5G and 6G wireless communication systems. Thus, in this chapter, a wideband conformal transmitarray employing dual-layer tightly coupled Huygens elements at E-band is developed. The element consists of five pairs of partly overlapped metallic striplines with different lengths printed

on two layers of a dielectric substrate, which can provide tightly coupled Huygens resonances with nearly total transmission and full transmission phase coverage in a wide bandwidth. To validate the design concept, a cylindrically conformal transmitarray at 78 GHz is designed, fabricated and measured. Continuous phase compensation of 360° on the aperture is achieved by tuning the lengths of the striplines, reducing phase errors of the array architecture. Good agreement between the measured and simulated results is found, showing a peak measured realized gain of 26.6 dBi with an aperture efficiency of 35.9 % at 78.5 GHz and measured 3-dB bandwidth of 20.4 % from 71 GHz to 87 GHz.

## 4.2 Wideband Dual-Layer Huygens Element

To design a wideband transmitarray, both wide magnitude bandwidth and wide phase bandwidth are required for the elements on the aperture of the transmitarray. This means the transmission loss of each element should be less than 3 dB in a wideband; the transmission phase coverage of each element should be at least nearly 360° in a wideband; the transmission phase difference between arbitrary two elements on the aperture of the transmitarray should be stable in a wideband. For this target, a dual-layer tightly coupled Huygens element is proposed.

### 4.2.1 Dual-Layer Huygens Element

A Huygens resonance consists of orthogonally induced electric and magnetic currents which are in-phase. The balanced condition between electric and magnetic responses can result in a total transmission and zero reflection which are beneficial to a high-efficiency transmitarray design. A simple realization of a dual-layer Huygens element is using a pair of partly overlapped metallic striplines printed on two layers of a dielectric substrate as shown in Fig. 4.1. The dielectric substrate is Rogers RT/duroid 5880 with relative permittivity of 2.2, dielectric loss tangent of 0.009, and thickness $h$ of 0.508 mm. The top layer is symmetric to the bottom layer along y-axis. The parameter values are as follows:

$p$ = 2.401 mm, $l_1$ = 1.655 mm, $d_1$ = 1.073 mm, $e_1 = (p + d_1)/2 - l_1$ and $w$ = 0.075 mm.

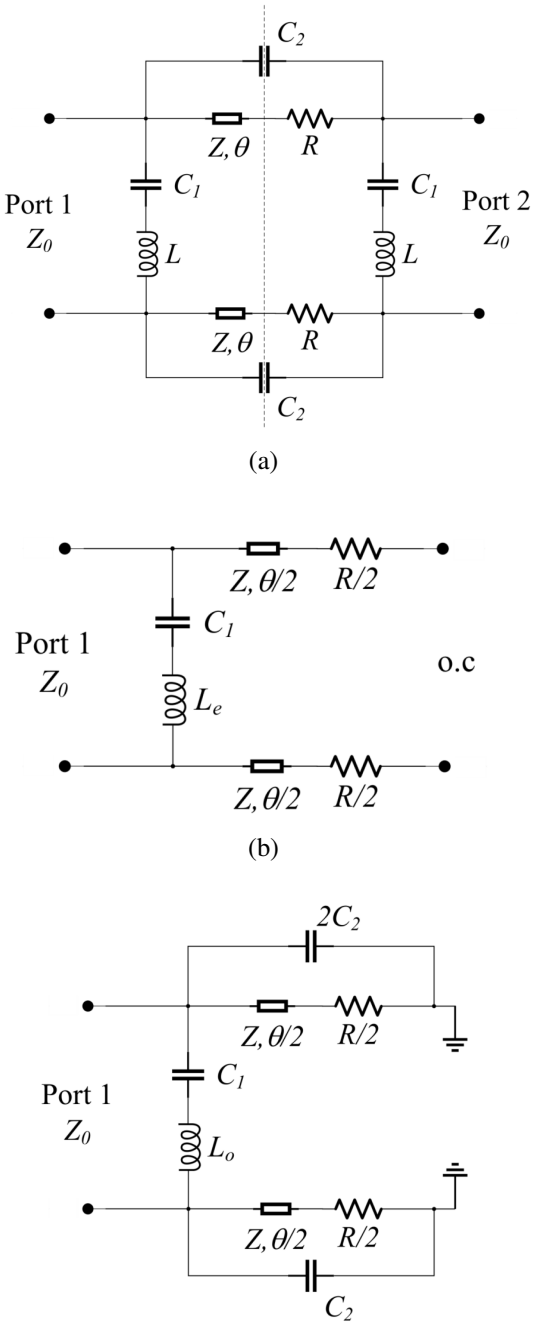


Figure 4.3: (a) Equivalent circuit model of the simple dual-layer Huygens element. (b) Even mode decomposed circuit. (c) Odd mode decomposed circuit. The values of the parameters are as follows: $L_e$ = 3.26 nH, $L_o$ = 2.73 nH, $C_1$ = 1.89 fF. $C_2$ = 0.55 fF, $Z_0$ = 377 , $Z$ = 254 , $\theta$ = 60.58° and $R$ = 1.77 Ω.

A simple way to illustrate the simple dual-layer Huygens element is using an equivalent circuit model, as shown in Fig. 4.3 (a). Under x-polarized incidence waves, an

electric current on the metallic striplines of the top or bottom layer is induced, which is represented by an inductance, $L$. A series capacitance $C_1$ exists between two neighboring metallic striplines of the top or bottom layer. The dielectric substrate is represented by a transmission line with the impedance of $Z$ and the electrical length of $\theta$. A coupling capacitance also exists between the two metallic striplines of top and bottom layers, represented by a capacitance $C_2$. The equivalent circuit shown in Fig. 4.3 (a) are further split to emphasize longitudinal symmetries of the structure.

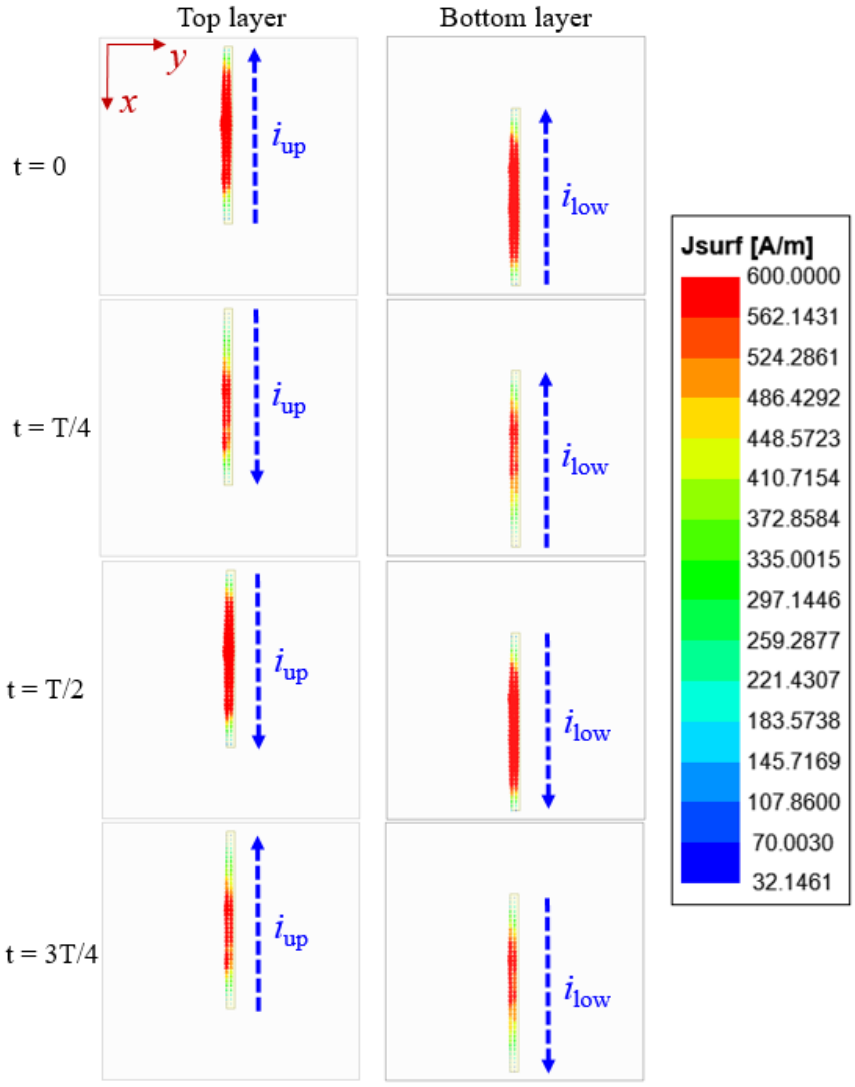


Figure 4.4: Induced surface currents on top and bottom layers of the simple dual-layer Huygens element in a time period T.

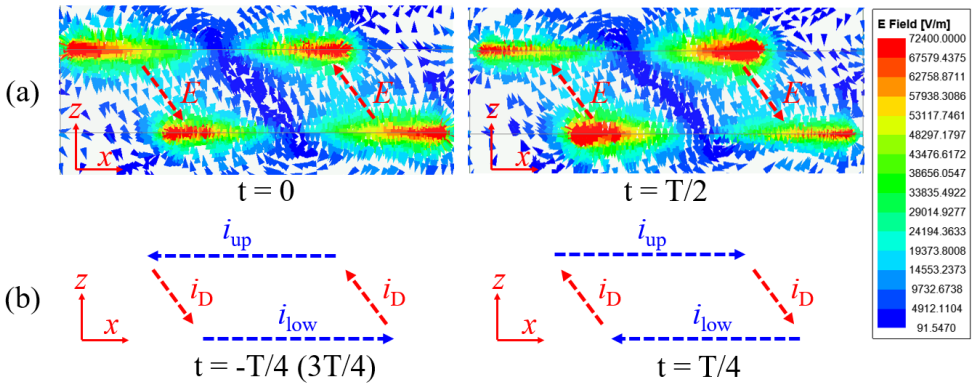


Figure 4.5: (a) Electric field of the simple dual-layer Huygens element on xoz plane at t = 0 and t = T/2. (b) Surface and displacement currents of the simple dual-layer Huygens element on xoz-plane at t = -T/4(3T/4) and t = T/4.

The longitudinal symmetry allows an even-odd mode decomposition of the structure. The equivalent circuit model of the even and odd mode decomposed circuits are shown in Fig. 4.3 (b) and 4.3 (c). In the even mode, the coupling capacitance $C_2$ has no contributions due to open circuit termination at the longitudinal symmetry plane, as shown in Fig. 4.3 (b). This even mode can provide an electric current for the dual-layer Huygens resonance. As shown in Fig. 4.3 (c), in the odd mode, the coupling capacitance $C_2$ causes the displacement current between the two metallic striplines of the top and bottom layers. This odd mode can provide a magnetic current for the dual-layer Huygens resonance. Moreover, the transmission and reflection coefficients of the simple dual-layer Huygens element can be obtained using the superposition of those of the even and odd modes:

$$S_{21} = \left( \frac{S_{11,even} + S_{11,odd}}{2} \right) \tag{4.1a}$$

$$S_{11} = \left( \frac{S_{11,even} - S_{11,odd}}{2} \right) \tag{4.1b}$$

The element is simulated using master/slave boundary conditions and Floquet ports of 3D EM simulation software HFSS. As shown in Fig. 4.2, its transmission loss is less than 2.7 dB and transmission phase coverage is about 360°from 50 GHz to 90 GHz. The

equivalent circuit model shown in Fig. 4.3 (a) is used to reproduce the full-wave response of the element configuration. Using 4.1a and 4.1b, various lumped circuit elements (i.e. $L_e$, $L_o$, $C_1$, $C_2$, $Z_0$, $Z$, $\theta$ and $R$) are determined using numerical optimization to match the full-wave response of the element.

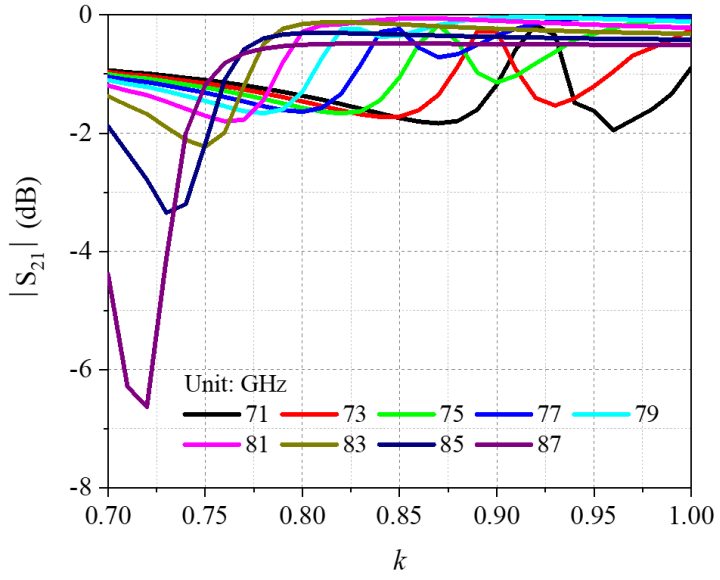


(a)

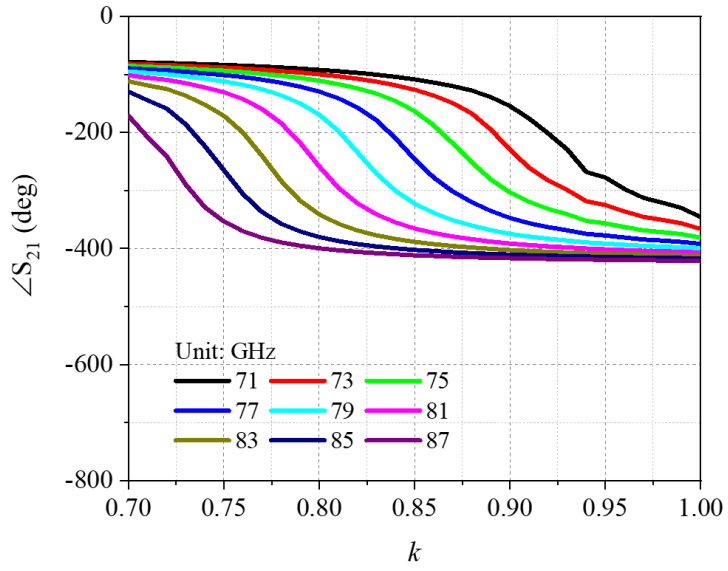


(b)

Figure 4.6: Transmission coefficients of the simple dual-layer Huygens element with different values of scale factor $k$. (a) Magnitudes. (b) Phases.

When the element is illuminated by an x-polarized wave, currents will be induced on the metallic striplines on both layers of the element. The induced surface currents on top

and bottom layers of the simple dual-layer Huygens element at 76 GHz are shown in Fig. 4.4. The currents on top and bottom layers are named as $i_{up}$ and $i_{low}$, respectively. As shown in Fig. 4.4, the directions of $i_{up}$ and $i_{low}$ are the same in the first and third quarters of one time period T, providing an electric current along x-axis. In the second and fourth quarters of T, the directions of $i_{up}$ and $i_{low}$ are opposite. Moreover, the electric fields of the dual-layer Huygens element on xoz-plane at t = 0 or t = T/2 are shown in Fig. 4.5 (a). Based on $i_D = \varepsilon \frac{\partial E}{\partial t}$, the electric fields between top and bottom layers at t = 0 and t = T/2 can provide displacement currents $i_D$ between top and bottom layers at t = -T/4 (3T/4) and t = T/4, respectively. As shown in Fig. 4.5 (b), the displacement currents with the opposite currents on top and bottom layers can provide a current loop which can be equivalent to a magnetic current with a time delay of T/4.

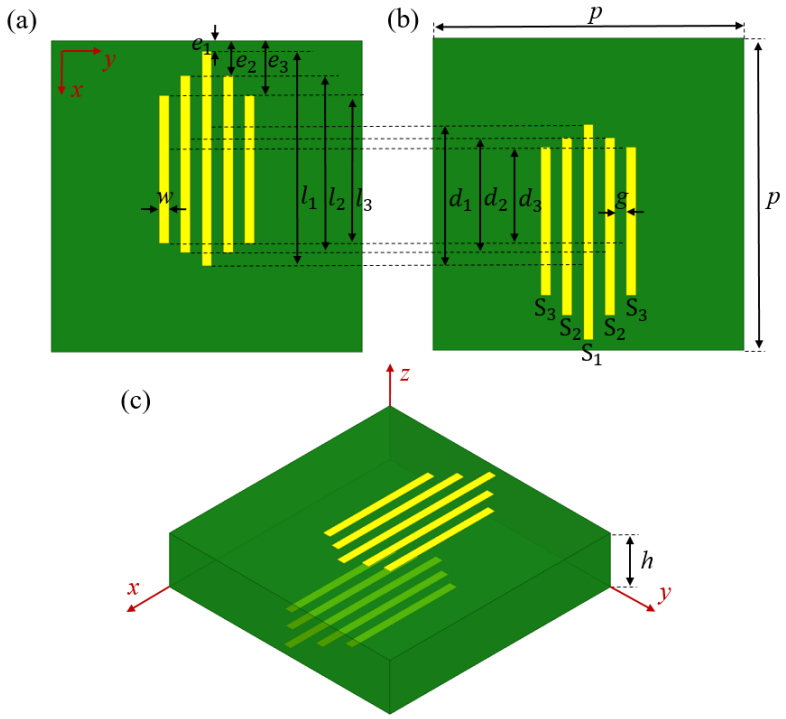


Figure 4.7: Configuration of the dual-layer tightly coupled Huygens element. (a) Top view. (b) Bottom view. (c) 3D view.

Thus, the orthogonally induced electric and magnetic currents appear simultaneously, exciting a Huygens resonance in the element. The length of the metallic stripline, $l_1$, along x-axis controls the resonant frequency of the Huygens resonance, and the length of the

overlapped part of the metallic stripline, $d_1$, provides fine tuning to achieve the balanced condition of a Huygens resonance.

Multiplying parameters $l_1$, $l_2$, $l_3$, $d_1$, $d_2$ and $d_3$ by a scale factor $k$, respectively, the transmission coefficients of the simple dual-layer Huygens element with different values of $k$ from 0.7 to 1.0 are shown in Fig. 4.6. It can be seen that the transmission loss of the element are not less than 3 dB; the transmission phase coverage are not at least nearly 360°; the transmission phase difference corresponding to an arbitrary $k$ variation are not stable from 71 GHz to 86 GHz. Thus, this simple dual-layer Huygens element are not suitable for a wideband transmitarray design.

### 4.2.2 Dual-Layer Tightly Coupled Huygens Element

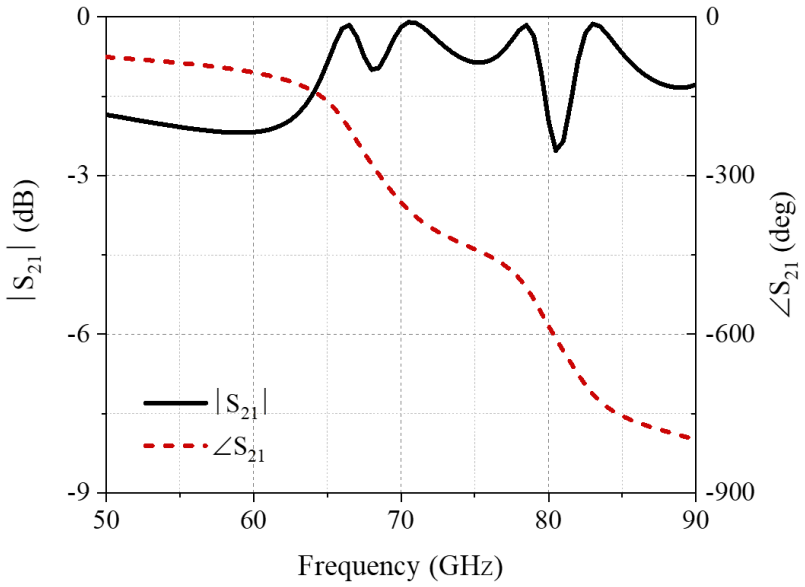


Figure 4.8: Transmission coefficients of the dual-layer tightly coupled Huygens element.

To achieve the transmission loss of less than 3 dB, the transmission phase coverage of nearly 360° and stable transmission phase difference corresponding to an arbitrary parameter variation in a wideband, a dual-layer tightly coupled Huygens element is proposed. The configuration of the element is demonstrated in Fig. 4.7. It consists of five pairs of partly overlapped metallic striplines, a $S_1$, two $S_2$ and two $S_3$ symmetric to x-axis, with

different lengths printed on two layers of a dielectric substrate. The dielectric substrate is the same as that of the simple dual-layer Huygens element. The top layer is symmetric to the bottom layer along y-axis, and both top and bottom layers are symmetric to x-axis. The parameter values are as follows: $p$ = 2.401 mm, $l_1$ = 1.655 mm, $l_2$ = 1.366 mm, $l_3$ = 1.138 mm, $d_1$ = 1.073 mm, $d_2$ = 0.868 mm, $d_3$ = 0.723 mm, $e_{1,2,3} = (p + d_{1,2,3})/2 - l_{1,2,3}$ and $w$ = 0.075 mm.

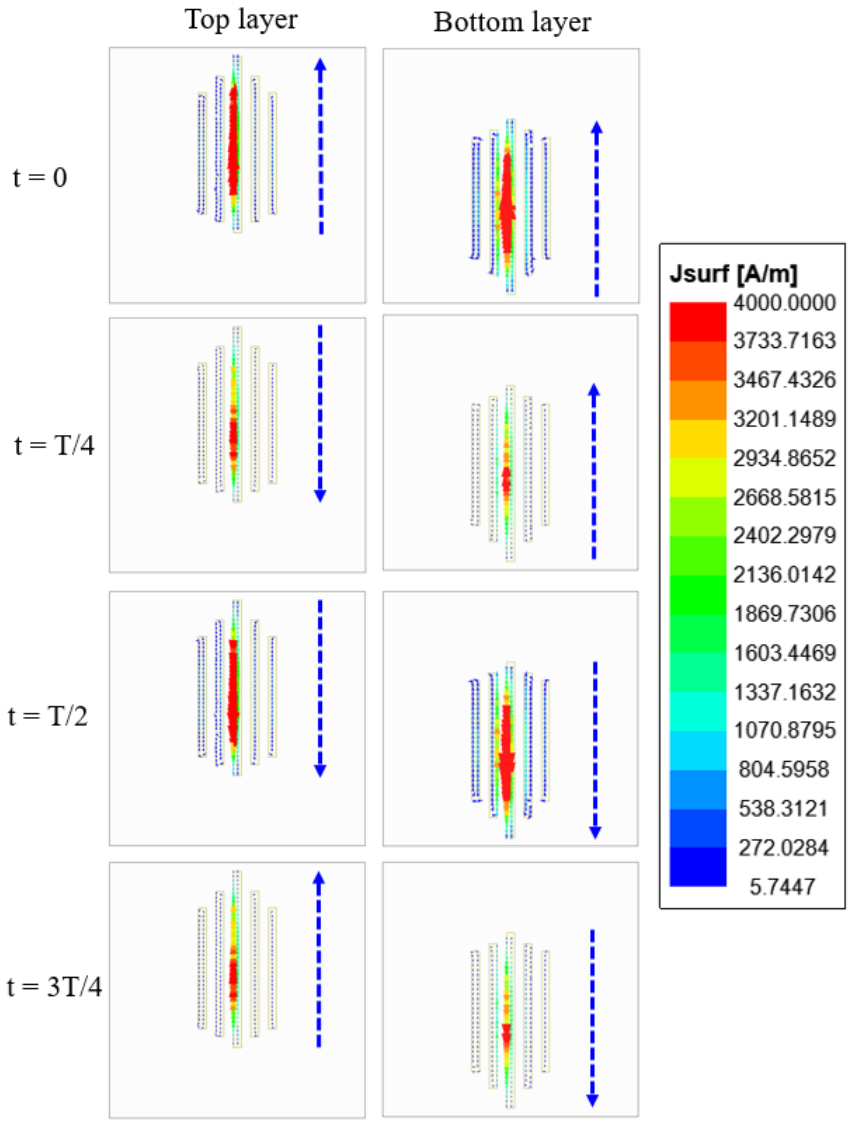


Figure 4.9: Induced surface current distributions on top and bottom layers of the dual-layer tighly coupled Huygens element at 71 GHz.

The proposed element is simulated using master/slave boundary conditions and Floquet ports of 3D EM simulation software HFSS. The simulated transmission coefficients

of the dual-layer tightly coupled Huygens element are shown in Fig. 4.8. It is seen from Fig. 4.8 that the transmission loss is less than 2.5 dB and the phase variation range is 725° from 50 to 90 GHz for the dual-layer tightly coupled Huygens element.

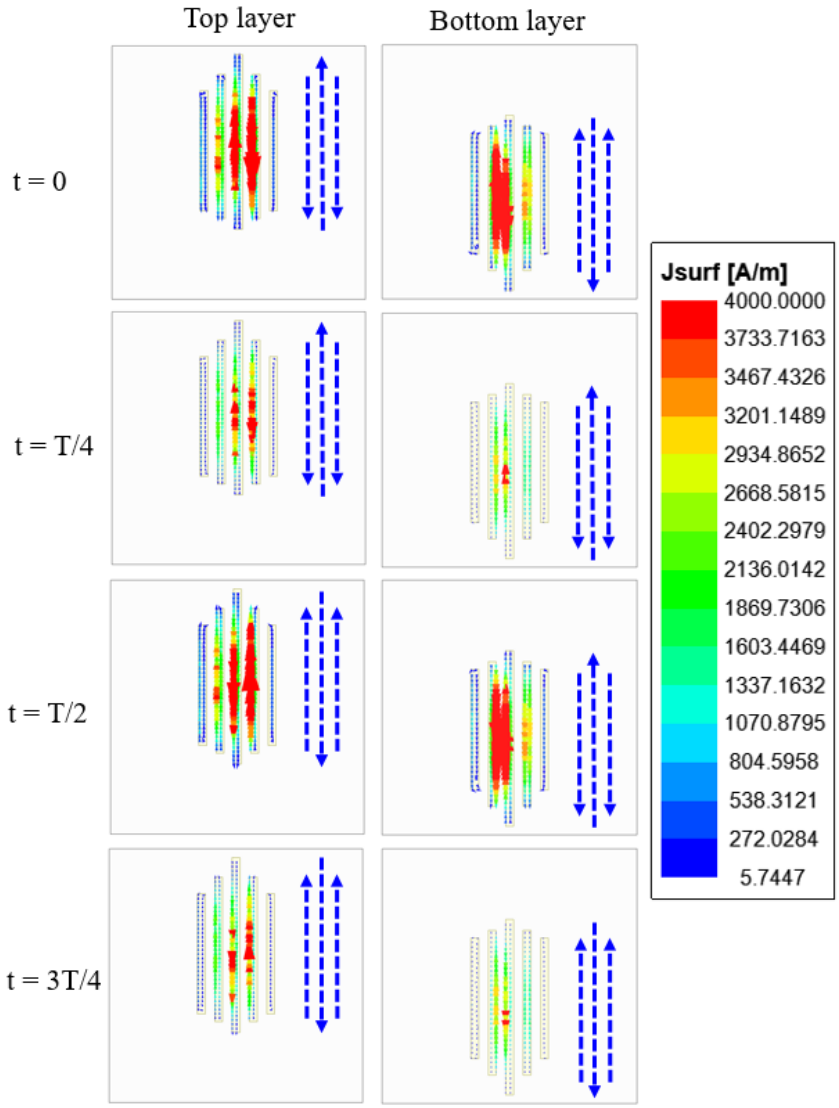


Figure 4.10: Induced surface current distributions on top and bottom layers of the dual-layer tighly coupled Huygens element at 78.5 GHz.

Compared to the simple dual-layer Huygens element, the dual-layer tightly coupled Huygens element based on multiple Huygens resonances significantly reduces the transmission loss and greatly improves the transmission phase coverage, due to their coupling capacitance between each neighboring pair of metallic striplines. With the amount of the metallic striplines increased, the bandwidth of the Huygens element can be improved.

However, when the amount of the striplines is larger than five pairs, this improvement would be minute and the structure complexity would also be increased. Therefore, the dual-layer tightly coupled Huygens element with five pairs of metallic striplines is chosen for a wideband transmitarray design.

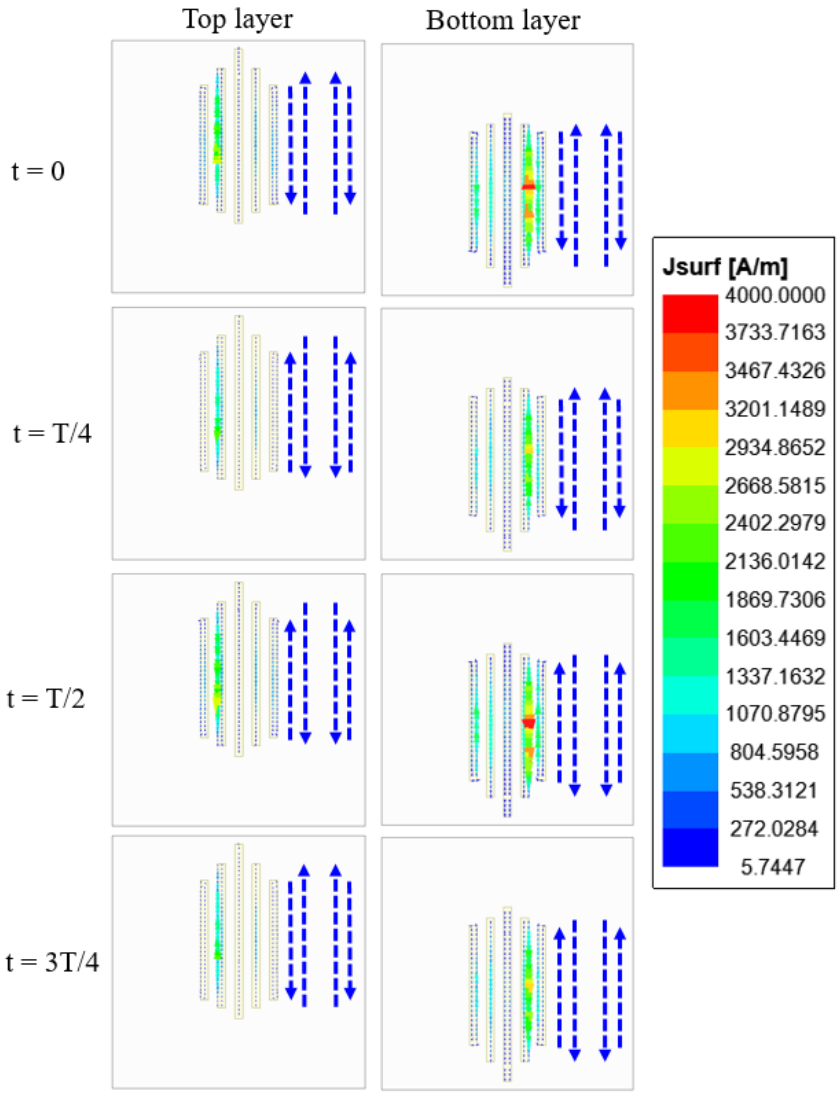


Figure 4.11: Induced surface current distributions on top and bottom layers of the dual-layer tighly coupled Huygens element at 86 GHz.

An x-polarized normal incident plane wave is used to illuminate the element. The simulated surface currents on the top and bottom layers of the dual-layer tightly coupled Huygens element at 71 GHz, 78.5 GHz and 86 GHz are shown in Figs. 4.9, 4.10 and 4.11, respectively.

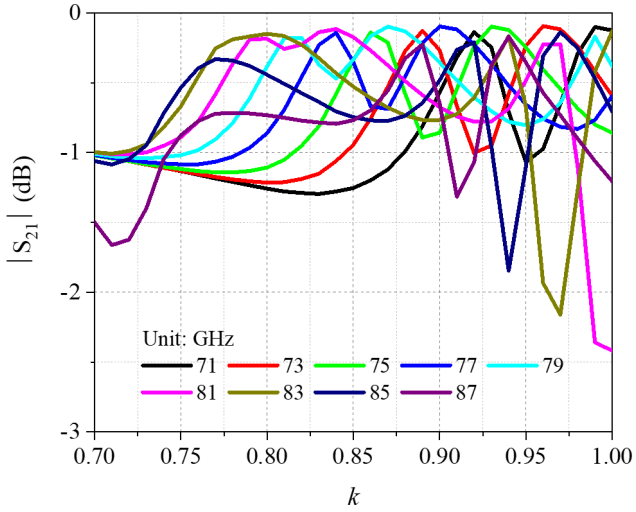


(a)

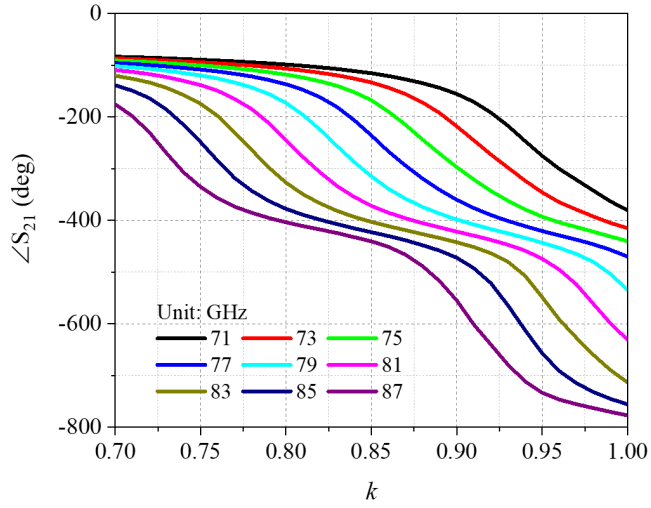


(b)

Figure 4.12: Transmission coefficients of the dual-layer tightly coupled Huygens element with different values of scale factor $k$. (a) Magnitudes. (b) Phases.

As shown in Fig. 4.9, the currents are mainly induced on the longest metallic striplines $S_1$ of top and bottom layers at 71 GHz. The directions of the currents on the striplines $S_1$ of top and bottom layers are the same leading to an equivalent electric dipole in the first and third quarters of time period T. The directions of the currents on the striplines $S_1$ of top and bottom layers are opposite in the second and fourth quarters of T, providing a current loop in the overlapped areas of the two striplines $S_1$ along x-axis on the two layers of the substrate. This current loop can be equivalent to a magnetic response dipole with a time delay of a quarter of T. Thus, the orthogonally induced electric and magnetic dipoles

appear simultaneously, which means a Huygens resonance is excited in the element at 71 GHz.

Table 4.1: Transmission Losses and Phase Coverages of the Dual-Layer Tightly Coupled Huygens Element at Different Frequencies

| Frequency | 71 GHz | 73 GHz | 75 GHz |
|---|---|---|---|
| Phase coverage | 297° | 328° | 349° |
| Max. tran. loss | 1.3 dB | 1.2 dB | 1.1 dB |
| Frequency | 77 GHz | 79 GHz | 81 GHz |
| Phase coverage | 374° | 432° | 521° |
| Max. tran. loss | 1.1 dB | 1.0 dB | 2.4 dB |
| Frequency | 83 GHz | 85 GHz | 87 GHz |
| Phase coverage | 592° | 617° | 601° |
| Max. tran. loss | 2.2 dB | 1.8 dB | 1.3 dB |

As shown in Fig. 4.10, the currents are mainly induced on the metallic striplines $S_1$ and $S_2$ of top and bottom layers at 78.5 GHz. In the first and third quarters of T, the directions of the currents on the striplines $S_1$ and $S_2$ of top layer are opposite as those on the corresponding striplines $S_1$ and $S_2$ of bottom layer providing three current loops which can be equivalent to three magnetic dipoles with time delays of a quarter of T. The directions of the currents on the striplines $S_1$ and $S_2$ of top layer are the same as those on the corresponding striplines $S_1$ and $S_2$ of bottom layer leading to three equivalent electric dipoles in the second and fourth quarters of T. Thus, three Huygens resonances are excited in the element at 78.5 GHz. Please be noted that the radiation directions of the three Huygens resonances are the same as -z direction, although the directions of the currents on the striplines $S_2$ and $S_3$ on each layer are different.

As shown in Fig. 4.11, the currents are mainly induced on the metallic striplines $S_2$ and $S_3$ of top and bottom layers at 86 GHz. The directions of the currents on the striplines $S_2$ and $S_3$ of top layer are the same as those on the corresponding striplines $S_2$ and $S_3$ of bottom layer leading to four equivalent electric dipoles in the first and third quarters of T. In the second and fourth quarters of T, the directions of the currents on the striplines

$S_2$ and $S_3$ of top layer are opposite as those on the corresponding striplines $S_2$ and $S_3$ of bottom layer providing four current loops which can be equivalent to four magnetic dipoles with time delays of a quarter of T. Similarly, four Huygens resonances radiating at -z direction are excited in the element at 86 GHz.

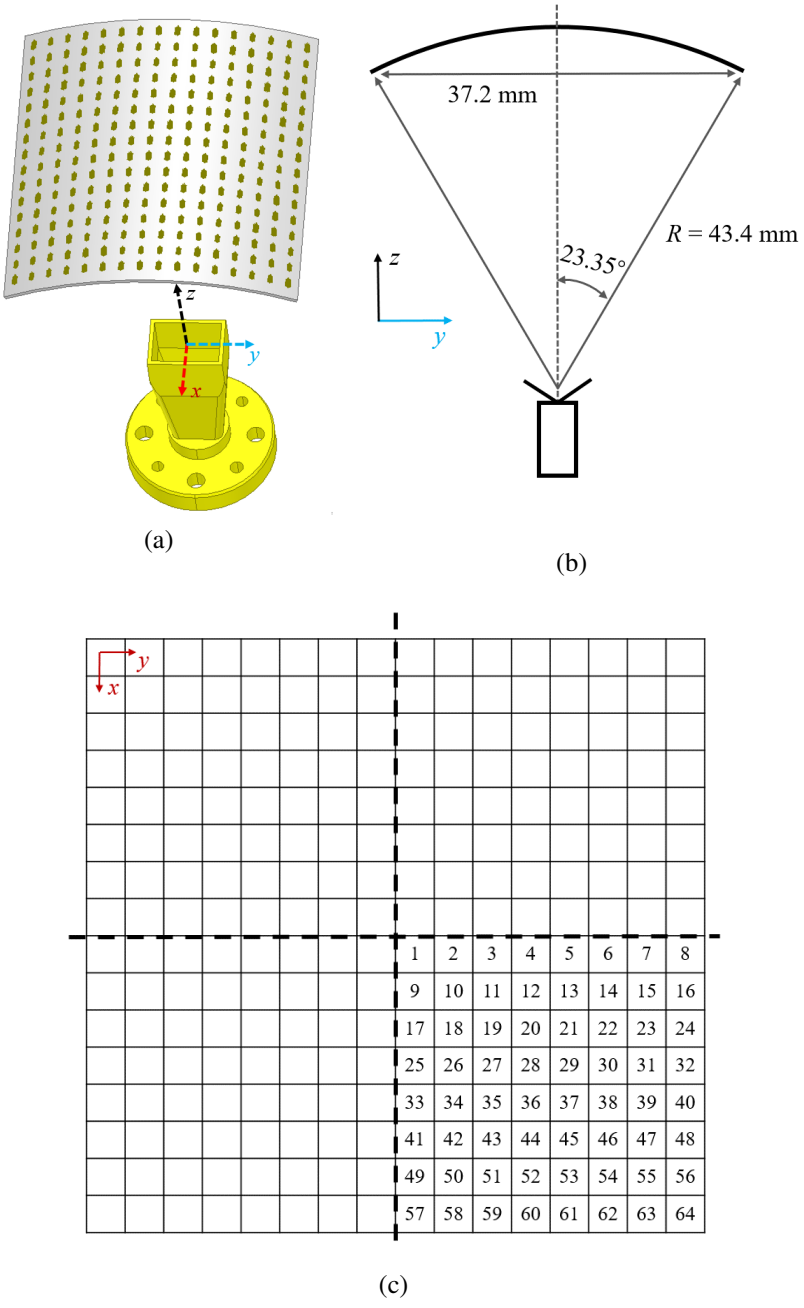


Figure 4.13: Cylindrically conformal transmitarray antenna: (a) 3D view; (b) schematic of front view. (c) The No. of the scale factor $k$ distributions on a quarter of the transmitarray.

In conclusion, multiple pairs of metallic striplines with different lengths in the ele-

ment can provide multiple Huygens resonances with low transmission losses in a wide operating band from 71 GHz to 86 GHz. The lengths of the metallic striplines, $S_1$, $S_2$ and $S_3$, along x-axis are $l_1$, $l_2$ and $l_3$, respectively, which control the resonant frequencies of each Huygens resonance. The lengths of the overlapped parts of the striplines, $S_1$, $S_2$ and $S_3$, along x-axis on each layer are $d_1$, $d_2$ and $d_3$, respectively, which provide fine tuning to achieve the balanced condition of multiple Huygens resonances.

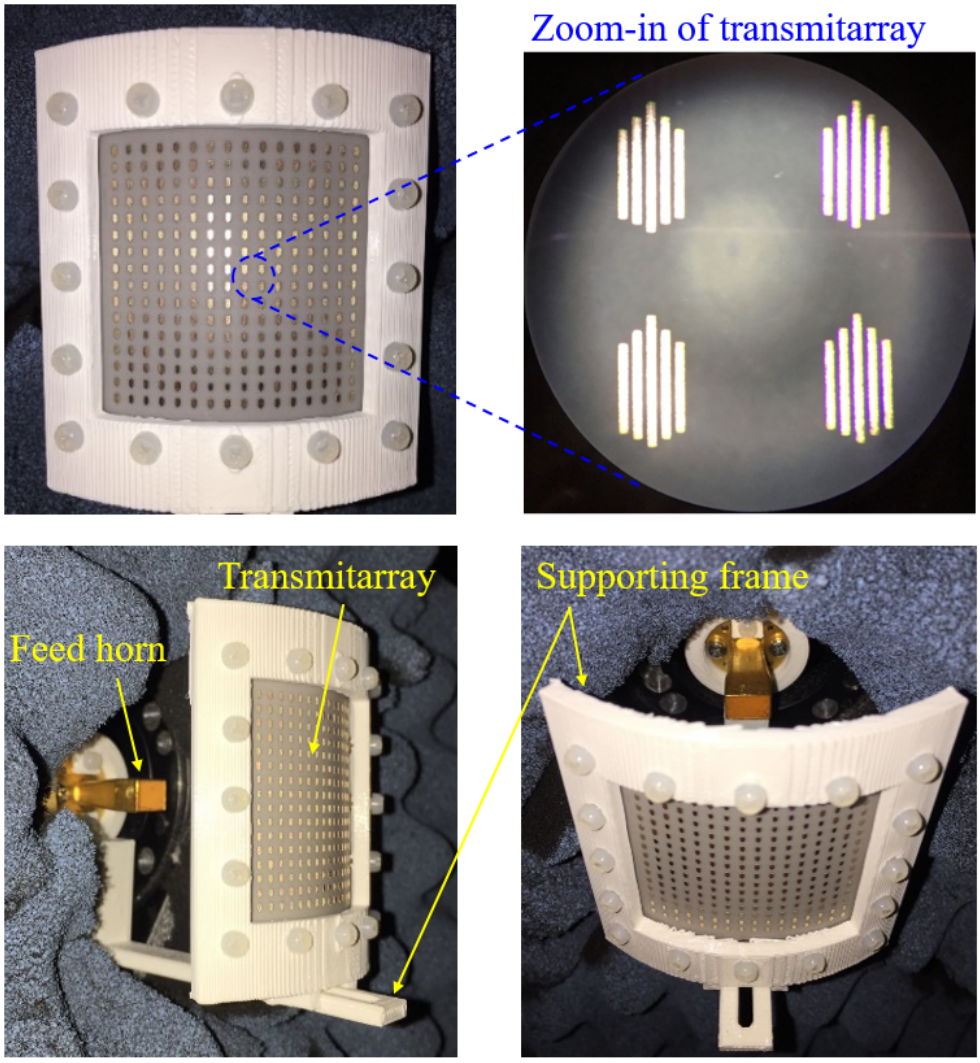


Figure 4.14: Photographs of the fabricated wideband conformal transmitarray antenna.

Multiplying parameters $l_1$, $l_2$, $l_3$, $d_1$, $d_2$ and $d_3$ by a scale factor $k$ respectively, the simulated transmission coefficients of the proposed element with different values of $k$ from 0.7 to 1.0 are shown in Fig. 4.12. The maximum transmission losses and phase

Table 4.2: Transmission Losses and Phases of the Dual-Layer Tightly Coupled Huygens Element with Different Values of Scale Factor $K$ at 78 GHz

| No. | $k$ | Tran. loss | Tran. phase | No. | $k$ | Tran. loss | Tran. phase |
|---|---|---|---|---|---|---|---|
| 1 | 0.900 | 0.4 dB | -398° | 33 | 0.836 | 0.4 dB | -275° |
| 2 | 0.889 | 0.2 dB | -386° | 34 | 0.832 | 0.4 dB | -263° |
| 3 | 0.872 | 0.1 dB | -361° | 35 | 0.824 | 0.3 dB | -238° |
| 4 | 0.854 | 0.3 dB | -325° | 36 | 0.811 | 0.2 dB | -199° |
| 5 | 0.836 | 0.4 dB | -275° | 37 | 0.785 | 0.7 dB | -150° |
| 6 | 0.816 | 0.2 dB | -213° | 38 | 0.954 | 0.8 dB | -447° |
| 7 | 0.774 | 0.9 dB | -138° | 39 | 0.880 | 0.1 dB | -374° |
| 8 | 0.914 | 0.5 dB | -412° | 40 | 0.840 | 0.5 dB | -287° |
| 9 | 0.889 | 0.2 dB | -386° | 41 | 0.816 | 0.2 dB | -213° |
| 10 | 0.880 | 0.1 dB | -374° | 42 | 0.812 | 0.2 dB | -202° |
| 11 | 0.865 | 0.1 dB | -349° | 43 | 0.802 | 0.3 dB | -178° |
| 12 | 0.849 | 0.4 dB | -312° | 44 | 0.775 | 0.9 dB | -139° |
| 13 | 0.832 | 0.4 dB | -263° | 45 | 0.956 | 0.8 dB | -449° |
| 14 | 0.811 | 0.2 dB | -199° | 46 | 0.890 | 0.2 dB | -387° |
| 15 | 0.758 | 1.0 dB | -125° | 47 | 0.849 | 0.4 dB | -312° |
| 16 | 0.900 | 0.4 dB | -398° | 48 | 0.821 | 0.2 dB | -228° |
| 17 | 0.872 | 0.1 dB | -361° | 49 | 0.779 | 0.8 dB | -142° |
| 18 | 0.865 | 0.1 dB | -349° | 50 | 0.765 | 0.9 dB | -130° |
| 19 | 0.854 | 0.3 dB | -325° | 51 | 0.970 | 0.6 dB | -465° |
| 20 | 0.840 | 0.5 dB | -287° | 52 | 0.932 | 0.7 dB | -427° |
| 21 | 0.824 | 0.3 dB | -238° | 53 | 0.883 | 0.2 dB | -378° |
| 22 | 0.801 | 0.3 dB | -176° | 54 | 0.850 | 0.3 dB | -315° |
| 23 | 0.966 | 0.7 dB | -460° | 55 | 0.825 | 0.3 dB | -241° |
| 24 | 0.880 | 0.1 dB | -374° | 56 | 0.789 | 0.6 dB | -155° |
| 25 | 0.854 | 0.3 dB | -325° | 57 | 0.923 | 0.6 dB | -419° |
| 26 | 0.849 | 0.4 dB | -312° | 58 | 0.910 | 0.5 dB | -408° |
| 27 | 0.840 | 0.5 dB | -287° | 59 | 0.889 | 0.2 dB | -386° |
| 28 | 0.828 | 0.3 dB | -251° | 60 | 0.863 | 0.2 dB | -345° |
| 29 | 0.811 | 0.2 dB | -199° | 61 | 0.843 | 0.4 dB | -296° |
| 30 | 0.773 | 0.9 dB | -137° | 62 | 0.823 | 0.2 dB | -234° |
| 31 | 0.925 | 0.7 dB | -421° | 63 | 0.792 | 0.6 dB | -159° |
| 32 | 0.859 | 0.2 dB | -337° | 64 | 0.939 | 0.8 dB | -433° |

coverages of the element at different frequencies are shown in Table 4.1. From 71 GHz to 87 GHz, the maximum transmission loss is less than 2.4 dB and the phase coverage is over 300°. In summary, the dual-layer tighly coupled Huygens element with different values of scale factor $k$ can provide over 300° continuous phase coverage when transmission loss is less than 2.4 dB from 71 GHz to 87 GHz.

## 4.3 Wideband Conformal Transmitarray Antenna

### 4.3.1 Wideband Conformal Transmitarray Prototype Design and Implementation

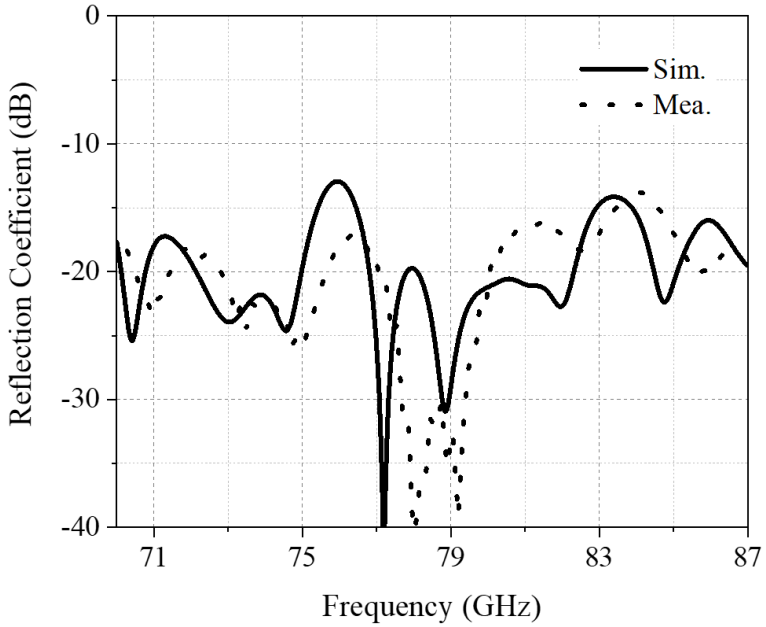


Figure 4.15: Measured and simulated reflection magnitudes of the wideband conformal transmitarray antenna.

To verify the feasibility of the dual-layer tightly coupled Huygens element, a cylindrically conformal transmitarray is designed with 16×16 = 256 elements, as shown in Figs. 4.13 (a) and 4.13 (b). A standard gain horn LB-12-15-A from A-INFO is placed at the focal point with -10 dB aperture edge illumination. The focal length is 43.4 mm. The gain

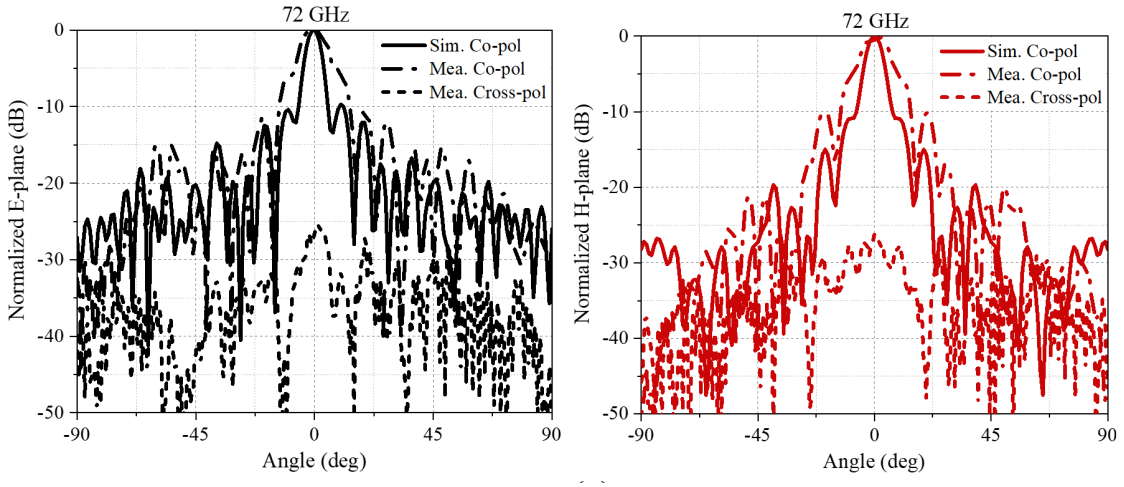


(a)

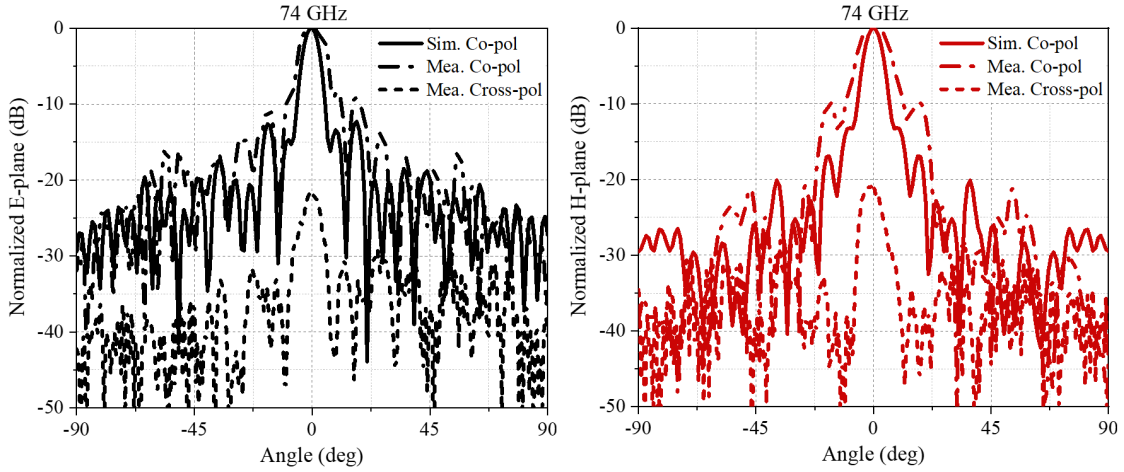


(b)

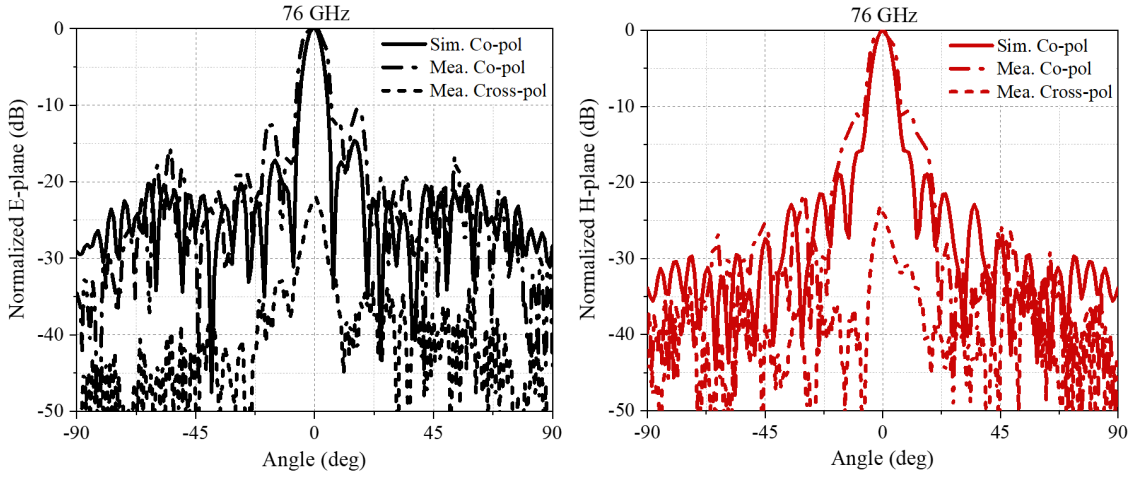


(c)

Figure 4.16: Measured and simulated realized gain patterns of the wideband conformal transmitarray antenna in E and H planes at different frequencies. (a) 72 GHz. (b) 74 GHz. (c) 76 GHz. (d) 78 GHz. (e) 80 GHz. (f) 82 GHz. (g) 84 GHz. (h) 86 GHz.

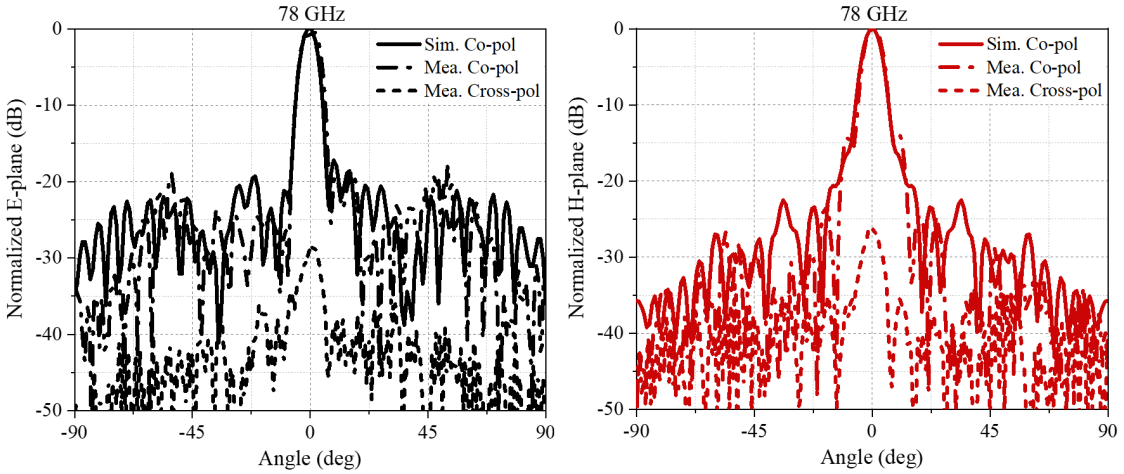


(d)

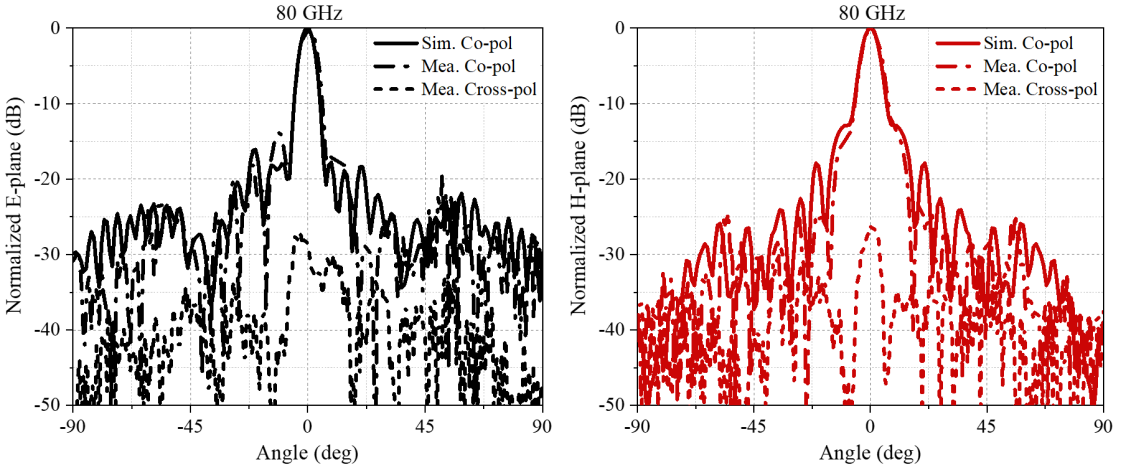


(e)

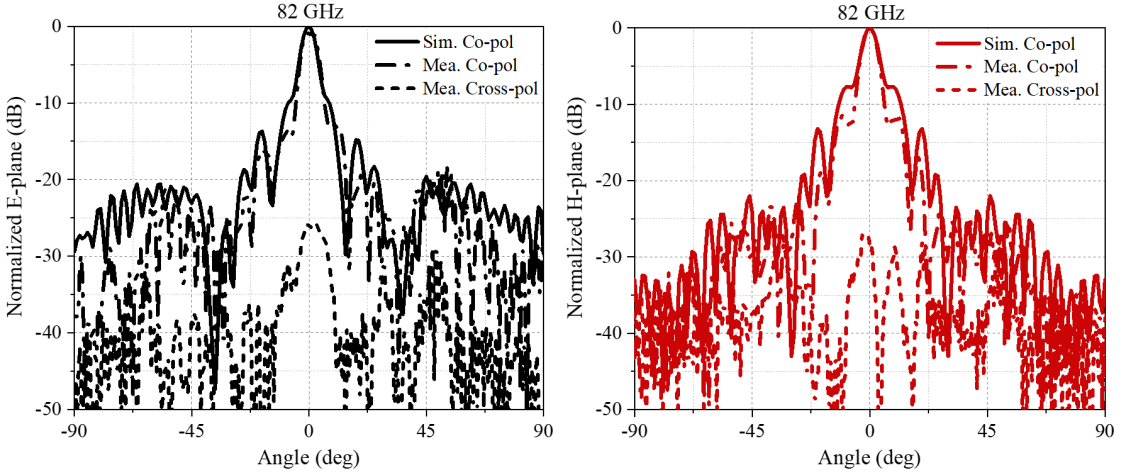


(f)

Figure 4.16: Measured and simulated realized gain patterns of the wideband conformal transmitarray antenna in E and H planes at different frequencies. (a) 72 GHz. (b) 74 GHz. (c) 76 GHz. (d) 78 GHz. (e) 80 GHz. (f) 82 GHz. (g) 84 GHz. (h) 86 GHz.

of LB-12-15-A from the data sheet is 15.65 dB at 78 GHz. The phase compensations of the transmitarray are achieved by varying the scale factor $k$ of each element on the aperture. Due to the conformal transmitarray symmetrical to both x- and y-axises, the scale factors $k$ and simulated transmission coefficients of the elements on a quarter of whole conformal transmitarray at 78 GHz are shown in Fig. 4.13 (c) and Table 4.2.

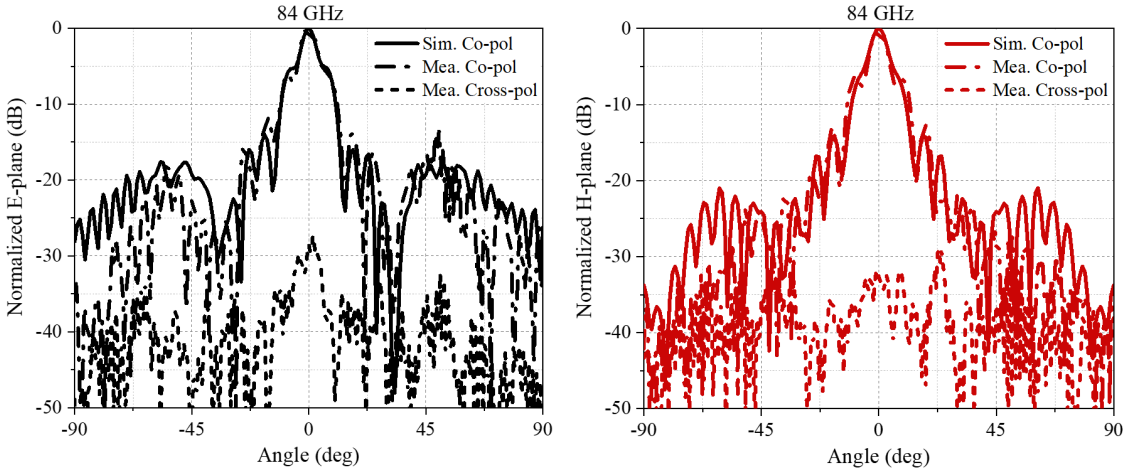


(g)

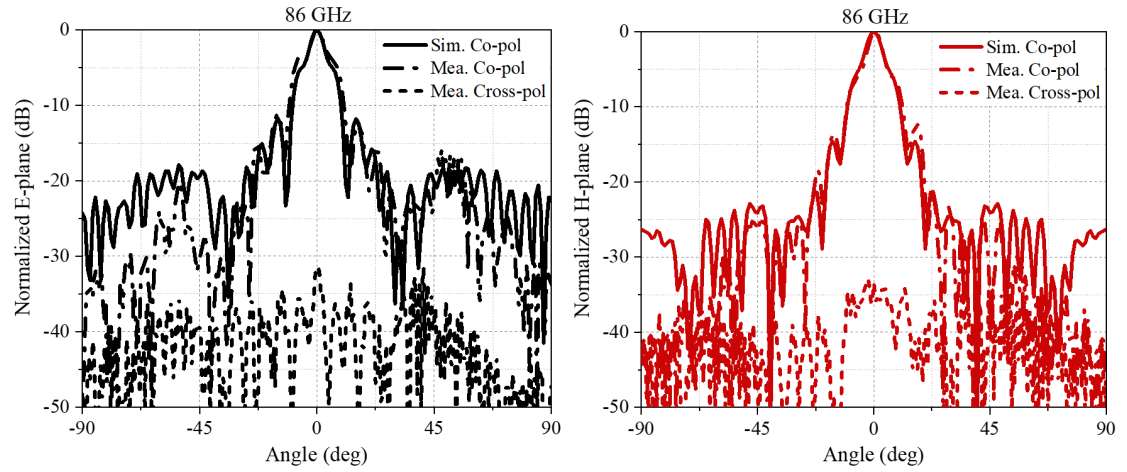


(h)

Figure 4.16: Measured and simulated realized gain patterns of the wideband conformal transmitarray antenna in E and H planes at different frequencies. (a) 72 GHz. (b) 74 GHz. (c) 76 GHz. (d) 78 GHz. (e) 80 GHz. (f) 82 GHz. (g) 84 GHz. (h) 86 GHz.

It can be seen from Table 4.2 that the transmission losses of all elements of the conformal transmitarray are less than 0.9 dB which is beneficial to achieve a high-efficiency transmitarray, and continuous transmission phase compensation of 360° is achieved to

reduce the phase errors of the array.

A planar transmitarray is fabricated and bent to adapt the cylindrical prototype as shown in Fig. 4.13. The fabricated prototype of wideband conformal transmitarray antenna is shown in Fig. 4.14. The far-field radiation pattens of the transmitarray are measured using a compact range antenna measurement system at University of Technology Sydney, Australia.

### 4.3.2 Numerical and Experimental Results of the Wideband Conformal Transmitarray Antenna

Table 4.3: Comparison Between Reported Transmitarray Antennas

| Ref | [37] | [39] | [46] | [47] | [71] | This work |
|---|---|---|---|---|---|---|
| Configuration | 3-layer | 2-layer | 2-layer | 2-layer | 2-layer with 4 vias | 2-layer |
| Conformality | Conformal | Conformal | Planar | Planar | Planar | Conformal |
| Frequency | 25.0 GHz | 10.0 GHz | 9.3 GHz | 26.2 GHz | 21.0 GHz | 78.5 GHz |
| Gain | 19.6 dBi | 20.6 dBi | 19.6 dBi | 30.7 dBi | 30.0 dBi | 26.6 dBi |
| Aperture eff. | 25.1 % | 47.0 % | 27.8 % | 42.2 % | 40.0 % | 35.9 % |
| 3-dB BW | 6.7 % | 3.7 % | 4.3 % | 15.7 % | 9.6 %* | 20.4 % |

As shown in Fig. 4.15, the measured and simulated input reflection coefficients of the antenna are below -10 dB from 70 GHz to 87 GHz. The measured and simulated normalized realized gain patterns of the wideband conformal transmitarray antenna in E plane and H plane at different frequencies are plotted in Fig. 4.16. It can be seen that all side lobe levels (SLLs) are greater than 10 dB from 72 GHz to 86 GHz. The measured and simulated realized gains and aperture efficiencies of the wideband conformal transmitarray antenna versus frequencies from 70 GHz to 87 GHz are shown in Fig. 4.17. The measured results shown a peak realized gain of 26.6 dB with an aperture efficiency of 35.9 % at 78.5 GHz. The measured 3-dB bandwidth is 20.4 % from 71 GHz to 87 GHz, fully covering the proposed E-band spectrum from 71 to 86 GHz. The phase error on the aperture and the transmission loss of the element are two main factors for decreasing aperture efficiency. Therefore, there are two methods to increase the aperture efficiency of the

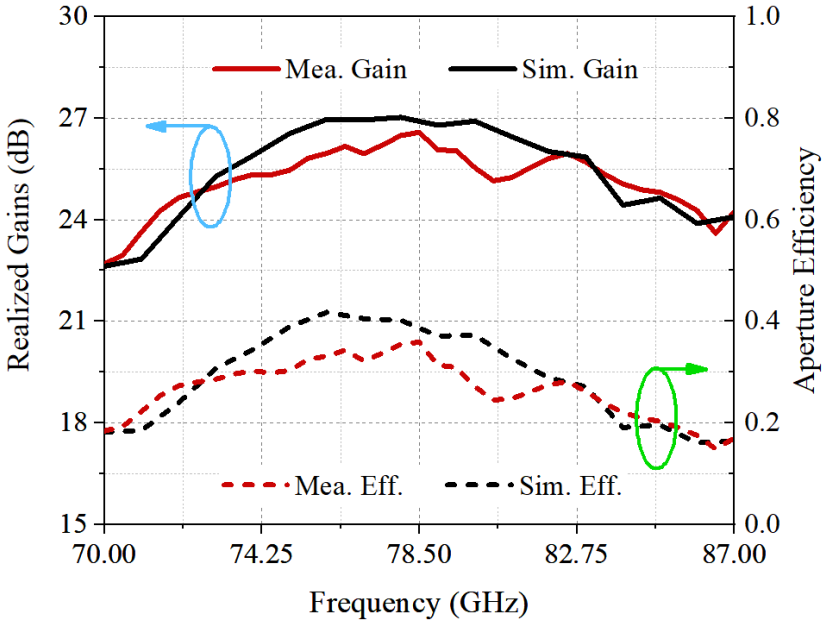


Figure 4.17: Measured and simulated realized gains and aperture efficiencies of the wideband conformal transmitarray antenna versus frequencies.

wideband conformal transmitarray: reducing the transmission loss of the transmitarray element and reducing the element size to reduce the phase error on the aperture.

A comparison between this work and other reported conformal, dual-layer or wideband transmitarrays is presented in Table 4.3. It can be found that the proposed work employs simple array elements, i.e. 2-layer Huygens configuration without any metallic vias, to achieve a wider bandwidth for conformal applications in E-band high data rate wireless communication systems.

## 4.4 Summary

A wideband conformal transmitarray employing dual-layer tightly coupled Huygens elements is proposed for E-band high data rate communication in the paper. The element consists of five pairs of partly overlapped metallic striplines with different lengths printed on two layers of a dielectric substrate, which can provide tightly coupled Huygens resonances with nearly total transmission and full transmission phase coverage in a wide

bandwidth. To validate the design concept, a cylindrically conformal transmitarray at 78 GHz is designed, fabricated and measured. Continuous phase compensation of 360° is achieved by tuning the lengths of the strips, reducing phase errors of the array architecture. Good agreement between the measured and simulated results is found, showing a peak measured realized gain of 26.6 dBi with an aperture efficiency of 35.9 % at 78.5 GHz and measured 3-dB bandwidth of 20.4 % from 71 to 87 GHz, fully covering the proposed E-band spectrum from 71 to 86 GHz.

# 5

# Reconfigurable transmitarray

## 5.1 Introduction

Space-fed arrays, i.e., reflectarrays and transmitarrays, have become more and more attractive since they are able to achieve high gains for many applications, e.g., satellite communications, imaging systems and automotive radars. The spatial feeding networks employed by reflectarrays and transmitarrays have lower loss and cost compared with transmission line based feeding networks employed by phased arrays. The beam scanning of the space-fed arrays can be realized by independently controlling the reflection or transmission phases of the elements on the apertures using PIN didoes, MEMS switches or varactor didoes.

According to the above literature review in Section 2.3, it can be found that most of the currently reported reconfigurable transmitarray elements have more than three metallic layers with several metallic vias. Such configurations may lead to complex fabrication and package processes, which could affect the performance of transmitarrays. For example, for a 2-bit reconfigurable transmitarray using 6-layer elements with 7 vias at 29 GHz reported in [55], 51 elements were found faulty, which could be due to the fabrication inaccuracies. Hence, it is highly desirable to design dual-layer reconfigurable transmitarray elements without metallic vias, which can also facilitate the design of large-size arrays at higher frequencies.

It should be noted that there are some published dual-layer transmitarray elements using rotated split-ring elements [43], malta-cross elements with metallic vias [41], or patch elements with metallic vias [42]. In those structures, however, the metallic vias increase the element complexity. Furthermore, some dual-layer Huygens elements are reported for transmitarrays [39, 44–47]. One particular advantage of Huygens elements is that a nearly total transmission, zero reflection and full phase coverage can be achieved when the electric and magnetic responses are balanced. This can lead to high efficiency transmitarrays. It should be noted that the above-mentioned dual-layer transmitarray elements are all passive ones and there is no electronic control of their transmission phases. Actually, electronic beam-scanning transmitarrays based on dual-layer reconfigurable elements have been rarely reported.

In this chapter, a Ku-band electronic 2-D beam scanning transmitarray employing a new reconfigurable dual-layer Huygens element is developed. The Huygens element consists of two metallic crosses printed on two layers of a dielectric substrate, respectively. A 1-bit phase compensation with low transmission loss is achieved by controlling two PIN diodes integrated on the element. Compared with many other reconfigurable transmitarray elements using multi-layer structures with metallic vias, the proposed reconfigurable Huygens element has much simpler configuration and biasing network, and it is not affected by multi-layer alignment errors. This particularly facilitates large aperture array development at higher frequencies. To validate the design concept, a transmitarray pro-

totype with the proposed element at 13 GHz is designed and fabricated. The measured results agree well with the simulated ones, showing 2-D scanning beams within ±50° in E-plane and ±40° in H-plane. A maximum realized gain of 18.4 dBi is obtained.

## 5.2 1-Bit Reconfigurable Dual-Layer Huygens Element

In order to electronically control the beams of a transmitarray for 2-D beam scanning, the transmission phase of each transmitarray element should be controlled independently. In this section, a 1-bit reconfigurable dual-layer Huygens element is developed using PIN diodes.

### 5.2.1 Dual-Layer Huygens Element Design

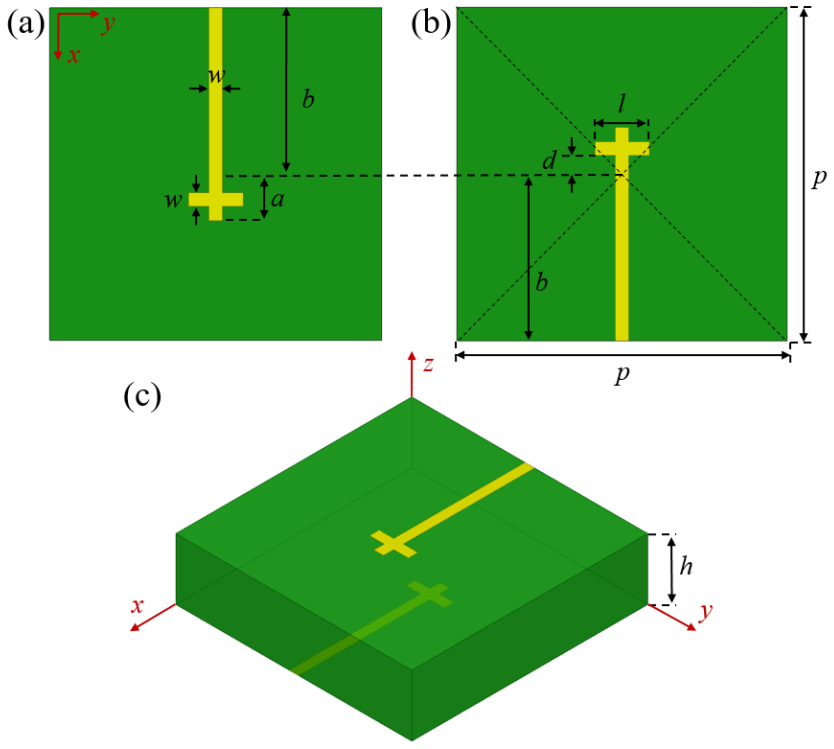


Figure 5.1: Configuration of the dual-layer Huygens element. (a) Top view. (b) Bottom view. (c) 3D view.

The configuration of the proposed dual-layer Huygens element is demonstrated in Fig. 5.1. It consists of two metallic crosses printed on two layers of a dielectric substrate (Rogers RT/duroid 5880, $\varepsilon_r$ = 2.2, tan$\delta$ = 0.009, $h$ = 3.175 mm). These two metallic crosses are symmetric to x-axis. The lengths of the total metallic strip and the overlapped part of the strips along x-axis on each layer are ($a$+$b$) and 2$a$, respectively. The other parameters are $p$ = 12.24 mm, $a$ = 1.71 mm, $b$ = 6.12 mm, $w$ = 0.49 mm, $d$ = 0.69 mm and $l$ = 2 mm.

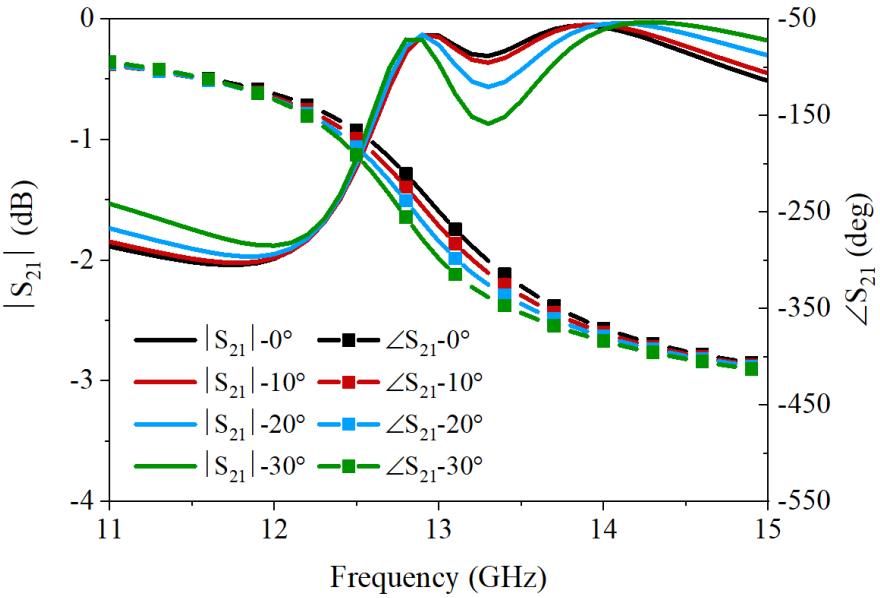


Figure 5.2: Transmission coefficients of the dual-layer Huygens element under the incidence waves with different angles.

The element is simulated using master/slave boundary conditions and Floquet ports of 3D EM simulation software HFSS. An incident x-polarized plane wave is used to illuminate the element. The simulated transmission coefficients of the dual-layer Huygens element under the incidence waves with different angles are shown in Fig. 5.2. It is seen that the transmission loss is less than 2.1 dB and the phase variation range is 320° from 11 to 15 GHz for the element under the incidence waves with angles from 0° to 30°. There are two peaks of transmission magnitude reaching -0.17 dB at 13.0 GHz and -0.08 dB at 13.8 GHz, respectively. It can also be seen from Fig. 5.2 that the element has stable transmission performance under the incidence waves with different angles, which is beneficial to a transmitarray design.

Based on the Huygens theory, a Huygens resonance can be excited with a total transmission when the orthogonally induced electric and magnetic currents are in-phase [72, 73]. The electric and magnetic surface currents can be characterized by the electric surface admittance ($Y_{es}$) and magnetic surface impedance ($Z_{ms}$) corresponding to a specific polarization of incidence EM wave. The electric admittance and magnetic impedance of the Huygens surface can be extracted from the reflection and transmission coefficients as follows [74]

$$Y_{es} = \frac{2(1-T-R)}{\eta(1+T+R)} \tag{5.1a}$$

$$Z_{ms} = \frac{2\eta(1-T+R)}{1+T-R} \tag{5.1b}$$

where $\eta$ is the wave impedance of free space, $T$ is the transmission coefficient and $R$ is the reflection coefficient. It has been demonstrated that a total transmission can be achieved if the normalized electric surface admittance and magnetic surface impedance are purely imaginary and equal as given below

$$Y_{es}\eta = \frac{Z_{ms}}{\eta} \tag{5.2}$$

Based on (5.1a) and (5.1b), the simulated $Y_{es}\eta$ and $Z_{ms}/\eta$ of the dual-layer Huygens element at two transmission peaks are $Y_{es}\eta = 2.87 - j0.03$ and $Z_{ms}/\eta = 1.53 - j0.03$ at 13.0 GHz; $Y_{es}\eta = 0.01 - j1.95$ and $Z_{ms}/\eta = -j1.95$ at 13.8 GHz. It shows that the imaginary parts of the normalized electric surface admittance and magnetic surface impedance are equal and their real parts are near zero at 13.0 GHz and 13.8 GHz. Thus, at these two frequency points, quasi Huygens resonances are achieved with very small transmission loss.

When the element is illuminated by an x-polarized wave, currents will be induced on the metallic crosses on both layers of the dielectric substrate. The simulated surface currents of the dual-layer Huygens element at 13 GHz are shown in Fig. 5.3. The currents

on top and bottom substrate layers are named as $i_{up}$ and $i_{low}$, respectively. As shown in Fig. 5.3, the directions of $i_{up}$ and $i_{low}$ are opposite in the first and third quarters of one time period T, providing a current loop in the overlapped areas of the two strips along x-axis on the two layers of the substrate. This current loop can be equivalent to a magnetic current with a time delay of T/4 [73, 74]. In the second and fourth quarters of T, the directions of $i_{up}$ and $i_{low}$ are the same leading to an electric current. Thus, the orthogonally induced electric and magnetic currents appear simultaneously, exciting a Huygens resonance in the element.

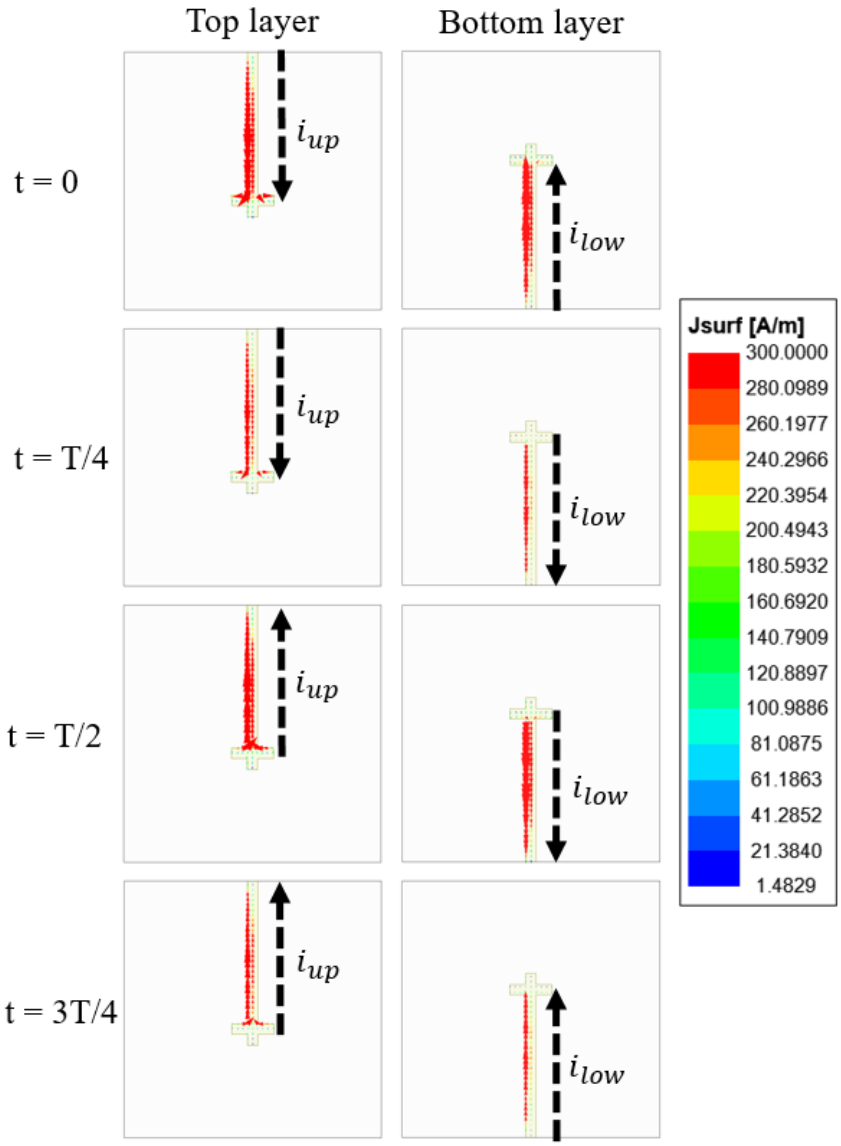


Figure 5.3: Simulated current distributions on top and bottom layers of the dual-layer Huygens element.

### 5.2.2 Parametric Study

A few parameters are found to play important roles in generating the Huygens resonance. A parametric study is conducted. When one parameter is varied, the others remain stable. The transmission coefficients of the dual-layer Huygens element with different values of parameter $a$ are shown in Fig. 5.4.

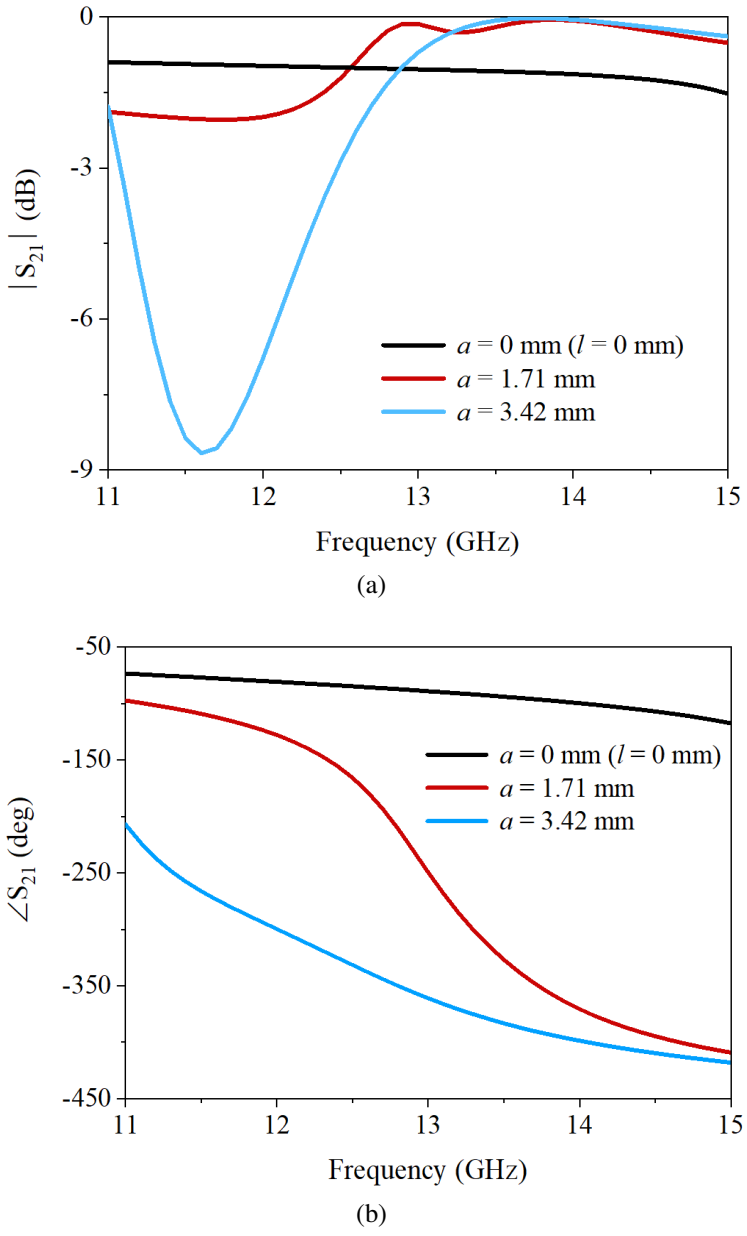


Figure 5.4: Transmission coefficients of the dual-layer Huygens element with different values of parameter $a$. (a) Magnitudes. (b) Phases.

It is noticed that the transmission loss and the phase range are dependent by $a$. This means the overlapped part of metallic strips along x-axis affects significantly the Huygens resonance. When $a$ = 0 (no overlapped part) or $a$ = 3.42 mm (too long overlapped part), the Huygens resonance cannot be excited as the phase coverage is very small or/and the transmission loss is very high in the band.

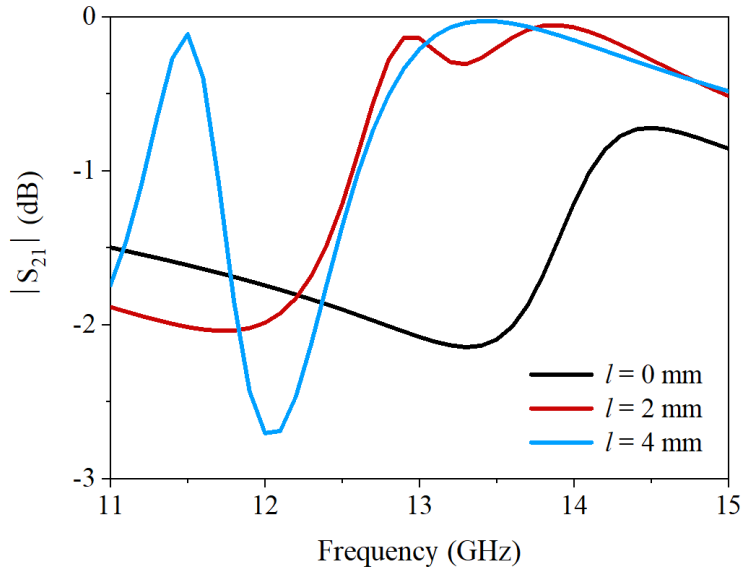


(a)

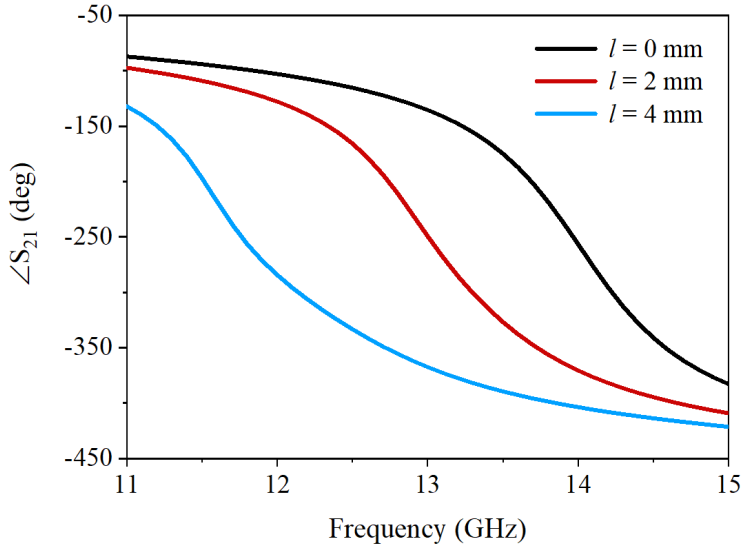


(b)

Figure 5.5: Transmission coefficients of the dual-layer Huygens element with different values of parameter $l$. (a) Magnitudes. (b) Phases.

The transmission coefficients of the element with different values of parameter $l$ are

shown in Fig. 5.5. It can be found that the operating frequency and transmission loss of the element are affected by $l$, thus low transmission loss and desired operating frequency can be achieved by tuning $l$.

The transmission magnitudes of the element for different thickness $h$ of the dielectric substrate are shown in Fig. 5.6. It is seen that the transmission loss of the element is significantly affected by $h$, which means the thickness of the dielectric substrate affects significantly the Huygens resonance.

Overall, the Huygens resonance depends on the induced current loop in relation to two parameters $a$ and $h$. In this work, the thickness of the element is chosen as 3.175mm.

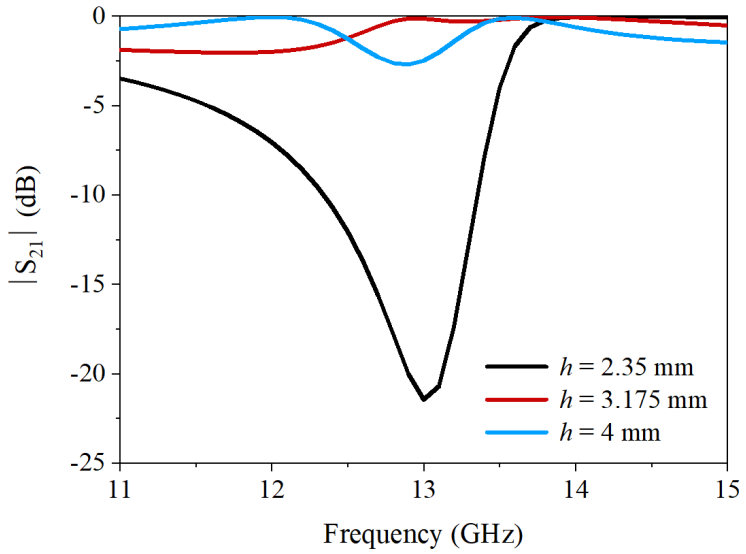


Figure 5.6: Transmission magnitudes of the dual-layer Huygens element with different thickness $h$ of the dielectric substrate.

### 5.2.3 PIN Diodes: Experimental Characterization and Modeling

To electronically control the transmission phase of the dual-layer Huygens element, the surface-mount PIN diodes MA4AGP907 (switching speed: 2 ns at 10 GHz) fabricated by M/A-Com are employed. A PIN diode MA4AGP907 has been mounted in series on a microstrip line of a fixture shown in Fig. 5.7 (a) and measured by a vector network analyzer (VNA) from 100 MHz to 20 GHz. The system is calibrated using the standard

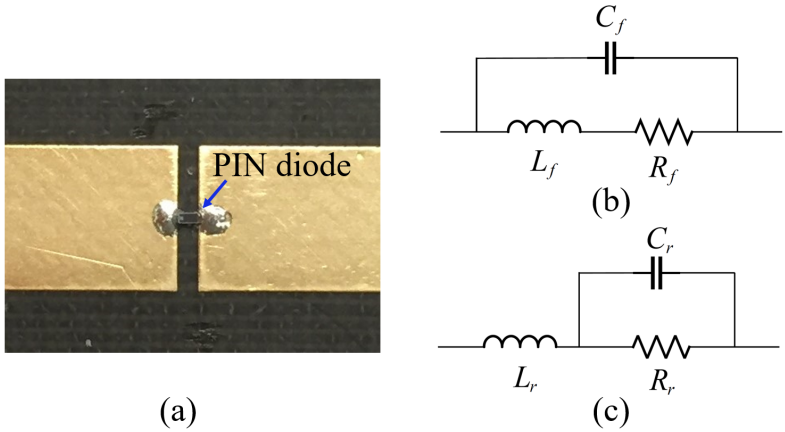


Figure 5.7: (a) Fabricated fixture for the experimental characterization of the PIN diode. Equivalent models of the PIN diode under (b) forward bias; (c) reverse bias.

short-open-load-thru (SOLT) calibration of the VNA firstly and a multiline TRL calibration [75] secondly to shift the reference planes to an appropriate place on the microstrip lines of the fixture. The *S*-parameters of the fixture are written as

$$\mathbf{S} = \begin{bmatrix} S_{11} & S_{12} & S_{13} \\ S_{21} & S_{22} & S_{23} \\ S_{31} & S_{32} & S_{33} \end{bmatrix} \tag{5.1}$$

where the first 2 ports are connected to the reference planes obtained by TRL calibration, and the third port is connected to the diode. Then the *S*-parameters of the fixture embedded with the diode are given by [76]:

$$\mathbf{S_m} = \begin{bmatrix} S_{11} & S_{12} \\ S_{21} & S_{22} \end{bmatrix} - \begin{bmatrix} S_{13} \\ S_{23} \end{bmatrix} (S_{33} - \mathbf{X}^{-1})^{-1} \begin{bmatrix} S_{31} & S_{32} \end{bmatrix} \tag{5.2}$$

where **X**, **S** and $\mathbf{S_m}$ denote the *S*-parameters of the diode, the fixture and the fixture embedded with the diode, respectively. Besides, $\mathbf{S_m}$ can be obtained after TRL calibration, and **S** can be obtained by EM simulation.

As a result, the diode can be de-embedded by (5.2). To minimize the inconsistency effects of the PIN diode, three PIN diodes MA4AGP907 were measured under forward bias ($I_f$ = 10 mA) and reverse bias ($V_r$ = -5 V). The de-embedded results of the didoes

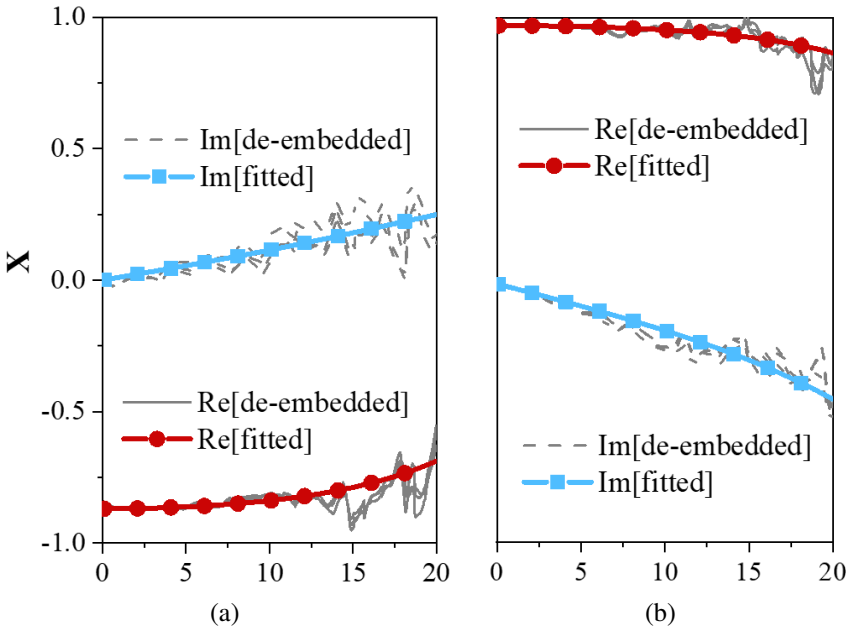


Figure 5.8: De-embedded and fitted results of the PIN diode under (a) forward bias; (b) reverse bias.

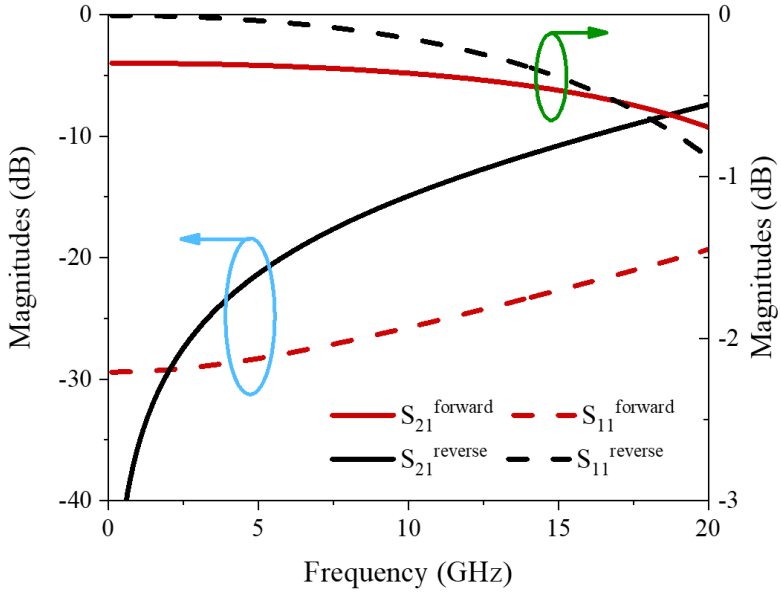


Figure 5.9: *S*-parameters of the equivalent circuits of the PIN diode.

under forward bias and reverse bias from 100 MHz to 20 GHz are shown in Figs. 5.8 (a) and 5.8 (b), respectively. The de-embedded results are fitted to two commonly used equivalent circuit models of a PIN diode shown in Figs. 5.7 (b) and 5.7 (c), and the extracted parameters are as follows: $R_f$ = 3.5 Ω, $L_f$ = 0.055 nH, $C_f$ = 0.42 pF, $R_r$ = 200 kΩ, $L_r$ = 0.66 nH, $C_r$ = 0.027 pF. The *S*-parameters of the extracted equivalent circuit

models of the PIN diode under forward bias and reverse bias from 100 MHz to 20 GHz are shown in Fig. 5.9.

### 5.2.4 Reconfigurable Dual-Layer Huygens Element with PIN Diodes

In order to electronically control the radiated beams of a transmitarray for 2-D beam scanning, the transmission phase of each transmitarray element should be controlled independently. As illustrated in Fig. 5.10, a reconfigurable Huygens element is developed based on the dual-layer Huygens element presented in 5.2.1. It is printed on two layers of the same Rogers RT/duroid 5880 dielectric substrate.

Two PIN diodes are integrated in these two metallic crosses respectively to achieve 1-bit phase compensation. By using the extracted equivalent circuit models of the PIN diode, the dimensions of the reconfigurable element are changed slightly to achieve 1-bit phase change with a high transmission. The dimensions are as follows: $p$ = 12.24 mm, $a$ = 1.71 mm, $b$ = 6.12 mm, $w$ = 0.49 mm, $d$ = 0.77 mm, $l$ = 5.86 mm, $k$ = 0.35 mm, $w_b$ = 0.15 mm, $l_a$ = 1.51 mm, $l_d$ = 0.74 mm, $w_d$ = 0.35 mm, $l_i$ = 0.89 mm, $w_i$ = 0.46 mm.

As shown in Figs. 5.10 (a), 5.10 (b) and 5.10 (c), two biasing lines along y-axis are connected to the two ends of the metallic strip along x-axis on each layer of the substrate to control the diode, and an inductor is embedded in each biasing line to isolate the DC source of the control board from the RF signals. According to the current distributions of the dual-layer Huygens element shown in Fig. 5.3, these two PIN diodes are located at the places where the currents through the metallic crosses are small. In this way, the extra loss from the PIN didoes can be minimized.

These two PIN diodes on the element are switched on or off at the same time. The working states of the element are named as ON or OFF states when these two PIN diodes are under forward or reverse biasing voltages, respectively. For different working states, the resonant lengths of the element are different, leading to different transmission phases. By selecting appropriate parameter $k$ which is the positions of these two diodes, a 1-bit phase shift with a high transmission is achieved between ON and OFF states.

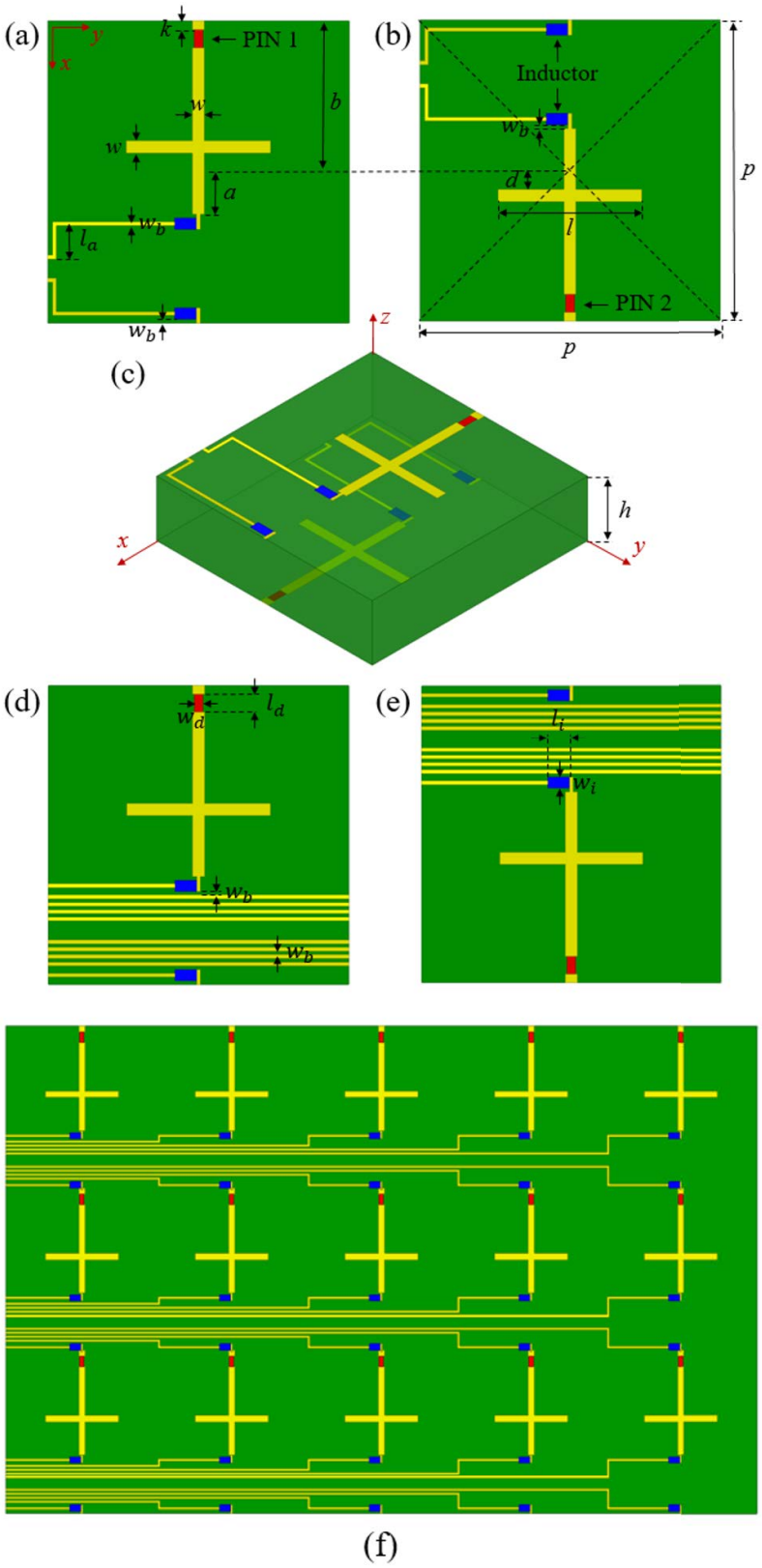


Figure 5.10: Configurations of the 1-bit reconfigurable dual-layer Huygens element. (a) Top view; (b) bottom view; (c) 3D view of the element with 4 biasing lines. (d) Top view; (e) bottom view of the element with 20 biasing lines. (f) Top view of a part of the whole transmitarray.

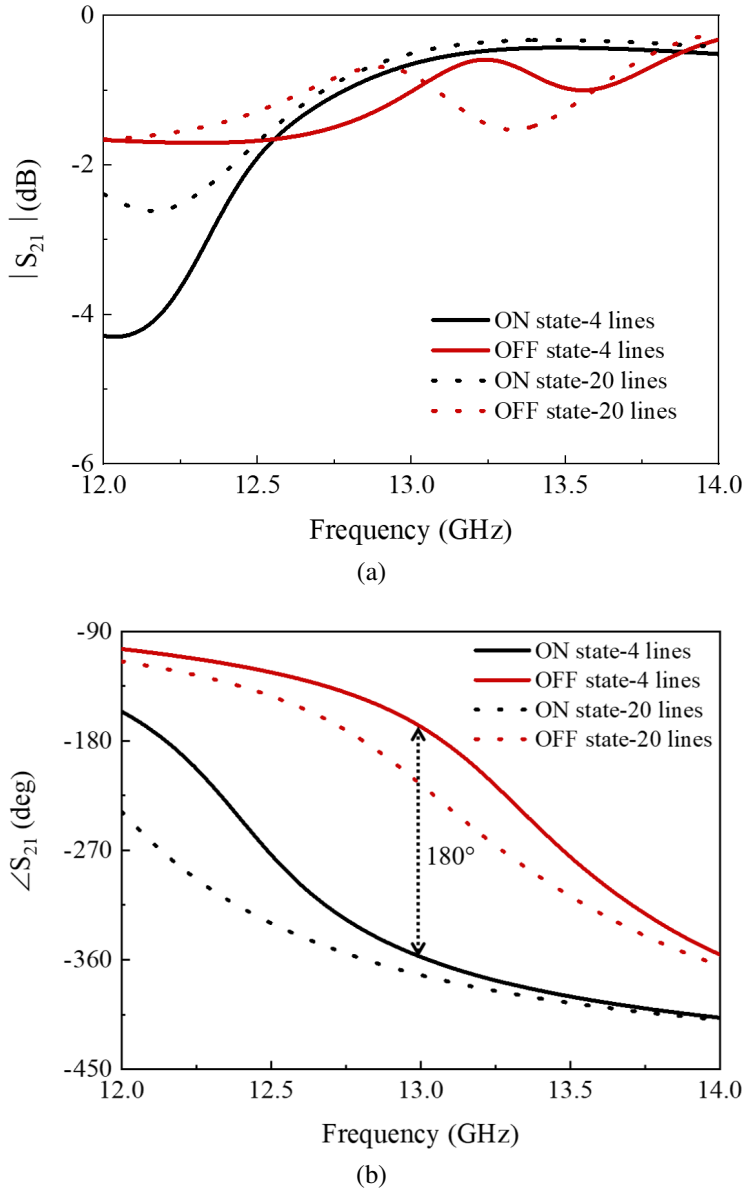


Figure 5.11: Transmission coefficients of the reconfigurable dual-layer Huygens element with 4 or 20 biasing lines under ON and OFF states. (a) Magnitudes. (b) Phases.

By utilizing periodic boundary conditions of the full-wave simulation software CST, the reconfigurable dual-layer Huygens element is simulated. The frequency response of the reconfigurable element with 4 biasing lines is shown in Table 5.1 and Fig. 5.11. It is seen that a phase difference of 180° between ON and OFF states of the element with 4 biasing lines is achieved at 13 GHz, and the transmission loss is lower than 1 dB at 13 GHz.

When employing the reconfigurable Huygens element to form a transmitarray, differ-

Table 5.1: Transmission Magnitudes and Phases of the 1-Bit Dual-Layer Huygens Element with Four Biasing Lines at 13 GHz

| State | PIN 1/PIN 2 | Magnitudes | Phase |
|---|---|---|---|
| ON | ON/ON | -0.65 dB | -353° |
| OFF | OFF/OFF | -1.02 dB | -173° |

ent number of biasing lines [Fig. 5.10 (f)], i.e., 4, 8, 12, 16, 20, will be printed on the elements located at different positions of the transmitarray. In order to evaluate the effects of the biasing lines on frequency responses of the element, the simulation of the reconfigurable elements with 20 biasing lines [Figs. 5.10 (d) and 5.10 (e)] under ON and OFF states have been performed as plotted in Fig. 5.11. It is seen that the transmission phase differences between two states and the transmission magnitudes of the elements with 4 and 20 biasing lines are nearly the same, which demonstrates that the DC biasing lines have little influence on the elements. This is mainly due to the fact that the biasing lines are perpendicular to the electric field polarization. Additionally, the biasing lines are very thin and embedded with inductors.

## 5.3 Reconfigurable Transmitarray Antenna

### 5.3.1 Reconfigurable Transmitarray Prototype Design

Due to the limited budget, a reconfigurable transmitarray with 10×10 elements is designed. The phase distributions on a planar transmitarray satisfy the following expression

$$\Delta\varphi_{m,n} = \frac{2\pi f}{c}\left(L_{m,n} - \vec{r}_{m,n}\cdot\hat{r}_0 - L_0\right) \tag{5.3}$$

where $\Delta\varphi_{m,n}$ is the phase difference between the geometric centers of the element $(m,n)$ and the transmitarray aperture, $m$ or $n$ is the number of the element along x- or y-axis, $f$ is the operating frequency, $c$ is the light speed in free space, $L_{m,n}$ is the distance between the phase center of the focal source and the geometric center of the element $(m,n)$ on the

aperture, $\vec{r}_{m,n}$ is the position vector of the element $(m, n)$, $\hat{r}_0$ is the desired direction of the radiated pencil beam, and $L_0$ is the focal length, as shown in Fig. 5.12 (a).

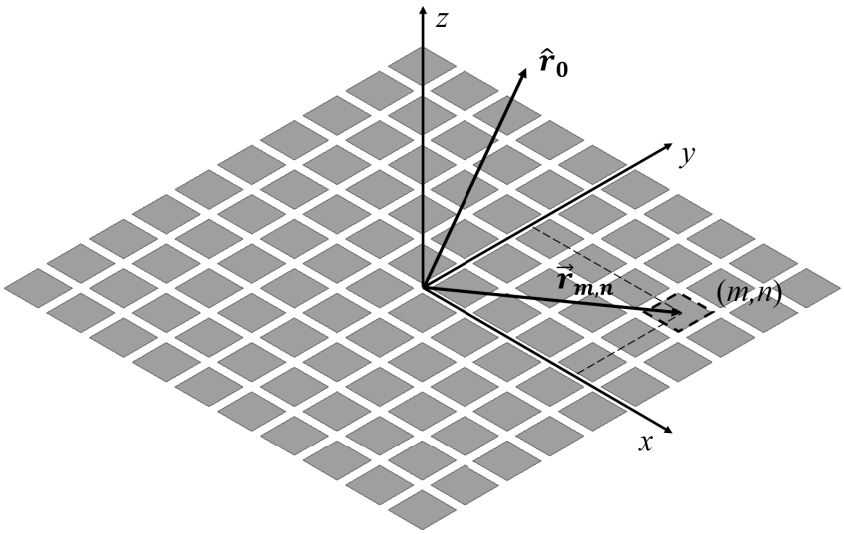


(a)

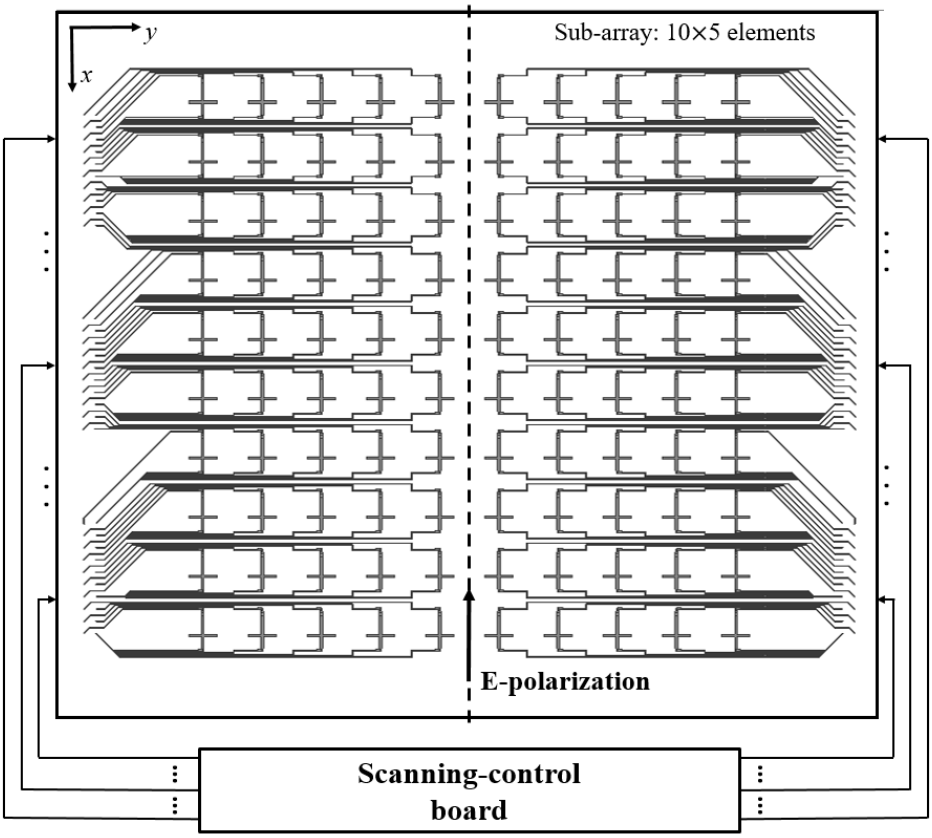


(b)

Figure 5.12: (a) Schematic diagram of the phase compensation for a radiated beam in a desired direction. (b) The 10×10 reconfigurable transmitarray with its scanning-control board.

Ideally, a continuous phase range of 360° is desired for each transmitarray element. As this is not feasible for a reconfigurable element with PIN diodes, a discrete phase compensation is utilized to approximate the ideal transmission phases with a resolution depending on the number of the available phase states in the element. The element described in 5.2.4 provides two phase states, thus the phase distributions $ph_{m,n}$ of the reconfigurable transmitarray are defined as follow

$$ph_{m,n} = \begin{cases} 0°, if -90° \leq \Delta\varphi_{m,n} < 90°; \\ 180°, otherwise. \end{cases} \tag{5.4}$$

The 10×10 reconfigurable transmitarray prototype based on the proposed element with a biasing network is shown in Fig. 5.12 (b), which can be seen as two 10×5-element sub-arrays symmetric to x-axis. The aperture size of the transmitarray is 122 mm × 122 mm. Because the two PIN diodes on any element work under the same state at the same time, the biasing lines of these two PIN diodes can be connected and controlled by one DC source path. Thus, the 10×10-element transmitarray contains 100 independent paths of DC sources to control the transmission phase of each element. These DC bias paths are controlled by a field-programmable gate array (FPGA) based controlling board.

The simulated scanning beams of the developed reconfigurable transmitarray in E- and H-planes are shown in Figs. 5.13 (a) and 5.13 (b), respectively. It is seen that the simulated gain decreases as the scanning angle increases. The scanning loss at 50° is 3.0 dB in E-plane and the scanning loss at 40° is 4.0 dB in H-plane. The SLLs of most scanned beams are better than -9 dB, only the SLL of the scanned beam at 40° in H-plane is -7 dB. There is the difference in beam scanning angles of E- and H-planes due to the single-polarization of the beam scanning transmitarray.

Please note that the biasing networks of the previous reported works are always realized with metallic vias. In this work, the biasing lines of the planar array are printed on the two sides of the substrate layer, and the biasing networks do not have any metallic vias, leading to a simple and low cost design. This layout would be beneficial for arrays

working at higher mm-wave bands.

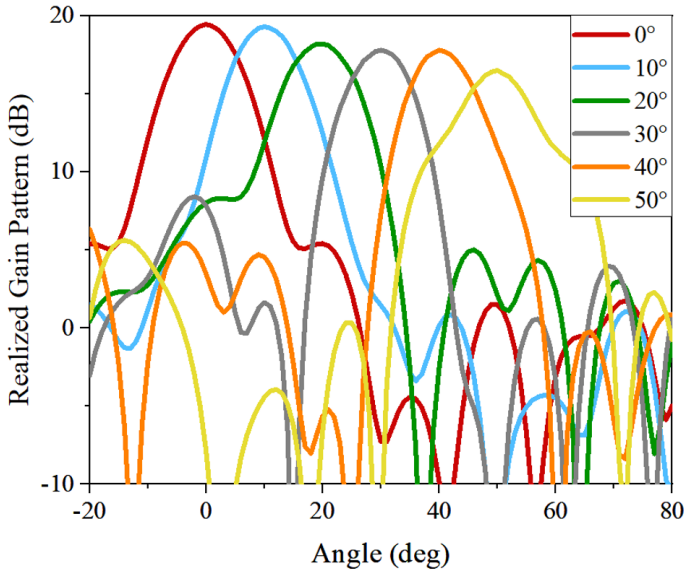


(a)

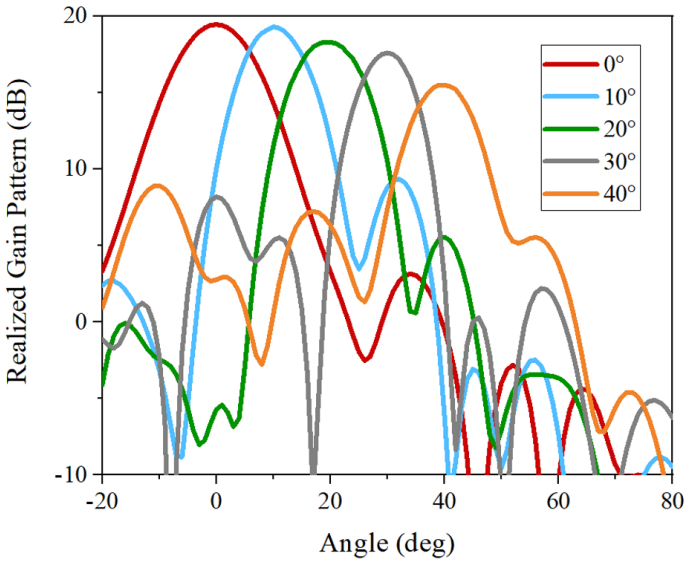


(b)

Figure 5.13: Simulated radiation patterns for different scan angles at 13 GHz in (a) E-plane and in (b) H-plane.

### 5.3.2 Fabricated Prototype and Experimental Implementation

The fabricated 100-element reconfigurable transmitarray is shown in Fig. 5.14 (a), which contains 200 PIN diodes and 400 inductors. The experimental setup is shown in Fig. 5.14 (b). A linearly-polarized standard gain horn antenna LB-75-10- from A-INFO

with a 12 dBi gain at 13 GHz is placed at the focal point with a -10 dB aperture edge illumination. The focal length is 91 mm, and the F/D ratio is 0.74.

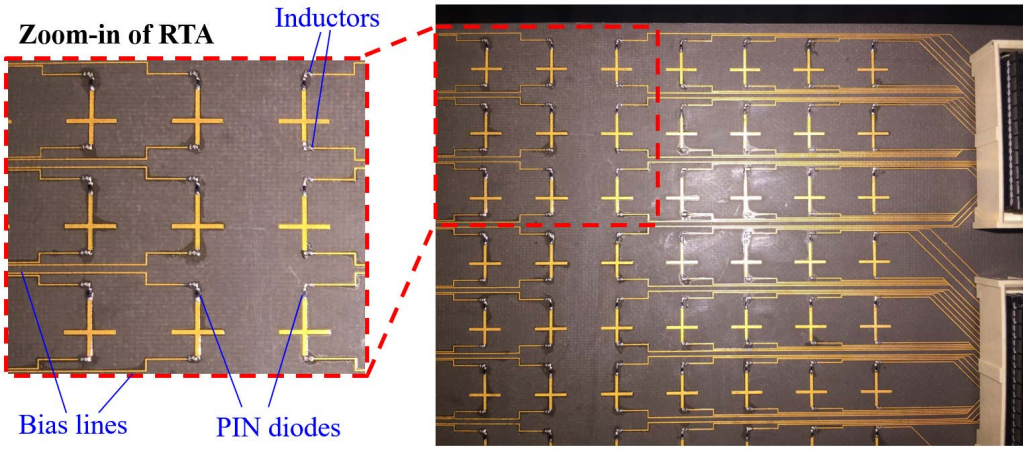


(a)

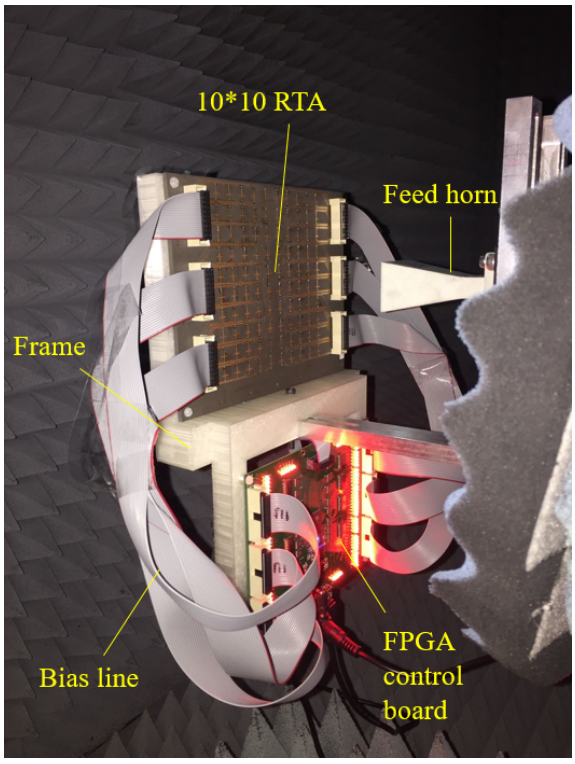


(b)

Figure 5.14: Photographs of (a) the fabricated reconfigurable transmitarray antenna (RTA) prototype and (b) the experimental setup of the RTA mounted in the anechoic chamber.

The FPGA control board is fixed below the reconfigurable transmitarray by a supporting frame. The FPGA control board contains 100 DC biasing paths which drive the

whole 10×10 elements with a 10 mA bias current or -5 V bias voltage per element. 100 LED lights are connected in series with the 100 DC biasing paths, respectively, in order to show the working status of the transmitarray intuitively. Six insulation-displacement contact (IDC) cables are used to connect the DC power supply from the FPGA control board to the diodes on the transmitarray. By using a digital I/O USB module, the control signals for 2-D beam scanning are provided to the FPGA control board from the computer.

The far-field radiation pattens of the electronically reconfigurable transmitarray antenna are measured using a Microwave Vision Group (MVG) compact range antenna measurement system located at University of Technology Sydney, Ultimo, Australia.

### 5.3.3 Numerical and Experimental Results of the Reconfigurable Transmitarray Antenna

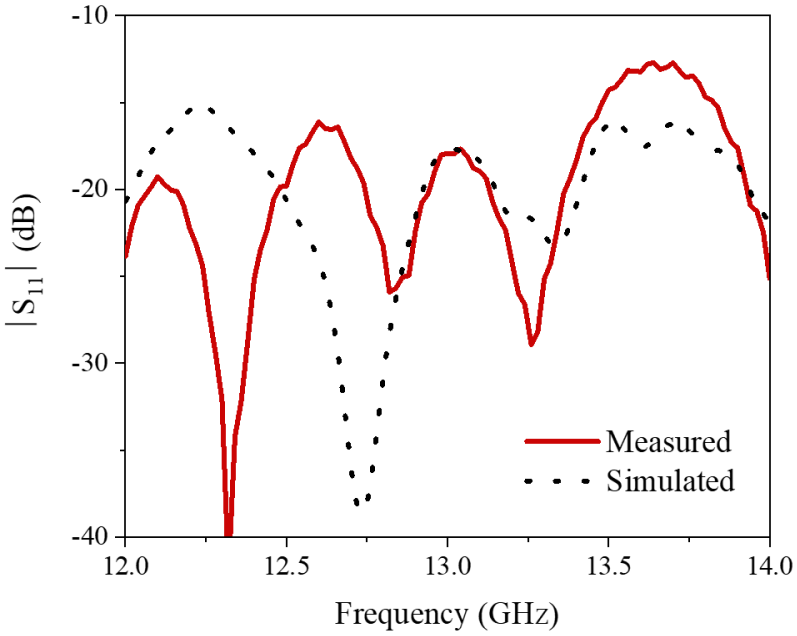


Figure 5.15: Measured and simulated input reflection magnitudes of the transmitarray radiating towards boresight.

As shown in Fig. 5.15, the input reflection coefficients for the boresight radiation pattern of the reconfigurable transmitarray are below -10 dB from 12 GHz to 14 GHz.

The input reflection coefficients for other beam scanning angles are also all below -10 dB, which are not shown here for brevity.

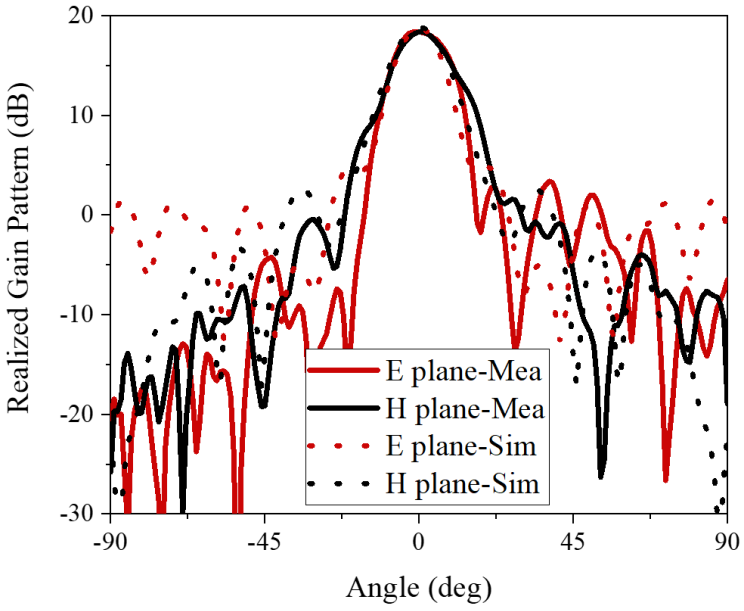


(a)

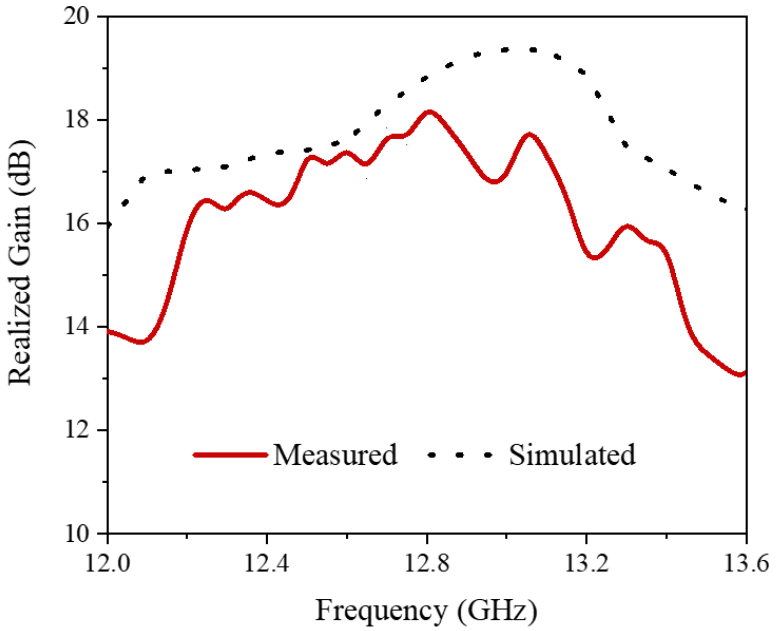


(b)

Figure 5.16: (a) Measured and simulated boresight radiation patterns in E and H planes at 12.8 GHz. (b) Measured and simulated realized gains in boresight direction versus frequencies.

The measured and simulated boresight radiation patterns of the transmitarray in E-

plane (xoz) and H-plane (yoz) at 12.8 GHz are shown in Fig. 5.16 (a). Good agreement between the simulated and measured results is observed. The measured SSL is below -15 dB in both planes. The measured and simulated realized gains in boresight direction versus frequencies are shown in Fig. 5.16 (b). The measured and simulated maximum gains are 18.4 dBi at 12.8 GHz and 19.5 dBi at 13 GHz, respectively. The measured aperture efficiency is 20.2 %.

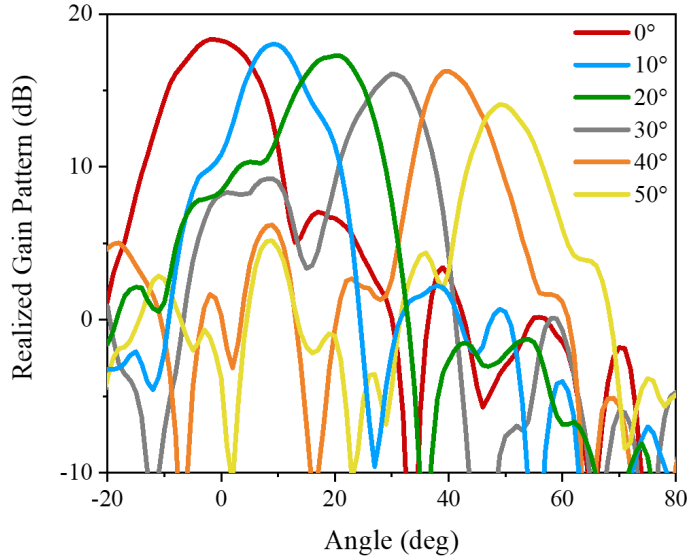


Figure 5.17: Measured radiation patterns for different scanning angles at 12.8 GHz in (a) E plane and (b) H plane.

There is a frequency shift of 0.2 GHz and a gain difference of 1.1 dB between the measured and simulated peak gains at boresight direction. This can be due to the following reasons. Firstly, there could be variations across the properties of the 200 PIN diodes from what we have measured and characterized. Secondly, there could be some fabrication errors during the implementation of the transmitarray and its mounting frame. The measured 3 dB gain bandwidth of the transmitarray is 1.2 GHz from 12.2 GHz to 13.4 GHz, which is 9.4 % at 12.8 GHz.

As shown in Figs. 5.17 (a) and 5.17 (b), the measured radiation patterns of the scanned beams at 12.8 GHz are from 0° to 50° in the E-plane and from 0° to 40° in the H-plane, respectively. The measured peak gains and SLLs of the scanned beams in E- and H-planes at 12.8 GHz and the simulated values at 13 GHz are shown in Tables 5.2 and 5.3. It is seen that the measured gain decreases as the scanning angle increases. The scanning loss at 50° is 4.2 dB in E-plane and the scanning loss at 40° is 3.4 dB in H-plane. The SLLs of most scanned beams are better than -9 dB, only the SLLs of the scanned beams at 30° in E-plane and 40° in H-plane are around -7 dB.

Table 5.2: Beam Scanning Performance of the Reconfigurable Transmitarray in E Plane

| Scan Angle | | 0° | 10° | 20° | 30° | 40° | 50° |
|---|---|---|---|---|---|---|---|
| Gain (dBi) | Mea. | 18.4 | 18.1 | 17.4 | 16.2 | 16.4 | 14.2 |
| | Sim. | 19.5 | 19.3 | 18.3 | 17.8 | 17.8 | 16.5 |
| SLL (dB) | Mea. | 11.4 | 15.9 | 15.3 | 7.0 | 10.2 | 9.1 |
| | Sim. | 14.0 | 13.2 | 9.9 | 9.3 | 9.5 | 9.3 |

Table 5.3: Beam Scanning Performance of the Reconfigurable Transmitarray in H Plane

| Scan Angle | | 0° | 10° | 20° | 30° | 40° |
|---|---|---|---|---|---|---|
| Gain (dBi) | Mea. | 18.4 | 18.1 | 17.5 | 16.1 | 15.0 |
| | Sim. | 19.5 | 19.3 | 18.3 | 17.6 | 15.5 |
| SLL (dB) | Mea. | 19.6 | 11.9 | 11.0 | 9.4 | 7.3 |
| | Sim. | 16.1 | 9.7 | 12.2 | 9.2 | 7.0 |

The measured cross-polarization radiation patterns for several scanning angles at 12.8

Table 5.4: Comparison Between the Reconfigurable Transmitarray Antennas

| Ref. | [50] | [52] | [53] | [55] | This work |
|---|---|---|---|---|---|
| Theory | Rx-Tx | Rx-Tx | Rx-Tx | Rx-Tx | Huygens |
| Layer No. | 4 | 4 | 4 | 6 | 2 |
| Via No. | 5 | 18 | 3 | 7 | None |
| Diode No. | 2 | 2 | 2 | 4 | 2 |
| Frequency | 9.8 GHz | 13.5 GHz | 12.5 GHz | 29.0 GHz | 12.8 GHz |
| Array size | 20×20 | 16×16 | 16×16 | 14×14 | 10×10 |
| Gain | 22.7 dBi | 21.4 dBi | 17.0 dBi | 19.8 dBi | 18.4 dBi |
| Aperture eff. | 16.0 % | 14.7 % | 14.0 % | 15.9 % | 20.2 % |
| 3-dB gain bandwidth | 15.8 % | 13.3 % | 9.6 % | 16.2 % | 9.4 % |
| Scanning angle and loss | 40° (2.8 dB) ×70° (7.6 dB) | 60° (3.6 dB) ×non shown | 50° (5.8 dB) ×50° (5.7 dB) | 60° (5.0 dB) ×60° (5.0 dB) | 50° (4.2 dB) ×40° (3.4 dB) |

GHz in E- and H-planes are shown in Fig. 5.18. It can be seen that the measured cross-polarized gain levels are all below 0 dB, which means they are at least 15 dB lower than the co-polarization. The measured cross-polarized gain levels for other scanning angles are all below 0 dB. They are not shown here for brevity.

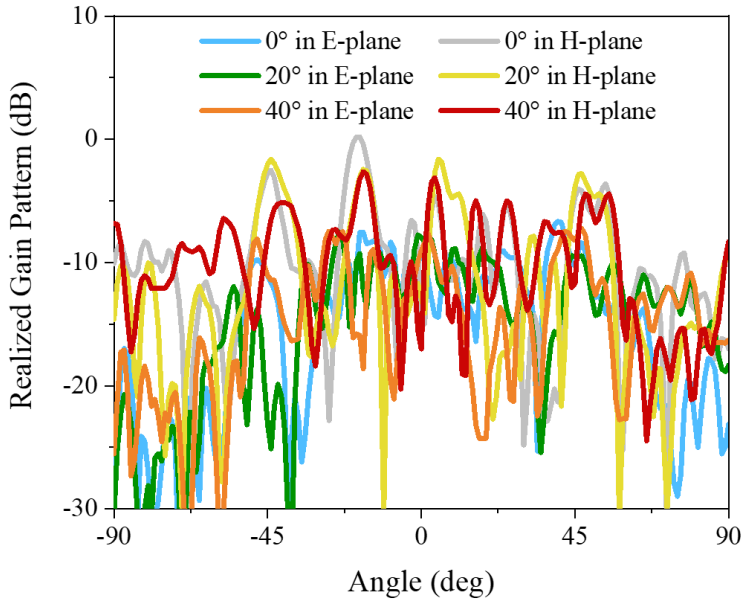


Figure 5.18: Measured cross-polarization radiation patterns for different scanning angles at 12.8 GHz in E and H planes.

A comparison between other reconfigurable transmitarrays and the developed one is presented in Table 5.4. It can be seen from the table that the proposed work employs much

simpler array elements, i.e. 2-layer Huygens configuration without any metallic vias. As a comparison, the other array elements have at least four metallic layers and many vias. Although the structure of the proposed element is simpler, the performance of the array is comparable to or even better than those of other arrays, e.g., the aperture efficiency of this work is 20.2 %.The proposed dual-layer reconfigurable Huygens element without metallic vias is particular suitable for larger-size beam scanning transmitarrays at higher frequency bands. If the aperture size of the reconfigurable transmitarray is larger, a better beam scanning performance with a larger beam scanning range, lower scanning losses and higher SLLs can be achieved.

## 5.4 Summary

A novel electronic beam scanning transmitarray employing dual-layer reconfigurable Huygens element is reported in this paper. The Huygens element is composed of two metallic crosses which enables a near non-reflection response. Moreover, the element can achieve a 1-bit phase compensation with low transmission loss by controlling two PIN diodes on the element. A reconfigurable transmitarray with a simple biasing network is designed and fabricated for the experimental verification. The measured maximum gain in the boresight direction is 18.4 dBi with an aperture efficiency of 20.2 %, and the 3-dB gain bandwidth is 9.4 %. The 2-D electronic beam scanning of $\pm 50^\circ$ in E plane and $\pm 40^\circ$ in H plane is achieved.

# 6

# Conclusions and Future Work

## 6.1 Conclusions

This thesis focused on the advancement of the transmitarrays associated with novel designs or methods to meet the demands for the future wireless systems. Firstly, the background of transmitarray antennas is briefly introduced. Motivated by challenges for current reported literature of transmitarrays, three transmitarray techniques are presented and investigated. The advances of the developed transmitarrays are summarized as follows:

To solve the tradeoff between high gain and low RCS properties, a low RCS transmitarray is developed using phase controllable AFST elements. The element consists of

asymmetrical resonators with resistors to obtain an absorption-transmission-absorption response. The transmission phase within the transmission band can be controlled by rotating the AFST elements, achieving a 1-bit phase change. Compared with a reference transmitarray, the radiation performance of the low-RCS one is almost unchanged, and there is a remarkable RCS reduction at the out-of-band frequencies for the low-RCS one. It has shown that the low-RCS transmitarray has achieved the RCS reduction under wide-angle impinging waves.

To develop a wideband conformal antenna with supporting high data rate and aerodynamic requirements with reduced alignment errors, a wideband conformal transmitarray employing dual-layer Huygens element is developed. The element consists of five pairs of partly overlapped metallic striplines with different lengths printed on two layers of a dielectric substrate, which can provide tightly coupled Huygens resonances with nearly total transmission and full transmission phase coverage in a wide bandwidth. Then a cylindrically conformal transmitarray at 78 GHz is designed, fabricated and measured. Continuous phase compensation of 360° is achieved by tuning the lengths of the strips, reducing phase errors of the array architecture. Good agreement between the measured and simulated results is found, showing a high measured aperture efficiency and measured 3-dB bandwidth fully covering the E-band spectrum.

To achieve good 2-D beam scanning with simple structure of reconfigurable transmitarrays, an electronic 2-D beam scanning transmitarray employing a new reconfigurable dual-layer Huygens element is developed in this paper. The Huygens element consists of two metallic crosses printed on two layers of a dielectric substrate respectively, which enables a near non-reflection Huygens resonance. A 1-bit phase compensation with low transmission loss is realized by controlling two PIN diodes on the element. Compared with many other reconfigurable transmitarray elements using multi-layer structures with metallic vias, the proposed reconfigurable Huygens element has much simpler configuration and biasing network, and it is not affected by multi-layer alignment errors. This particularly facilitates large aperture array development at higher frequencies. By employing dual-layer reconfigurable Huygens element, a novel electronic beam scanning

transmitarray is developed. Although the structure of the proposed element is simpler, the performance of the transmitarray is comparable to or even better than those of mostly reported transmitarrays.

## 6.2 Future Work

Several advanced transmitarray designs and methods have been developed in this thesis, and there are some interesting directions to work on in the future:

1. Based on the 1-bit reconfigurable transmitarray in Chapter 5, beam synthesis methods for multibeam and beam forming, can be studied.

2. In Chapter 5, a reconfigurable transmitarray at 12.8 GHz has been developed and implemented. For 5G and beyond wireless communication systems, reconfigurable transmitarrays at millimeter-wave and higher frequency bands will be a research focus with great application values.

3. In Chapter 5, a 1-bit reconfigurable transmitarray for 2-D beam scanning has been realized. However, compared with 1-bit reconfigurable transmitarrays, more-bit reconfigurable transmitarrays are more attractive with less phase errors resulting in better beam scanning performance.

4. Low-RCS reconfigurable transmitarrays can significantly reduce the RCS of the arrays with electronic 2-D beam scanning characteristics, which is very valuable for antenna stealth and communication security in future wireless communication systems.

# BIBLIOGRAPHY


[1] L. Dussopt, *Transmitarray Antennas*. Cham: Springer International Publishing, 2018. 2, 35

[2] H. Malhat, S. Gaber, and S. Zainud-Deen, *Analysis and Design of Reflectarrays/-Transmitarrays Antennas*. 06 2014. 2, 35

[3] A. H. Abdelrahman, F. Yang, A. Z. Elsherbeni, P. Nayeri, and C. A. Balanis, *Analysis and Design of Transmitarray Antennas*. 2017. 2, 35

[4] A. H. Abdelrahman, A. Z. Elsherbeni, and F. Yang, "Transmission phase limit of multilayer frequency-selective surfaces for transmitarray designs," *IEEE Transactions on Antennas and Propagation*, vol. 62, no. 2, pp. 690–697, 2014. 3

[5] R. Milne, "Dipole array lens antenna," *IEEE Transactions on Antennas and Propagation*, vol. 30, no. 4, pp. 704–712, 1982. 3

[6] C. G. M. Ryan, M. R. Chaharmir, J. Shaker, J. R. Bray, Y. M. M. Antar, and A. Ittipiboon, "A wideband transmitarray using dual-resonant double square rings," *IEEE Transactions on Antennas and Propagation*, vol. 58, no. 5, pp. 1486–1493, 2010. 3

[7] M. A. Al-Joumayly and N. Behdad, "Wideband planar microwave lenses using sub-wavelength spatial phase shifters," *IEEE Transactions on Antennas and Propagation*, vol. 59, no. 12, pp. 4542–4552, 2011. 3

[8] M. Li, M. A. Al-Joumayly, and N. Behdad, "Broadband true-time-delay microwave lenses based on miniaturized element frequency selective surfaces," *IEEE Transactions on Antennas and Propagation*, vol. 61, no. 3, pp. 1166–1179, 2013. 3

[9] H. Song and M. Bialkowski, "Transmit array of transistor amplifiers illuminated by a patch array in the reactive near-field region," *IEEE Transactions on Microwave Theory and Techniques*, vol. 49, no. 3, pp. 470–475, 2001. 4

[10] C.-C. Cheng, B. Lakshminarayanan, and A. Abbaspour-Tamijani, "A programmable lens-array antenna with monolithically integrated mems switches," *IEEE Transactions on Microwave Theory and Techniques*, vol. 57, no. 8, pp. 1874–1884, 2009. 4, 29

[11] P. Padilla, A. Muoz-Acevedo, M. Sierra-Castaer, and M. Sierra-Prez, "Electronically reconfigurable transmitarray at ku band for microwave applications," *IEEE Transactions on Antennas and Propagation*, vol. 58, no. 8, pp. 2571–2579, 2010. 4

[12] H. Kaouach, L. Dussopt, J. Lanteri, T. Koleck, and R. Sauleau, "Wideband low-loss linear and circular polarization transmit-arrays in v-band," *IEEE Transactions on Antennas and Propagation*, vol. 59, no. 7, pp. 2513–2523, 2011. 4

[13] J. Y. Lau and S. V. Hum, "A wideband reconfigurable transmitarray element," *IEEE Transactions on Antennas and Propagation*, vol. 60, no. 3, pp. 1303–1311, 2012. 17, 4, 29, 31

[14] A. Clemente, L. Dussopt, R. Sauleau, P. Potier, and P. Pouliguen, "Wideband 400-element electronically reconfigurable transmitarray in x band," *IEEE Transactions on Antennas and Propagation*, vol. 61, no. 10, pp. 5017–5027, 2013. 16, 4, 29, 30

[15] Q. Cheng, H. F. Ma, and T. J. Cui, "Broadband planar luneburg lens based on complementary metamaterials," *Applied Physics Letters*, vol. 95, no. 18, p. 181901, 2009. 4

[16] Y. Zhang, R. Mittra, and W. Hong, "On the synthesis of a flat lens using a wideband low-reflection gradient-index metamaterial," *Journal of Electromagnetic Waves and Applications*, vol. 25, no. 16, pp. 2178–2187, 2011. 4

[17] L. John Wiley, Sons, *Antenna Analysis Techniques*, ch. 3, pp. 27–78. 2007. 7

[18] P. Nayeri, *Advanced design methodologies and novel applications of reflectarray antennas*. PhD thesis, 2012. Copyright - Database copyright ProQuest LLC; ProQuest does not claim copyright in the individual underlying works; Last updated - 2021-05-13. 7

[19] P. Rost, A. Banchs, I. Berberana, M. Breitbach, M. Doll, H. Droste, C. Mannweiler, M. A. Puente, K. Samdanis, and B. Sayadi, "Mobile network architecture evolution toward 5g," *IEEE Communications Magazine*, vol. 54, no. 5, pp. 84–91, 2016. 8, 55

[20] Y. Liu, N. Li, Y. Jia, W. Zhang, and Z. Zhou, "Low RCS and high-gain patch antenna based on a holographic metasurface," *IEEE Antennas Wireless Propag. Lett.*, vol. 18, pp. 492–496, March 2019. 15, 16, 53

[21] W. Zhang, Y. Liu, S. Gong, J. Wang, and Y. Jiang, "Wideband RCS reduction of a slot array antenna using phase gradient metasurface," *IEEE Antennas Wireless Propag. Lett.*, vol. 17, pp. 2193–2197, Dec 2018. 15

[22] S. Genovesi, F. Costa, and A. Monorchio, "Wideband radar cross section reduction of slot antennas arrays," *IEEE Trans. Antennas Propag.*, vol. 62, pp. 163–173, Jan 2014. 15, 16, 17

[23] J. Su, Y. Lu, J. Liu, Y. Yang, Z. Li, and J. Song, "A novel checkerboard metasurface based on optimized multielement phase cancellation for superwideband RCS reduction," *IEEE Trans. Antennas Propag.*, vol. 66, pp. 7091–7099, Dec 2018. 15

[24] C. Huang, W. Pan, X. Ma, and X. Luo, "A frequency reconfigurable directive antenna with wideband low-RCS property," *IEEE Trans. Antennas Propag.*, vol. 64, pp. 1173–1178, March 2016. 15

[25] D. Sang, Q. Chen, L. Ding, M. Guo, and Y. Fu, "Design of checkerboard amc structure for wideband RCS reduction," *IEEE Trans. Antennas Propag.*, vol. 67, pp. 2604–2612, April 2019. 15, 17, 18

[26] Y. Zheng, J. Gao, X. Cao, Z. Yuan, and H. Yang, "Wideband RCS reduction of a microstrip antenna using artificial magnetic conductor structures," *IEEE Antennas Wireless Propag. Lett.*, vol. 14, pp. 1582–1585, 2015. 15

[27] N. Misran, R. Cahill, and V. F. Fusco, "RCS reduction technique for reflectarray antennas," *Electron. Lett.*, vol. 39, p. 1630, Nov 2003. 15, 18, 19

[28] E. Genender, H. Garbe, and F. Sabath, "Probabilistic risk analysis technique of intentional electromagnetic interference at system level," *IEEE Transactions on Electromagnetic Compatibility*, vol. 56, pp. 200–207, 02 2014. 19

[29] H. Huang and Z. Shen, "Low-RCS reflectarray with phase controllable absorptive frequency-selective reflector," *IEEE Trans. Antennas Propag.*, vol. 67, pp. 190–198, Jan 2019. 16, 19, 20, 53

[30] P. Mei, S. Zhang, Y. Cai, X. Q. Lin, and G. F. Pedersen, "A reflectarray antenna designed with gain filtering and low-RCS properties," *IEEE Trans. Antennas Propag.*, vol. 67, pp. 5362–5371, Aug 2019. 16, 20, 21, 46, 53

[31] Z. Sun, Q. Chen, M. Guo, and Y. Fu, "Low rcs reflectarray antenna based on frequency selective rasorber," *IEEE Antennas and Wireless Propagation Letters*, vol. PP, pp. 1–1, 02 2019. 20, 37

[32] Y. Shang, Z. Shen, and S. Xiao, "Frequency-selective rasorber based on square-loop and cross-dipole arrays," *IEEE Transactions on Antennas and Propagation*, vol. 62, pp. 5581–5589, 11 2014. 21, 36

[33] H. Huang and Z. Shen, "Absorptive frequency-selective transmission structure with square-loop hybrid resonator," *IEEE Antennas and Wireless Propagation Letters*, vol. PP, pp. 1–1, 11 2017. 21

[34] M. Qu, S. Sun, l. Deng, and S. Li, "Design of a frequency-selective rasorber based on notch structure," *IEEE Access*, vol. PP, pp. 1–1, 12 2018. 21

[35] S. Zainud-Deen, S. Gaber, H. Malhet, and K. Awadalla, "Cylindrical perforated transmitarrays," in *The 2nd Middle East Conference on Antennas and Propagation*, pp. 1–7, 2012. 16, 22, 23, 56

[36] T. A. Hill, J. R. Kelly, M. Khalily, and T. W. C. Brown, "Conformal transmitarray for scan loss mitigation with thinned reconfiguration," in *2019 13th European Conference on Antennas and Propagation (EuCAP)*, pp. 1–5, 2019. 16, 22, 23, 56

[37] P.-Y. Qin, L.-z. Song, and Y. J. Guo, "Beam steering conformal transmitarray employing ultra-thin triple-layer slot elements," *IEEE Transactions on Antennas and Propagation*, vol. 67, no. 8, pp. 5390–5398, 2019. 16, 23, 24, 56, 57, 77

[38] L.-Z. Song, P.-Y. Qin, S. Maci, and Y. J. Guo, "Ultrawideband conformal transmitarray employing connected slot-bowtie elements," *IEEE Transactions on Antennas and Propagation*, vol. 69, no. 6, pp. 3273–3283, 2021. 16, 23, 25, 26, 56, 57

[39] L.-Z. Song, P.-Y. Qin, and Y. J. Guo, "A high-efficiency conformal transmitarray antenna employing dual-layer ultrathin huygens element," *IEEE Transactions on Antennas and Propagation*, vol. 69, no. 2, pp. 848–858, 2021. 16, 23, 24, 25, 56, 57, 77, 82

[40] M. Beccaria, P. Pirinoli, and F. Yang, "Preliminary results on conformal transmitarray antennas," in *2018 IEEE International Symposium on Antennas and Propagation USNC/URSI National Radio Science Meeting*, pp. 265–266, 2018. 16, 23, 56

[41] W. An, S. Xu, and M. Li, "A double-layer transmitarray antenna using malta crosses with vias," *IEEE Transactions on Antennas and Propagation*, vol. 64, pp. 1–1, 01 2015. 16, 25, 26, 82

[42] S. Yang, Z. Yan, M. Cai, F. Fan, and T. Zhang, "A high-efficiency double-layer transmitarray antenna using low-loss dual-linearly polarized elements," *IEEE Antennas and Wireless Propagation Letters*, vol. PP, pp. 1–1, 10 2020. 25, 82

[43] X. Zhang, F. Yang, S. Xu, A. Aziz, and M. Li, "Dual-layer transmitarray antenna with high transmission efficiency," *IEEE Transactions on Antennas and Propagation*, vol. 68, no. 8, pp. 6003–6012, 2020. 16, 26, 27, 82

[44] L. Wu, H. F. Ma, Y. Gou, R. Wu, Z. X. Wang, M. Wang, X. Gao, and T. Cui, "High-transmission ultrathin huygens metasurface with 360 phase control by using double-layer transmitarray elements," *Physical Review Applied*, vol. 12, 08 2019. 16, 27, 82

[45] C. Xue, J. Sun, L. Niu, and Q. Lou, "Ultrathin dual-polarized huygens metasurface: Design and application," *Annalen der Physik*, vol. 532, p. 2000151, 06 2020. 27, 82

[46] M. R. Akram, C. He, and W. Zhu, "Ultra-thin bi-layer metasurface based on huygens' principle for high gain antenna applications," *Optics Express*, vol. 28, 05 2020. 27, 77, 82

[47] C. Xue, Q. Lou, and Z. N. Chen, "Broadband double-layered huygens metasurface lens antenna for 5g millimeter-wave systems," *IEEE Transactions on Antennas and Propagation*, vol. PP, pp. 1–1, 09 2019. 27, 77, 82

[48] C. Tian, Y.-C. Jiao, G. Zhao, and H. Wang, "A wideband transmitarray using triple-layer elements combined with cross slots and double square rings," *IEEE Antennas and Wireless Propagation Letters*, vol. PP, pp. 1–1, 01 2017. 16, 27, 28

[49] Q. Luo, S. Gao, M. Sohby, and X.-X. Yang, "Wideband transmitarray with reduced profile," *IEEE Antennas and Wireless Propagation Letters*, vol. PP, pp. 1–1, 01 2018. 16, 27, 28, 36

[50] A. Clemente, L. Dussopt, R. Sauleau, P. Potier, and P. Pouliguen, "Wideband 400-element electronically reconfigurable transmitarray in x band," *IEEE Transactions on Antennas and Propagation*, vol. 61, no. 10, pp. 5017–5027, 2013. 29, 36, 104

[51] C. Huang, W. Pan, X. Ma, and X. Luo, "1 bit reconfigurable circularly polarized transmit-array in x band," *IEEE Antennas and Wireless Propagation Letters*, vol. 15, pp. 1–1, 01 2015. 29

[52] Y. Wang, S. Xu, and M. Li, "A novel 1 bit wide-angle beam scanning reconfigurable transmitarray antenna using an equivalent magnetic dipole element," *IEEE Transactions on Antennas and Propagation*, vol. PP, pp. 1–1, 01 2020. 29, 30, 104

[53] M. Wang, S. Xu, and M. Li, "Design and measurement of a 1-bit reconfigurable transmitarray with subwavelength h-shaped coupling slot elements," *IEEE Transactions on Antennas and Propagation*, vol. PP, pp. 1–1, 03 2019. 29, 104

[54] Y. Xiao, S. Xu, M. Li, K. Zhu, and H. Sun, "Design and implementation of a wideband 1-bit transmitarray based on a yagi-vivaldi unit cell," *IEEE Transactions on Antennas and Propagation*, vol. PP, pp. 1–1, 01 2021. 29

[55] F. Diaby, A. Clemente, R. Sauleau, K. Pham, and L. Dussopt, "2-bit reconfigurable unit-cell and electronically steerable transmitarray at ka-band," *IEEE Transactions on Antennas and Propagation*, vol. PP, pp. 1–1, 12 2019. 29, 30, 33, 82, 104

[56] C.-C. Cheng and A. Abbaspour-Tamijani, "Study of 2-bit antennafilterantenna elements for reconfigurable millimeter-wave lens arrays," *IEEE Transactions on Microwave Theory and Techniques*, vol. 54, pp. 4498 – 4506, 01 2007. 29

[57] C. Huang, W. Pan, and X. Luo, "Low-loss circularly polarized transmitarray for beam steering application," *IEEE Transactions on Antennas and Propagation*, vol. 64, no. 10, pp. 4471–4476, 2016. 17, 29, 30, 31

[58] J. Lau and S. Hum, "Analysis and characterization of a multipole reconfigurable transmitarray element," *IEEE Transactions on Antennas and Propagation*, vol. 59, pp. 70 – 79, 02 2011. 29

[59] J. Lau and S. Hum, "Reconfigurable transmitarray design approaches for beamforming applications," *IEEE Transactions on Antennas and Propagation*, vol. 60, pp. 5679–5689, 12 2012. 29

[60] N. Binh Duong and C. Pichot, "Unit-cell loaded with pin diodes for 1-bit linearly polarized reconfigurable transmitarrays," *IEEE Antennas and Wireless Propagation Letters*, vol. PP, pp. 1–1, 11 2018. 17, 29, 31, 32

[61] L. Boccia, I. Russo, G. Amendola, and G. Di Massa, "Multilayer antenna-filter antenna for beam-steering transmit-array applications," *IEEE Transactions on Microwave Theory and Techniques*, vol. 60, pp. 1–14, 07 2012. 17, 29, 31, 32

[62] J. Reis, R. Caldeirinha, A. Hammoudeh, and N. Copner, "Electronically reconfigurable fss-inspired transmitarray for two dimensional beamsteering," *IEEE Trans. on Antennas and Propagation*, vol. 1, pp. 1–1, 07 2017. 17, 29, 31, 32

[63] P.-Y. Feng, S.-W. Qu, and S. Yang, "Octave bandwidth transmitarrays with a flat gain," *IEEE Transactions on Antennas and Propagation*, vol. PP, pp. 1–1, 07 2018. 36

[64] M. Jiang, Z. N. Chen, Y. Zhang, W. Hong, and X. Xuan, "Metamaterial-based thin planar lens antenna for spatial beamforming and multibeam massive mimo," *IEEE Transactions on Antennas and Propagation*, vol. PP, pp. 1–1, 11 2016. 36

[65] J. Nicholls and S. Hum, "Full-space electronic beam-steering transmitarray with integrated leaky-wave feed," *IEEE Transactions on Antennas and Propagation*, vol. 64, pp. 1–1, 08 2016. 36

[66] H. Yang, X. Cao, S. Xu, J. Gao, X. Chen, M. Li, and T. Li, "A 1600-element dual-frequency electronically reconfigurable reflectarray at x/ku-band," *IEEE Transactions on Antennas and Propagation*, vol. PP, pp. 1–1, 04 2017. 36

[67] A. Omar, Z. Shen, and H. Huang, "Absorptive frequency-selective reflection and transmission structures," *IEEE Transactions on Antennas and Propagation*, vol. PP, pp. 1–1, 09 2017. 36

[68] Q. Chen, S. Yang, J. Bai, and Y. Fu, "Design of absorptive/ transmissive frequency-selective surface based on parallel resonance," *IEEE Transactions on Antennas and Propagation*, vol. PP, pp. 1–1, 07 2017. 36

[69] Y. Han, L. Zhu, Y. Chang, and B. Li, "Dual-polarized bandpass and band-notched frequency-selective absorbers under multimode resonance," *IEEE Transactions on Antennas and Propagation*, vol. PP, pp. 1–1, 09 2018. 36

[70] M. Giordani, M. Polese, M. Mezzavilla, S. Rangan, and M. Zorzi, "Toward 6g networks: Use cases and technologies," *IEEE Communications Magazine*, vol. 58, no. 3, pp. 55–61, 2020. 55

[71] X. Yi, T. Su, X. Li, B. Wu, and L. Yang, "A double-layer wideband transmitarray antenna using two degrees of freedom elements around 20 ghz," *IEEE Transactions on Antennas and Propagation*, vol. PP, pp. 1–1, 01 2019. 77

[72] F. Wu, J. Wang, R. Lu, X. Xia, W. Hong, and K. Luk, "Wideband and low cross-polarization transmitarray using 1-bit magneto-electric dipole elements," *IEEE Transactions on Antennas and Propagation*, vol. PP, pp. 1–1, 10 2020. 85

[73] W. Lin, R. Ziolkowski, and J. Huang, "Electrically small, low profile, highly efficient, huygens dipole rectennas for wirelessly powering internet-of-things (iot) devices," *IEEE Transactions on Antennas and Propagation*, vol. PP, pp. 1–1, 03 2019. 85, 86

[74] C. Pfeiffer and A. Grbic, "Metamaterial huygens surfaces: Tailoring wave fronts with reflectionless sheets," *Physical review letters*, vol. 110, p. 197401, 05 2013. 85, 86

[75] R. Marks, "A multi-line method of network analyzer calibration," *IEEE Transactions on Microwave Theory and Techniques*, vol. 39, pp. 1205 – 1215, 08 1991. 90

[76] W. Wang, R. Jin, T. Bird, H. Fan, X.-L. Liang, and J. Geng, "A multifixture full-wave de-embedding method for characterizing one-port devices," *IEEE Transactions on Microwave Theory and Techniques*, vol. PP, 09 2016. 90